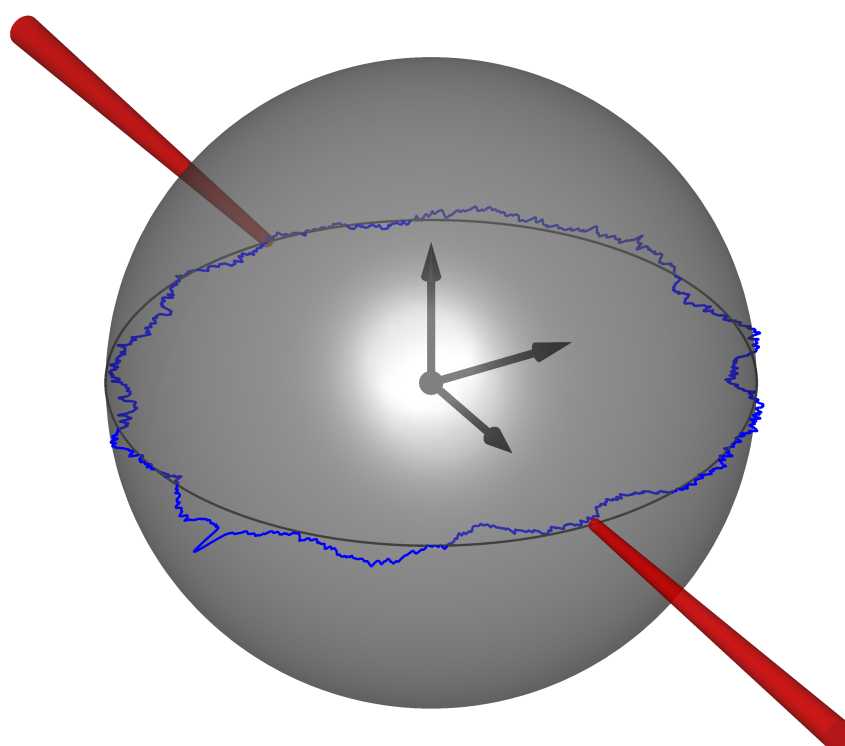


Towards an Advanced LISA Payload Architecture Featuring In-Field Pointing and Spherical Proof Masses



H. Kögel

Towards an Advanced LISA Payload Architecture Featuring In-Field Pointing and Spherical Proof Masses

Vom Fachbereich Produktionstechnik
der
UNIVERSITÄT BREMEN

zur Erlangung des Grades
Doktor-Ingenieur
genehmigte

Dissertation
von
M.Eng. Harald Kögel

Gutachter: Prof. Dr. Claus Braxmaier, Universität Bremen
Prof. Dr. Gerhard Heinzl, Leibniz Universität Hannover

Tag der mündlichen Prüfung: 4. September 2018

Ich habe die vorgelegte Dissertation selbständig und ohne unerlaubte fremde Hilfe verfasst, sowie nur die angegebenen Quellen und Hilfsmittel verwendet. Alle Textstellen, die wörtlich oder inhaltlich aus veröffentlichten oder nicht veröffentlichten Werken entnommen sind, sind als solche kenntlich gemacht.

Bremen, den 22. Oktober 2017

Harald Kögel

Zusammenfassung

Die Vorhersage der Existenz von Gravitationswellen zu Beginn des 20. Jahrhunderts initiierte ein neues Aufgabengebiet innerhalb der beobachtenden Astronomie, da erwartet wurde, dass Gravitationswellen einen tiefen Einblick in unser Universum gewähren würden. Die erste direkte Detektion von Gravitationswellen durch die erdgebundenen LIGO Detektoren im Jahr 2016 – ein bedeutender Erfolg im Bereich der Gravitationswellenbeobachtung – bestätigte die ursprünglichen Vorhersagen und weckte das Interesse zur Entwicklung von verbesserten sowie neuen Gravitationswellendetektoren, die zu neuen Erkenntnissen über unser Universum führen sollen.

Einer dieser neuen Detektoren ist die geplante LISA (Laser Interferometer Space Antenna) Mission, die ein großes Interferometer zur Observation von Gravitationswellen im Weltall aufspannen soll. Hierzu besteht LISA aus drei Satelliten, die in einer Dreiecksformation angeordnet sind und zwischen denen jeweils ein optischer Link gebildet wird. Das Detektionsprinzip von LISA basiert auf der interferometrischen (Laser-) Distanzmessung zwischen frei fliegenden Testmassen, die auf den drei Satelliten angeordnet sind. Diese Testmassen stellen die Endpunkte der Interferometerarme dar und ändern ihre relative Distanz zueinander, sobald eine Gravitationswelle die Satellitenformation durchläuft. Da die Amplituden von Gravitationswellen sehr klein sind (im Bereich von 10^{-21}) und damit auch die relativen Distanzänderungen zwischen den Testmassen (im Bereich einiger weniger zehn pm), stellt deren Detektion eine große Herausforderung dar. Es ist geplant, dass LISA die heute verfügbare Frequenzbandbreite zur Detektion von Gravitationswellen, die durch die erdgebundenen Gravitationswellendetektoren abgedeckt wird, zu tiefen Frequenzen hin (zwischen $3 \cdot 10^{-5}$ Hz – 1 Hz) erweitern wird. Hierdurch verspricht man sich die Beobachtung von neuen Gravitationswellen, die von bisher noch nicht detektierbaren Quellen ausgesendet werden.

Im momentan vorgesehenen Nutzlastkonzept von LISA werden Änderungen im Winkel der Satellitenformation, die durch die individuelle Orbitalmechanik der Satelliten hervorgerufen werden und eine Strahlnachführung erfordern, durch eine aktive Ausrichtung der gesamten Teleskop-Einheiten kompensiert. Dieses Konzept der Strahlnachführung ist unter dem Namen "Telescope Pointing" bekannt. Während der Durchführung der LISA Missionsstudie wurde ein neues, alternatives Nutzlastkonzept entwickelt und theoretisch untersucht, welches das sogenannte "In-Field Pointing" als Schlüsselkonzept einer neuen Methode zur aktiven Strahlnachführung beinhaltet. Die im Zusammenhang mit diesem neuartigen Nutzlastkonzept entwickelte Instrumentenarchitektur bietet potentielle Einsparungen bei Gewicht, Volumen und Leistungsaufnahme, sowie auch eine potentielle Verbesserung der Messgenauigkeit des Messinstruments, im Vergleich zum Nutzlastkonzept mit "Telescope Pointing". Allerdings stellten sich bei der detaillierten Ausarbeitung dieses neuartigen Konzepts, vor allem unter Berücksichtigung der gegebenen Anforderungen an das Messinstrument, einige ungelöste technischen Aufgaben heraus.

Die vorliegende Arbeit befasst sich mit zwei unterschiedlichen und potenziell limitierenden Aspekten bezüglich der Umsetzung dieses neuen LISA Nutzlastkonzepts inklusive "In-Field Pointing". Der erste dargestellte Aspekt ist Teil der detaillierten Untersuchungen zum benötigten Weitwinkelteleskop und behandelt im Speziellen die Änderung der optischen Pfad-

länge im Teleskop, die durch eine integrierte aktive Strahlnachführung und der damit verbundenen Abtastung der Oberfläche der nachfolgenden Teleskopspiegel hervorgerufen wird. Dieser Effekt wurde anhand von experimentellen Messungen, sowie auch einem theoretischen Modell detailliert untersucht und dessen potentielle Auswirkung auf die Messgenauigkeit des LISA Messinstruments bestimmt.

Der zweite Aspekt befasst sich mit einem neuartigen Konzept eines Inertialsensors für LISA, inklusive sphärischer Testmasse und einer vollständig optischen Auslesung. Dieses Konzept stellt eine elegante Lösung für einen hoch-präzisen Inertialsensor dar, der ohne eine elektrostatische Führung der Testmasse fungiert. Ein solcher Inertialsensor hat das Potential für eine weitere Verbesserung der Messgenauigkeit des LISA Messinstruments. Die präsentierten Untersuchungen behandeln im Speziellen die Entwicklung eines optischen Messaufbaus für Oberflächenmessungen an sphärischen Testmassen. Die erzeugten Messdaten dienen der Erstellung einer Oberflächenkarte, die benötigt wird um eine exakte Bestimmung des Schwerpunktes einer frei fliegenden und rotierenden Testmasse zu ermitteln. In diesem Teil der Arbeit werden auch die Messergebnisse der ersten, eindimensionalen Oberflächenmessungen entlang eines Großkreises einer Dummy-Testmasse gezeigt, die einen entscheidenden Schritt in Richtung einer vollständigen (zweidimensionalen) Vermessung der Testmassenoberfläche darstellen.

Beide Themen wurden auf der Grundlage von experimentellen Oberflächenmessungen erarbeitet, die auf der Verwendung von hoch sensitiven, heterodynem Interferometern beruhen. Ein entscheidender Vorteil dieser Messmethode ist deren kontaktlose Natur, wodurch eine Beschädigung der untersuchten Oberflächen vermieden wird. Zudem besitzt diese Messmethode ein hohes Maß an Messgenauigkeit.

Abstract

The prediction of gravitational waves in the early 20th century promised new means for observational astronomy, since they were expected to allow deeper insight into our universe. Recently, the first direct detection of gravitational waves by the earth based LIGO detectors - a major achievement along gravitational wave observation - confirmed the original prediction. This milestone elevated the interest in the development of enhanced as well as new detectors, which hopefully enable the discovery of new aspects of our universe.

One of these new detectors is the planned Laser Interferometer Space Antenna (LISA) space mission, which will represent a giant interferometer for the observation of gravitational waves in space. LISA consists of three satellites, which are arranged in a triangular formation and form three interferometer arms. The detection will be performed via interferometric, inter-satellite laser distance metrology between free-flying proof masses, which act as the end points of the interferometer arms and will change their relative distances with respect to each other when a gravitational wave is passing. However, the strain amplitudes of gravitational waves are small (in the order of 10^{-21}), and so will be the distance changes between the proof masses (in the order of a few tens of a pm), which makes their detection very challenging. LISA will expand the currently available measurement bandwidth covered by the earth based detectors to lower frequencies between $3 \cdot 10^{-5}$ Hz – 1 Hz, hence enabling the detection of new gravitational wave sources.

In the baseline LISA payload architecture, changes in the angles of the triangular spacecraft formation, caused by the individual orbital mechanics of the spacecraft, are compensated by pointing of the whole telescope assemblies. This concept is called telescope pointing. During the LISA mission formulation study a new, alternative LISA payload architecture was developed and theoretically investigated. This concept features in-field pointing in order to compensate for these changes in spacecraft formation. The in-field pointing architecture offers potential savings in mass, volume and power consumption as well as potential improvements in measurement performance of the metrology instrument, compared to telescope pointing. Nonetheless, the technical realisation of the IFP concept in compliance with the requirements is highly demanding.

This thesis covers two different and potentially limiting aspects concerning the realisation of an advanced LISA payload architecture including in-field pointing. The first one is part of the detailed investigations of the required wide-field telescope, suffering from mirror topography induced (optical) path length changes, so called piston, due to active beam steering and walking of the laser beam over the surfaces of subsequent telescope mirrors. This specific effect and its impact on the LISA measurement performance is investigated in more detail based on experimental measurements as well as a theoretical model.

The second aspect investigated in this thesis is a novel concept for a LISA like inertial sensor, which features a spherical proof mass in combination with an all optical read-out. This concept represents an elegant solution for a low-noise, fully drag-free inertial sensor system, which could further increase the measurement performance of the LISA metrology instrument. In particular, the presented investigations include the development of a measurement setup for generating a detailed surface map of spherical proof masses, in order to calibrate its topography with respect

to the sphere's centre of mass. First results of one-dimensional topography measurements of a SPM dummy are presented, representing a first step towards the generation of a complete two-dimensional surface map.

Both topics are based on picometer-precision interferometric topography measurements, utilising highly sensitive heterodyne techniques. A major advantage of this measurement principle is its non-tactile nature, hence avoiding damage of the examined surfaces, while offering high levels of accuracy and reproducibility.

Contents

1	Introduction	1
1.1	Gravitational Waves & Their Detection	1
1.2	LISA - A Space Based Interferometric Gravitational Wave Observatory	4
1.3	IFP & SPMs - An Alternative LISA Payload Architecture	9
2	Optical Path Length Changes in the LISA IFP Telescope	15
2.1	Mirror Surface Characterisation	15
2.1.1	Measurement Setup	15
2.1.1.1	Heterodyne Interferometer	15
2.1.1.2	Pendulum Mechanism	23
2.1.2	Measurements & Results	28
2.1.2.1	Laser Beam Characterisation	30
2.1.2.2	Surface Topography Characterisation	31
2.2	The LISA IFP Telescope Design	41
2.2.1	Estimation of Piston Generated by Beamwalk	45
2.2.1.1	Piston due to Deterministic Pointing	45
2.2.1.2	Piston due to Pointing-Jitter	46
3	An Inertial Sensor Concept featuring a SPM	53
3.1	Surface Mapping of a Sphere	54
3.1.1	Measurement Setup	54
3.1.1.1	Heterodyne Interferometer & Electronics	54
3.1.1.2	Structure & Optical Setup	62
3.1.2	Measurements & Results	67
3.1.2.1	Laser Beam Characterisation	67
3.1.2.2	Proof Mass Actuation Mode	68
3.1.2.3	Surface Mapping	71
3.2	The Proof Mass Levitation System	83
3.2.1	Levitation Test Setup	83
3.2.1.1	Magnetic SPM Dummy	84
3.2.1.2	Electro-Magnet	84
3.2.1.3	Optical SPM Height Sensor	87
3.2.1.4	Digital Control-Loop	92
3.2.2	Measurements & Results	93
4	Conclusions & Outlook	95
	Appendix	105
A.1	Kinematic Trace of the Pendulum Mechanism	107
A.2	Circuit Diagrams of the Interferometer Electronics	109
A.3	Error Movements of the ALAR 100-LP Rotation Stage	113
	Bibliography	I

1 Introduction

Since the early days of mankind, people were keen to understand the luminaries and their motion in the sky. The invention of the telescope in the 17th century finally enabled detailed observations of them and motivated modern astronomy. Over time, the telescope design was constantly improved, which led to a steady increase in resolution, permitting a deeper understanding of the celestial bodies and the universe. After the discovery of infrared radiation in the 19th century, it became clear that there is a much broader spectrum of electromagnetic radiation besides the known, visible range. Over the years, new telescopes had been developed, equipped with specialised detectors in order to explore new regions of the electromagnetic spectrum and with each expansion of the bandwidth, a different aspect of the universe had been discovered. Today, the observable spectral range spans a large part of the electromagnetic spectrum covering ≈ 20 orders of magnitude including radio waves ($\lambda > 1 \text{ m}$), microwaves ($1 \text{ m} \geq \lambda > 1 \text{ mm}$), infrared- ($1 \text{ mm} \geq \lambda > 780 \text{ nm}$), visible- ($780 \text{ nm} \geq \lambda > 380 \text{ nm}$), ultraviolet- ($380 \text{ nm} \geq \lambda > 1 \text{ nm}$), x-ray- ($1 \text{ nm} \geq \lambda > 10 \text{ pm}$) and gamma-radiation ($\lambda < 10 \text{ pm}$).

The prediction of gravitational waves in the early 20th century by A. Einstein promised new means for observational astronomy. In contrast to electromagnetic waves, which can be easily scattered, absorbed and dispersed during propagation, gravitational waves are not significantly affected by intervening matter. This means they travel nearly unimpeded through space and time, carrying information about astronomical phenomena. Due to these unique properties they are expected to provide novel observational data about unexplored regions as well as the very early universe, hence rouse the interest in the development of gravitational wave detectors. Recently, their development has been subject to an increased focus, due to the availability of new technologies, which lead to the construction of several earth based, interferometric detectors as well as concrete plans for a dedicated space mission.

1.1 Gravitational Waves & Their Detection

In 1915, A. Einstein established the field equations of general relativity, which describe the influence of matter and energy on the geometry of space-time [1]. These equations are the core of the theory of general relativity. One year later, in 1916, A. Einstein predicted the existence of gravitational waves, which are supposed to transport energy in form of gravitational radiation, as a solution of these field equations [2, 3].

The theory of general relativity reveals, that the space-time will curve in the presence of mass. When the mass is moving, the corresponding curvature of space-time is moving along with it, and when the mass is accelerated, the corresponding curvature of space-time changes, hence generating gravitational waves. Therefore, gravitational waves can be described as waveform-like distortions of the space-time, which periodically change the distance between free objects, without imposing a force on them.

Given their nature, gravitational waves can exist at any frequency, propagating at the speed of light from the source outwards on in the form of transverse waves. During propagation their amplitude decreases proportional to the inverse distance to the source, which implies that it

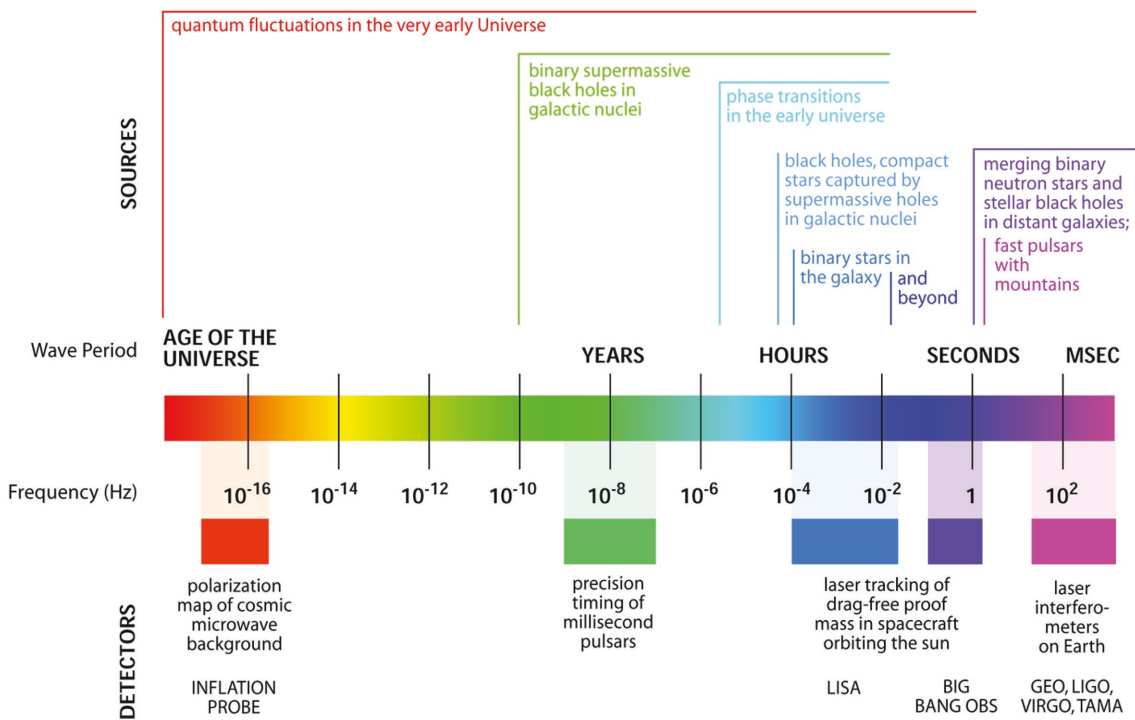


Figure 1.1: Overview of the gravitational wave spectrum. Depicted are potential astrophysical sources as well as proven and promising detection techniques. [Source: NASA Goddard Space Flight Center - Gravitational Astrophysics Laboratory; University of Glasgow - Institute for Gravitational Research]

will be small, when they arrive at earth. This also implies, that only powerful sources and events are expected to be detectable, including black hole inspirals and mergers, neutron star mergers as well as supernovae, to mention just a few of them. However, even those powerful sources are expected to generate only extremely low strain amplitudes in the order of $\approx 10^{-21}$, which makes them very challenging to detect. When only considering such powerful sources, the expected frequency range of detectable gravitational waves is expected to be between $\approx 10^{-16} \text{ Hz} - 10^4 \text{ Hz}$, which represents an indicator for the required measurement bandwidth of gravitational wave detectors [4]. An overview of the gravitational wave spectrum as well as their sources is depicted in Figure 1.1.

First attempts for the direct detection of gravitational waves were performed in the early 1960s by J. Weber and involved resonant bar detectors, so called Weber bars [5]. The original Weber bars featured a cylindrical shape and were made of aluminium with a resonance frequency at $\approx 1660 \text{ Hz}$. J. Weber expected, that a passing gravitational wave near the resonance frequency will excite the resonator and the signal is then amplified to a detectable level for the piezo-electric sensors mounted at the side walls of the detector. In general, Weber bars only provide a narrow bandwidth of $\approx 1 \text{ Hz}$ around their resonance frequency, which limits their application almost exclusively to the detection of burst events like for example supernovae.

Even today there are still Weber bars in operation. One example is the MiniGRAIL detector in the Netherlands [6]. This detector features a spherical shape, in order to detect gravitational waves from different spatial directions and is equipped with highly sensitive superconducting quantum interference devices for detecting vibrations. Combined with a cryogenic environment for reduced thermal noise it shows a considerably improved strain sensitivity in the order of

$\approx 10^{-19}$ compared to the original detectors. However, there has not been a successful detection of gravitational waves involving a Weber bar, yet.

An indirect proof for the existence of gravitational waves was achieved by J. Taylor, L. Fowler and P. McCulloch in the late 1970s, based on the observation of the orbital period of the binary pulsar system PSR B1913 + 16 [7, 8]. This particular pulsar system was discovered in 1974 by R. Hulse and J. Taylor and promised to be a suitable candidate for testing general relativity, due to the expected strong emission of energy. The idea behind this proof was based on the assumption, that a reduction in energy of the pulsar system, due to gravitational radiation, will draw the involved stars closer to each other, hence decreasing their orbital period. This phenomena is called an inspiral, and interestingly, long time observations with the Arecibo radio telescope actually showed a measurable reduction in orbital period of the pulsar system. A comparison of the measurement results with theoretical predictions of the development of the orbital period according to general relativity showed very good agreement, which finally confirmed the original assumption. Up to now, several more binary pulsar systems have been detected, which are regularly used for testing general relativity as well as alternative theories of gravity.

A different approach for the direct detection of gravitational waves was proposed in 1962 by M. Gertsenshtein and V. Pustovoit based on laser interferometry [9]. Later, in the 1970s, concrete plans for the construction of interferometric gravitational wave detectors were developed. However, it was not before the mid 1990s when their construction finally started. The idea behind an interferometric gravitational wave detector is based on the principle of a Michelson interferometer. The main feature in this application is, that the end-mirror in each interferometer arm is suspended in order to decouple it from seismic events, hence acting as a proof mass. A passing gravitational wave will cause a differential change in distance between the end-mirrors, which can be detected in the interference pattern of the interferometer.

Today there are several interferometric gravitational wave detectors operated around the world reaching strain sensitivities in the order of 10^{-21} , namely LIGO (4 km arm-length), Virgo (3 km arm-length), GEO600 (600 m arm-length), and TAMA 300 (300 m arm-length) [10]. They will be soon joined by the new KARGA Detector (3 km arm-length), which is currently under construction in Japan and is intended to be operational in 2018. In contrast to a Weber bar, these interferometric detectors feature a considerably larger measurement bandwidth ranging from a few hundred Hz to a few kHz, see Figure 1.2, which enables the detection of a broader range of gravitational wave sources including supernovae and the coalescence of neutron stars as well as black holes. The typical measurement bandwidth of these interferometric detectors is between $\approx 10 \text{ Hz} - 10^4 \text{ Hz}$, mainly dependent on their effective arm-length.

In 2016, the LIGO collaboration announced the first direct detection of a gravitational wave, which was observed on the 14th of September 2015 at both operated sites in Hanford and Livingston within a short time shift [12]. The event was identified as a merger of two black holes at a distance of ≈ 1.3 billion light years. A second detection was announced shortly after, which was observed on the 26th of December 2015. Also this event was identified as a merger of black holes, however this time at a distance of ≈ 1.4 billion light years.

In the near future some of the existing interferometric gravitational wave detectors will be enhanced, in order to further increase sensitivity and to expand their measurement bandwidth. This will enable the detection of even more distant gravitational wave sources as well as the rate of detected events. However, the typical limitation of earth-based gravitational wave detectors will still remain, which is the strongly reduced sensitivity at low frequencies, due to gravity gradient noise on earth and the principal limitation in arm length. This noise is

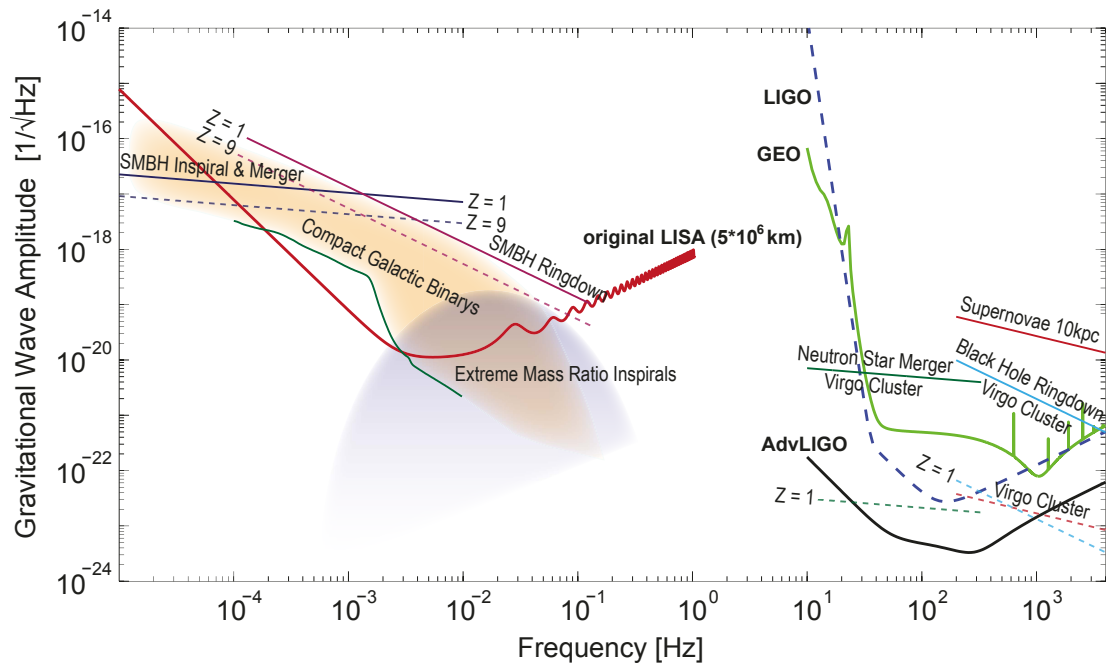


Figure 1.2: Sensitivities of the ground based (LIGO and GEO) as well as space based (original LISA) detectors, along with potential sources of gravitational waves. The solid source curves represent upper limits, and the dashed curves (of the same colour) represent equivalent sources at greater distances [11].

mainly caused by seismic vibrations and prevents the detection of low-frequency gravitational waves below 10 Hz. As a solution for this specific problem, the concept of a space-based, interferometric gravitational wave detector had been investigated in the 1980s, which should be able to detect gravitational waves at frequencies below 1 Hz, hence expanding the currently available detection bandwidth of earth-based detectors to lower frequencies. Over the next decade, the concept has been refined and was proposed to the European Space Agency (ESA) in 1993 under the new mission name Laser Interferometer Space Antenna (LISA)[13].

1.2 LISA - A Space Based Interferometric Gravitational Wave Observatory

The development of the LISA space mission has not always been straight forward. In 1997, a few years after its first proposal to ESA, it was decided that LISA should be developed in collaboration with the National Aeronautic and Space Administration (NASA), due to the expected high costs. Over the next decade, the development led to a detailed mission concept, which consists of 3 spacecraft, arranged in a triangular formation, representing a giant Michelson-like interferometer with 3 arms of a length of $\approx 5 \cdot 10^6$ km. In order to detect gravitational waves the distance between proof masses on the distant spacecraft is measured with high accuracy.

In early 2011, NASA announced their decision to pull out of the mission, due to budget cuts, and withdrew all planned contributions. ESA decided still to push on and initiated a redesign of the mission with the focus on cost-reduction, in order for it to become a possible candidate for an upcoming mission selection in 2012. A revised mission concept was developed and proposed under the name New Gravitational Wave Observatory (NGO). Similar to LISA this new concept

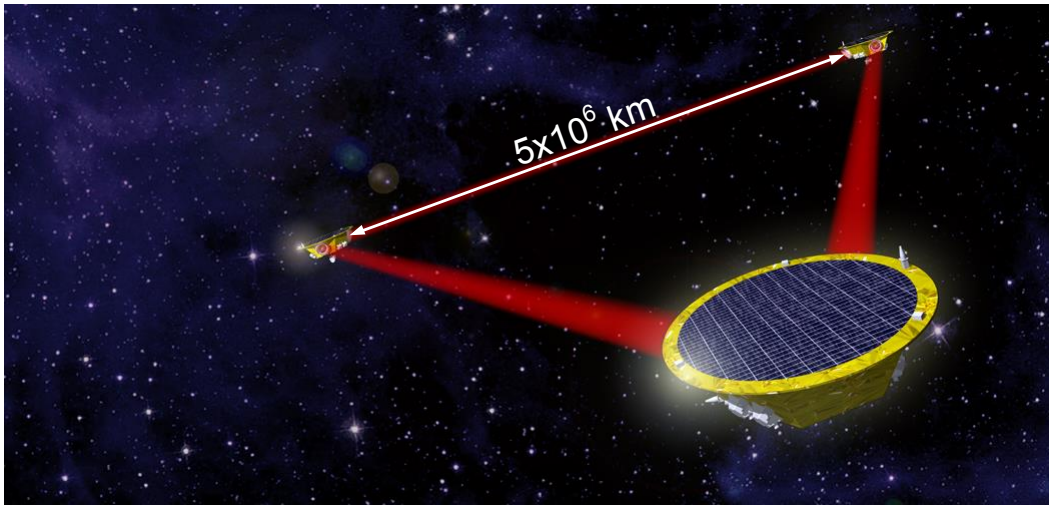


Figure 1.3: Artist's view of the original LISA spacecraft formation, representing a 3 arm (Michelson-like) interferometer with an arm-length of $\approx 5 \cdot 10^6$ km.

featured 3 spacecraft, arranged in a triangular formation. However, the spacecraft work in a mother-daughter configuration with just 2 interferometer arms of a length of $\approx 1 \cdot 10^6$ km [14]. Despite the redesign, NGO was not selected on the grounds of an uncertain readiness-level of its technology at launch date. Then, in late 2013, ESA selected the theme for the upcoming L3 mission to be "The Gravitational Universe", to that, in late 2016, the call for proposals was announced. In response to the call, a new LISA mission was proposed, with a concept similar to the original one, including 3 spacecraft and 3 interferometer arms, but with a reduced arm-length of $\approx 2.5 \cdot 10^6$ km. A few months later, in mid 2017, the new LISA mission was finally confirmed by ESA as the L3 candidate, which is now planned to be launched in 2034.

Since the investigations in this thesis are initiated by original LISA ($5 \cdot 10^6$ km arm-length), the following mission description refers to this specific configuration. Nonetheless, the presented models and results are transferable to different LISA configurations as well as other space missions, which involve optical links between spacecraft and formation flying. As mentioned earlier, LISA consists of 3 spacecraft, which are arranged in an equilateral triangle with $\approx 5 \cdot 10^6$ km in side-length, see Figure 1.3. The formation will fly on a heliocentric orbit, trailing the earth at 20° , and the plane spanned by the 3 spacecraft is inclined by 60° with respect to the ecliptic. The individual orbital mechanics of the spacecraft causes the LISA formation to rotate around its centre once every year and also to slightly change its triangular shape. The latter is called breathing and includes changes in distance as well as inter-arm angle between the spacecraft, which can not completely be removed by orbit optimisation.

Together, the LISA formation represents a set of giant Michelson-like interferometers with 3 arms, and highly sensitive distance metrology between the proof masses on the spacecraft. In order to enable interferometry over these large distances, the spacecraft are mutually linked in an active transponder scheme. Two (nearly) free-flying proof masses located on each spacecraft represent the end-points, more specifically the reference-points of each interferometer arm and define its length. These proof masses are shielded from external disturbances and follow in a nearly perfect geodesic motion. A passing gravitational wave is expected to change the distance between the proof masses in the order of a few tens of a μm , which can be detected in the interferometer signals. Thereby the use of 3 interferometer arms facilitates

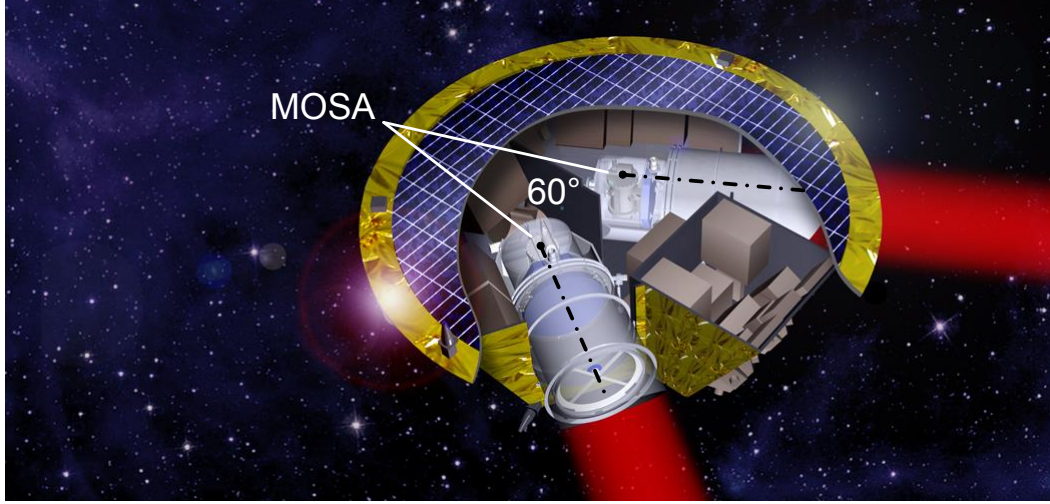


Figure 1.4: Section view of a LISA spacecraft including its two articulated MOSA for telescope pointing, arranged in a $\approx 60^\circ$ angle in order to match the LISA spacecraft formation.

the determination of the propagation direction of the gravitational wave. The expected LISA sensitivity curve is depicted in Figure 1.2, which also shows its wide detection bandwidth for gravitational waves between $3 \cdot 10^{-5} \text{ Hz} - 1 \text{ Hz}$. In order to reach this sensitivity, several demanding requirements for the LISA metrology instrument were derived in a breakdown of the required strain sensitivity, including the requirement for displacement noise \tilde{q}_l (single link) and the requirement for proof mass acceleration noise \tilde{q}_a (single proof mass) [15], given at:

$$\tilde{q}_l(f) = 12 \cdot 10^{-12} \frac{\text{m}}{\sqrt{\text{Hz}}} \cdot \sqrt{1 + \left(\frac{2.8 \text{ mHz}}{f}\right)^4} \quad (1.1)$$

$$\tilde{q}_a(f) = 3 \cdot 10^{-15} \frac{\text{m}}{\text{s}^2 \sqrt{\text{Hz}}} \cdot \sqrt{1 + \left(\frac{f}{8 \text{ mHz}}\right)^4} \quad (1.2)$$

In order to perform the interferometric distance measurements, each LISA spacecraft is equipped with two moveable optical sub-assemblies (MOSA), which are arranged at 60° with respect to each other in order to match the triangular spacecraft formation, see Figure 1.4. The entire MOSA is articulated, in order to track the laser beam with respect to the remote spacecraft, hence enabling compensation for changes in inter-arm angle of the formation in the order of $\approx \pm 0.8^\circ$, caused by the breathing. This concept for changing the line of sight of the telescopes is known as telescope pointing. Thereby, each MOSA consists of three main components, namely:

- The Cassegrain telescope ($\varnothing 400 \text{ mm}$) for sending and receiving laser light to and from the remote spacecraft.
- The optical bench, which holds the optics, detectors and mechanism required for the heterodyne interferometry.
- The gravitational reference sensor (GRS), which holds a free-flying cubical proof mass, enclosed by the electrode housing as well as the caging mechanism for catching / releasing of the proof mass in orbit.

Together, these components represent the core-system of the LISA metrology instrument. Figure 1.5 shows a rendering of the MOSA architecture including these three main sub-assemblies. The whole GRS is enclosed by a vacuum housing, which shields the proof mass from external disturbances, hence ensuring an unperturbed environment for the detection of gravitational waves. As mentioned above, the GRS includes besides the proof mass also the electrode housing, which enables electrostatic sensing and actuation of the proof mass position, as well as the caging mechanism for releasing and catching of the proof mass in orbit. The proof mass itself acts as one end-mirror of an interferometer arm and, at the same time, as the inertial reference for the spacecraft's drag-free attitude control system.

In addition, each spacecraft carries two laser systems, one for each optical bench, resulting in a total of six laser systems for the constellation. However, there will be only one frequency stabilised (master) laser system at the time, whereas the other five (slave) laser systems are phase locked to this master.

The distance measurement within LISA utilises a so called strap-down architecture, which implements a break-down of the overall length of each interferometer arm into three technically and functionally decoupled distance measurements. These are:

- The intra-spacecraft distance measurement between the proof mass and the optical bench of the local spacecraft.
- The inter-spacecraft distance measurement between the optical benches of the local and the remote spacecraft.
- The intra-spacecraft distance measurement between the proof mass and the optical bench of the remote spacecraft.

The principle behind the strap-down architecture is also displayed in Figure 1.6. Adding these three individual measurements together allows to measure the overall distance variation between the free-flying proof masses within one interferometer arm. A unique property of the (long) inter-satellite distance metrology is the transponder scheme applied. The laser light emitted from the local spacecraft at $\approx 1\text{ W}$ is received by the remote spacecraft at a considerable reduced power ($\approx 150\text{ pW}$), due to beam expansion and the limited telescope diameter. Since this power is too low to be directly reflected back to the local spacecraft, the onboard laser on the remote spacecraft is phase locked to the incoming laser light and is used to send back laser light at $\approx 1\text{ W}$ of identical phase with respect to the incoming light.

In 2015, the LISA Pathfinder (LPF) mission was launched in order to test and validate key technologies of LISA. LPF consists of a single spacecraft and carries two different drag-free control systems (one developed by ESA and the other one developed by NASA) as well as the LISA Technology Package (LTP) [16, 17]. The latter comprises two LISA like inertial sensors with free-flying cubical proof masses as well as an optical bench including a highly sensitive heterodyne interferometer and the corresponding instrumentation [18]. The read-out of the proof mass position is realised via a combination of optical and capacitive sensing. Technically, LTP represents one interferometer arm of LISA, reduced to an arm-length of $< 0.5\text{ m}$ [19]. The main objectives of the mission are:

- Test of highly-precise laser interferometry between (cubical) proof masses.
- Test of an ultra-low disturbance environment of the proof mass in the GRSs.
- Test of the drag-free attitude control of the spacecraft including the μN thrusters.

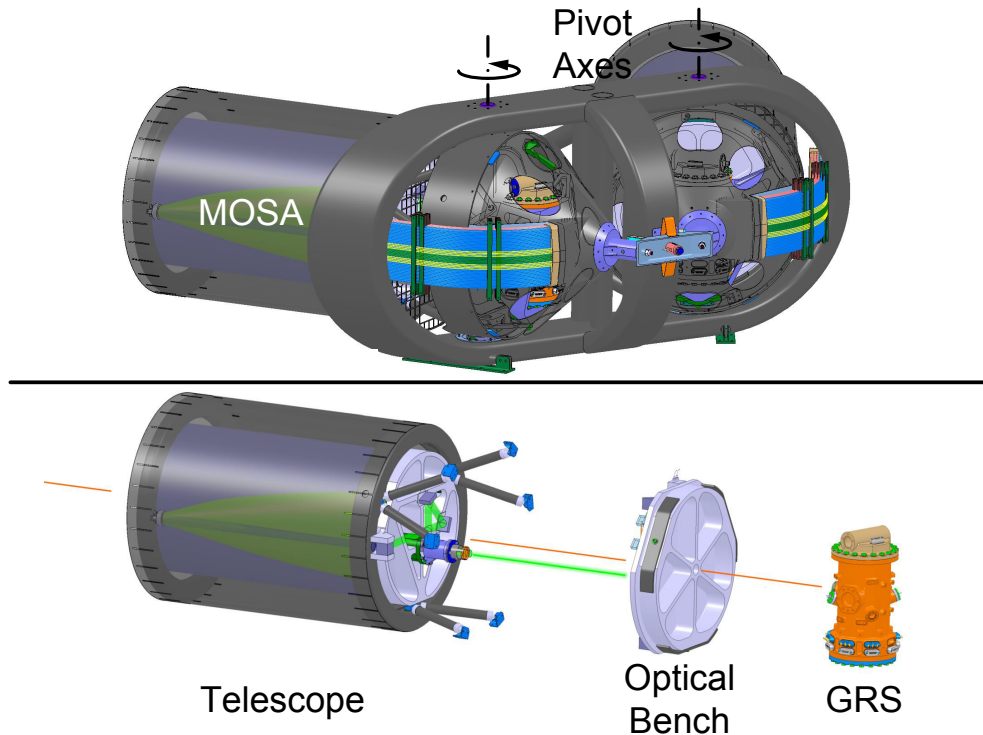


Figure 1.5: Rendering of the opto-mechanical system of the LISA metrology instrument, including the two MOSA for telescope pointing as utilised in the baseline concept (top). The architecture of each MOSA comprises three main sub-assemblies, the telescope, the optical bench and the GRS (bottom).

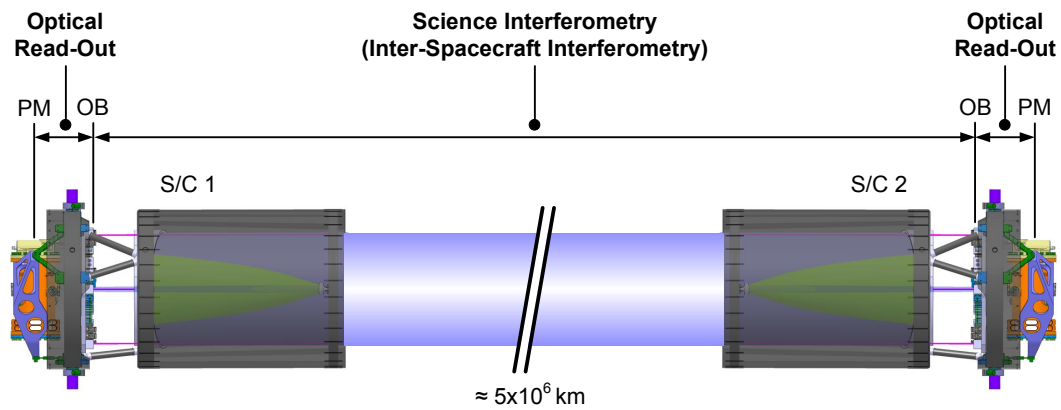


Figure 1.6: Principle of the strap-down architecture utilised (for a single link), which implements a break-down of the overall length of each LISA interferometer arm into three technically and functionally decoupled distance measurements. These include two intra-spacecraft distance measurements between the proof mass (PM) and the optical bench (OB) of each spacecraft (S/C), as well as the inter-spacecraft distance measurement between the two optical benches of the local and remote spacecraft.

The targeted differential acceleration noise of the inertial sensor is $3 \cdot 10^{-14} \text{ m s}^{-2} \text{ Hz}^{-0.5}$, a factor of 10 above the level required for LISA. In 2016 the first measurement results were published, which overfulfilled the high-level requirement and confirmed the feasibility of several key aspects of the proposed LISA metrology concept [20].

1.3 IFP & SPMs - An Alternative LISA Payload Architecture

The in-field pointing (IFP) concept was developed as part of the LISA Mission Formulation study under ESA contract and represents a conceptual design of an alternative opto-mechanical architecture for the LISA metrology instrument [21, 22]. Compared to telescope pointing, which moves the whole MOSA, including the telescope, optical bench and GRS, IFP only utilises a small actuated mirror within the telescope in order to change its line of sight for compensating the breathing of the LISA spacecraft formation. Therefore the instrument is equipped with a wide-field telescope, which offers the required field of view of $\pm 0.5^\circ$. The actuated mirror for beam steering is positioned in an intermediate pupil plane of the telescope and is represented by the in-field pointing mechanism (IFPM), see Figure 1.7. The implementation of the IFP concept allows for a redesign of the opto-mechanical architecture of LISA with respect to the baseline concept:

- The omission of the MOSAs, including their articulation mechanism and launch locks enables the realisation of a fixed opto-mechanical design for the instrument with only small moved masses, hence minimised self-gravity effects. Therein the telescopes, the optical bench and the GRSs are rigidly attached to the structure of the instrument, since an articulation is not required. The fixed telescopes allow for the use of a single common optical bench per spacecraft, which is attached to both telescopes. This solution avoids the use of articulated backlink fibres, that establish an optical phase reference between the two separate optical benches in the baseline concept.
- The IFP architecture with the fixed opto-mechanical instrument design integrates more coherently with the application of a single active GRS configuration. In this configuration, each spacecraft actively operates only a single GRS system, with one proof mass, that acts as the reference point of both adjacent interferometer arms. A second GRS system can be implemented optionally in order to establish a redundancy. However, the performance of the LISA metrology instrument will decrease, when this second GRS is used.

Figure 1.8 shows a rendering of the proposed opto-mechanical IFP architecture. In general, the IFP concept offers high flexibility in the choice of the layout of the instrument as well as potential savings in mass, volume and power consumption, compared to the baseline concept. It could also improve mission robustness, when implementing a single active GRS configuration including a second GRS system for redundancy on each spacecraft.

The application of the single active GRS concept within the IFP architecture in particular is interesting, since it is expected to reduce the acceleration noise of the proof masses, thus improving the measurement performance of the metrology instrument. In an instrument configuration that features two active GRS systems onboard each spacecraft, as proposed in the baseline concept, the satellite's drag-free attitude control system is only able to keep the proof masses in a free-flying state along one (translational) degree of freedom (DoF), in case of LISA the measurement line of the interferometer arms. The other five DoFs have to

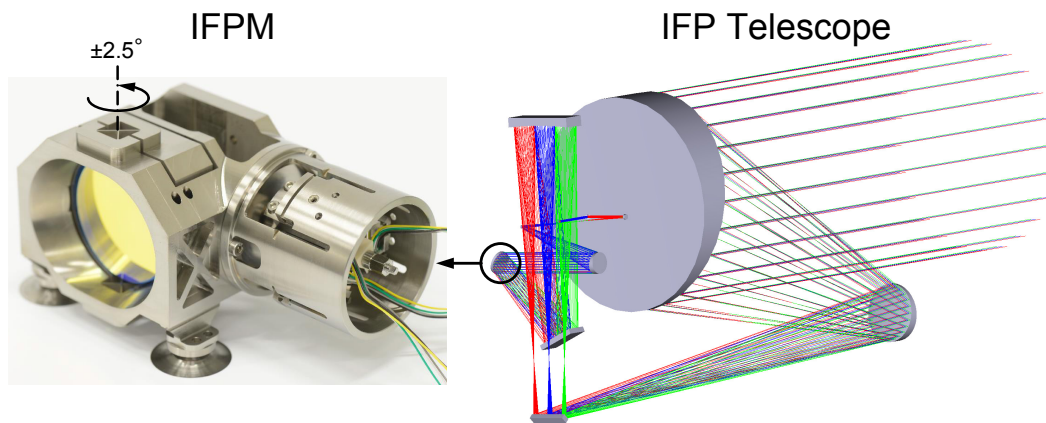


Figure 1.7: Photograph of the IFPM for beam steering, which is positioned in an intermediate pupil plane of the telescope (left) [Courtesy of TNO]. Optical design of the IFP wide-field telescope (right). Three different orientations of the IFPM are indicated by different colours of the optical paths, blue for 0° , red for $+2.5^\circ$ and green for -2.5° , covering the required external field of view of the telescope of $\pm 0.5^\circ$.

be controlled via an electro-static suspension in order to compensate for relative movements between the proof masses themselves as well as to avoid contact of the proof masses with the surrounding electrode housing. However, these suspension forces are expected to introduce additional acceleration noise to the proof mass, also in the non-guided measurement direction due to cross coupling effects, which is expected to limit the measurement performance. In the proposed single active GRS concept, only one free-flying proof mass per spacecraft is operated at a time, which does not require a suspension in its translational DoFs, since the spacecraft can perfectly trace its motion.

Despite offering high flexibility as well as potential advantages in measurement performance, the technical realisation of the IFP concept in compliance with the requirements for the LISA metrology instrument is highly demanding. Especially the optical design of the wide-field telescope including the required IFPM for beam steering is challenging with respect to providing the optical performance over the complete field of view. This refers in particular to the far field quality of the transmitted beam as well as the achievable heterodyne efficiency for reception of a plane wave, which strongly influences the measurement noise.

An additional important aspect is the generation of optical path length variations within the telescope due to geometrical coupling of tilt to optical path length during active beam steering as well as thermo-elastic effects coupling to optical path length. The first effect is almost solely generated by the beam steering implemented, and is dependent on the mechanical design of the IFPM, in particular the kinematics of the hinge. Additional errors are introduced by manufacturing and alignment tolerances (with respect to the intermediate pupil plane) as well as the general optical design of the telescope. The resulting path length variations are expected to be in the order of $1 \mu\text{m}$ for an actuation over the full range / full field of view, with the main contribution expected to be generated by the kinematics of the IFPM hinge. Additional small contributions to the path length variations are expected due to beamwalk across the surfaces of optical components, generated by IFPM beam steering as well as IFPM pointing jitter. This specific effect and its impact in the measurement accuracy of the LISA metrology instrument is investigated in more detail in Chapter 2 of this thesis.

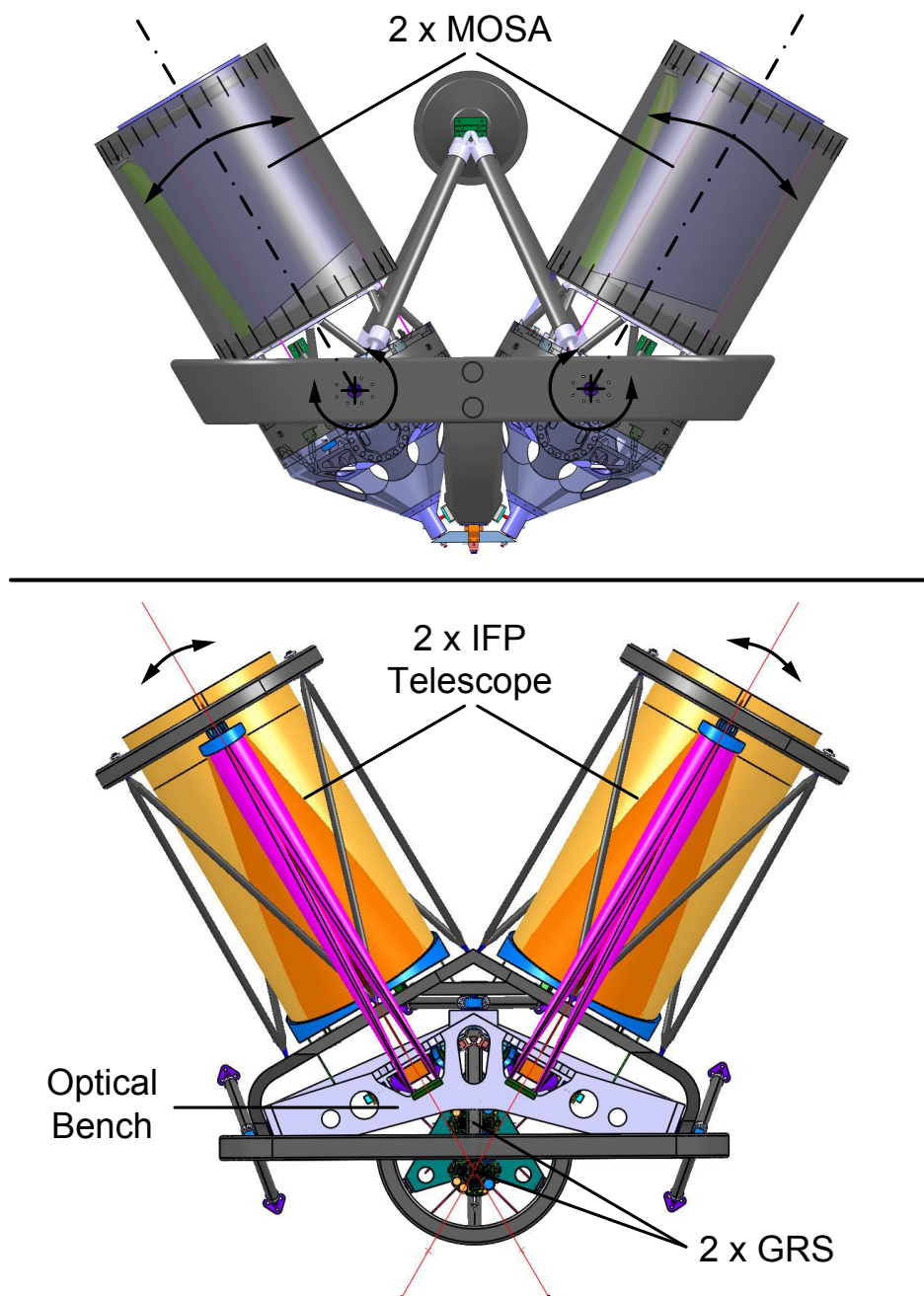


Figure 1.8: Comparison of the different opto-mechanical architectures of the LISA metrology instrument. Telescope pointing (top), which involves the movement of the whole MOSA in order to change the line of sight of the instrument. IFP (bottom), which features a small actuated mirror within the wide-field telescope for changing its line of sight. This concept enables a fixed opto-mechanical design, in which the telescopes as well as the optical bench and the GRSs are rigidly attached to the structure of the instrument.

In a more advanced version of the single active GRS within the IFP concept, the application of a spherical proof mass (SPM) has been considered, since it offers several potential advantages including improvements in measurement performance of the LISA metrology instrument. The concept of a drag-free inertial reference system featuring a SPM and the technology for following a geodesic in space goes back to the TRIAD satellite (1972), and its novel Disturbance Compensation System (DISCOS) [23, 24, 25]. More recently, the Gravity Probe-B (GP-B) satellite (2004), first demonstrated a drag-free control in accelerometer mode, also featuring SPMs [26]. Already in the first LISA industrial study (1998-2000), SPMs had been briefly considered for a possible application within the GRSs, since they represent a more natural / canonical approach for solving the given tasks in LISA compared to the cubic proof masses [27]. However this idea was quickly discarded due to unsolved problems with dealing with non perfect spheres at the scale of the required accuracy for centre of mass (CoM) position determination.

Nonetheless, due to their potential advantages, several investigations were started in order to solve these problems and to examine the application of SPMs in the LISA mission in more detail [28, 29, 30, 31]. The application of SPMs offers a solution for the general problem of cubical proof masses, which is the required suspension in their rotational DoFs in order to enable an optical read-out between proof mass and optical bench. Without a suspension, the proof mass will slowly rotate within the GRS due to residual torques, hence the laser beam of the read-out will reflect off the cubical proof mass surface in a random angle. In contrast, SPMs feature a rotationally symmetric shape, where the laser beam will reflect off the surface in itself independent of their actual orientation, thus enabling a fully drag-free concept of the proof mass without the need for controlling specific DoFs.

An additional advantage, which comes with the omission of the suspension electrodes and the application of an all-optical read-out, is the possibility to use a larger gap between the proof mass and the surrounding housing. During in-orbit operation, the proof mass gets charged due to contact electrification (during proof mass release), charged particles and high-energy plasma in its near environment as well as cosmic ray impacts. These charges will induce forces onto the proof mass, when interacting with the housing, which will result in residual proof mass acceleration noise. Since the force gradient is expected to scale at $\approx l_g^{-3}$ with respect to the gap size, a larger gap will reduce the proof mass acceleration noise. Considering these aspects, the application of SPMs represents an elegant solution for a low-noise, fully drag-free GRS system, which can be applied also in a larger class of drag-free space missions besides LISA.

Further investigations resulted in a conceptual GRS design including SPMs, called the modular gravitational reference sensor (MGRS), which is intended for the application in LISA [32, 33, 34]. Herein, one major limitation identified so far are errors in position determination of the SPM's CoM due to its surface topography and the involved optical path length changes under rotation, which will be misinterpreted as changes in CoM position by the read-out. It is expected, that even with modern technologies the surface of a SPM can only be manufactured to a precision in the order of a few tens of a μm (peak to valley amplitudes of the topography) [35, 36]. Since this value is $\approx 10^3$ times higher than the allocated LISA requirement for displacement noise (see Equation 1.1), the SPM topography will represent a dominant source of error, which has to be considered.

At the moment, two complementary solutions are discussed and investigated to address this issue [37]:

- The application of a defined spin (≥ 10 Hz) to the SPM in order to average its surface, thus (spectrally) shifting topography induced errors as well as mass centre offset errors due to inhomogeneities in density outside the LISA measurement bandwidth between $3 \cdot 10^{-5}$ Hz - 1 Hz.
- The implementation of a correction algorithm, which utilises a detailed SPM surface map, measured on ground prior to launch of the satellites, for a subsequent correction of the topography induced errors in the recorded in-orbit measurement data.

In particular, the second solution, namely the prior calibration of the surface topography and subsequent referencing of the laser metrology to the surface of a slowly tumbling SPM triggered the work described in Chapter 3 of this thesis. It describes in detail the development of an optical measurement setup based on heterodyne interferometry, which enables precise, contact-free surface metrology.

Despite the potential advantages, the application of SPMs within the LISA mission is not likely, since suitable GRSs featuring cubical proof masses are already successfully tested in space in the scope of the LPF mission and thus exhibit a considerable higher level of maturity. Nonetheless, the concept of SPMs promises to be still relevant for an application in future space missions beyond LISA, which require drag-free satellites and even more stringent performance levels. One example is the suggested Big Bang Observer (BBO), which has been proposed as a follow-up mission for gravitational wave detection [38].

2 Optical Path Length Changes in the LISA IFP Telescope

As described in Chapter 1 of this thesis, each IFP wide-field telescope features an IFPM for steering its line of sight. This beam steering generates optical path length variations within the telescope, so called piston, due to several linked effects, including geometrical coupling of tilt to piston and thermo-elastic effects coupling to piston. Especially the first one is almost solely generated by the beam steering implemented and is dependent on the mechanical design of the IFPM, in particular the kinematics of the hinge. Additional errors are introduced by manufacturing and alignment tolerances (with respect to the intermediate pupil plane) as well as by IFPM beam steering / IFPM pointing-jitter and the associated beamwalk across surfaces of subsequent optical components in the telescope [39].

This chapter covers in particular the latter effect. Therefore the surface of a typical laser mirror is experimentally characterised and measured in order to validate a theoretical surface model, which is then applied to predict the level as well as the impact of beamwalk induced piston in the measurement performance of the LISA metrology instrument.

2.1 Mirror Surface Characterisation

Since the information provided about the surface of optical components is not detailed, an off-the-shelf laser mirror (in the further course referred to as test mirror) is experimentally characterised. The measurement results are then used to calculate the surface spectrum of the test mirror, which is expected to be representative for a first estimation of the piston generated by beamwalk in the IFP wide-field telescope. The test mirror employed is made of BK-7 with a diameter of 25 mm. Its base substrate surface flatness (before coating) is claimed to be $\lambda/10$ or $3/0.2$ (referenced to $\lambda = 633\text{ nm}$) and surface defects are defined at $5/3 \times 0.025$, both according to DIN ISO 10110.

2.1.1 Measurement Setup

A schematic of the measurement setup is depicted in Figure 2.1, which is designed to mimic surface topography induced changes in optical path length by scanning a laser beam over the test mirror surface. Therefore it features a piezo driven pendulum mechanism, which moves the test mirror lateral to the output laser beams of a heterodyne laser interferometer. During movement the test mirror's topography will introduce linear wavefront displacements as well as wavefront tilts in the laser beams, which are measured by the interferometer and used to characterise the test mirror surface. Similar approaches for surface characterisations and measurements have already been successfully applied also involving heterodyne interferometry [40, 41].

2.1.1.1 Heterodyne Interferometer

The heterodyne laser interferometer utilised is based on a highly symmetric interferometer design with spatially separated laser beams for the two different laser frequencies [42], which has been adapted for the use as an optical read-out of the LISA proof masses [43, 44].

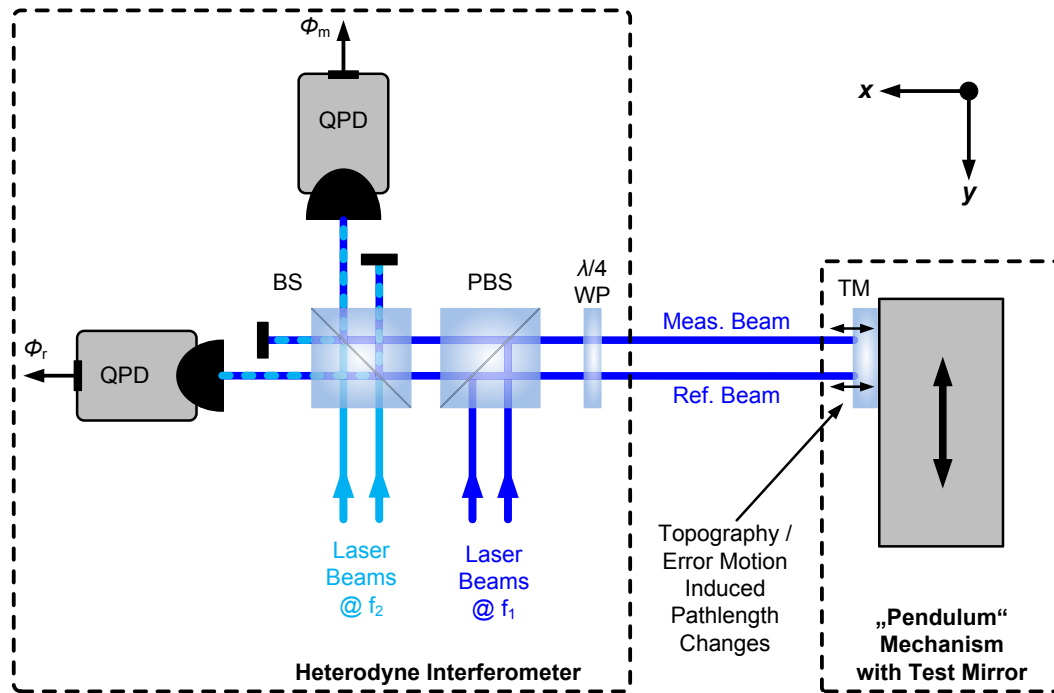


Figure 2.1: Schematic of the measurement principle applied for characterising the surface topography of a test mirror, which is used to estimate the beamwalk induced piston in the IFP wide-field telescope. BS: 50/50 Beam Splitter; PBS: Polarising Beam Splitter; WP: Wave Plate; TM: Test Mirror; QPD: Quadrant Photo Detector;

This interferometer design offers high resolution and sensitivity for measuring linear wavefront displacements and, if equipped with quadrant photo detectors (QPDs), also for wavefront tilts, while being insensitive to DC intensity variations. Seed laser is a Nd:YAG NPRO Laser at a wavelength of $\lambda_0 = 1064 \text{ nm}$.

A schematic of the interferometer's heterodyne frequency generation setup is depicted in Figure 2.2. After splitting the laser light in two parts of equal power using a 50/50 beam splitter (BS), each beam is transmitted through an acousto optic modulator (AOM), which shifts the frequency of the first beam to $f_1 = f_0 + 78.00 \text{ MHz}$ and the frequency of the second beam to $f_2 = f_0 + 78.01 \text{ MHz}$ in the first order Bragg diffraction, where f_0 represents the laser frequency. This leads to a heterodyne frequency of $f_h = 10 \text{ kHz}$. The driving signals of the AOMs are generated by two Direct Digital Synthesizers (DDSs) as well as two subsequent low noise linear power amplifiers.

Subsequently, both laser beams are transmitted into a vacuum chamber via two optical fibre feedthroughs featuring single mode polarisation maintaining optical fibres. In order to compensate for differential elongation between the optical fibres due to variations in ambient temperature, an analogue phase locked loop (PLL) is implemented in one of the optical paths. This PLL drives a piezo actuated mirror in order to adapt the optical path length. The piezo mechanism utilised allows a maximum linear mirror translation of $400 \mu\text{m}$, which proved to be more than enough for this application. In order to avoid excitation at and above the resonance frequency of the mechanism, the bandwidth of the control loop is limited to $\approx 1 \text{ kHz}$.

Additionally, each optical path features an analogue intensity stabilisation loop (ISL), which keeps the light intensity at the interferometer input constant. The ISLs control the light

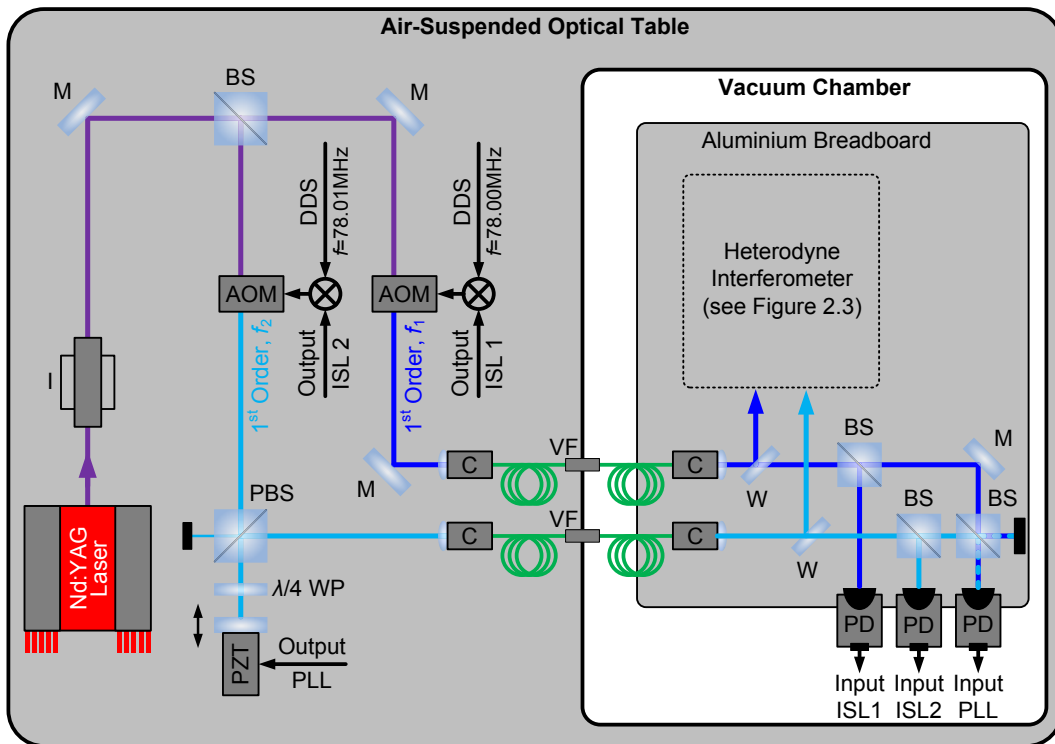


Figure 2.2: Schematic of the setup for heterodyne frequency generation including the input / output signals of the control loops. I: Isolator; M: Mirror; BS: 50/50 Beam Splitter; AOM: Acousto Optic Modulator; PBS: Polarising Beam Splitter; WP: Wave Plate; PZT: Piezo Actuator; C: Collimator; VF: (Optical Fibre) Vacuum Feedthrough; W: Window; PD: Photo Detector; PLL: Phase Locked Loop; ISL: Intensity Stabilisation Loop; DDS: Direct Digital Synthesizer;

intensity by adjusting the amplitude of the individual AOM driving signal, which directly couples to its diffraction efficiency. The ISL bandwidth currently applied is limited to ≈ 200 Hz, which is sufficient to compensate for thermally driven intensity changes in the optical setup. Important to notice is that an implementation of ISLs is only required, when sub-nm and sub- μ rad measurement accuracies are targeted, since intensity variations measurably couple to phase at this accuracy level. All three control loops utilised feature a proportional and integral (PI) control scheme.

The optical setup of the interferometer is placed on an aluminium breadboard (cast and heat-treated for reduced internal stress), which is located in a vacuum chamber in order to reduce air fluctuations during measurement. The residual pressure is at the low 10^{-5} mbar level. A schematic of the interferometer's optical setup is depicted in Figure 2.3 and a photograph is depicted in Figure 2.4. The (intensity stabilised) input laser beams of frequency f_1 and f_2 are each split into a parallel beam pair by two energy separator cubes (ESCs) with a separation of $y_s \approx 4.5$ mm. Beam pair 1 at frequency f_1 represents the interferometer's measurement and reference laser beam and is reflected at a polarising beam splitter (PBS) onto the test mirror. They pass a $\lambda/4$ wave plate (WP) twice, once before and once after being reflected, thus changing their linear polarisation state. Further on, the beam pair is transmitted through the PBS and afterwards superimposed with beam pair 2 at frequency f_2 at a 50/50 BS in order to generate a heterodyne signal at frequency f_h . This interferometer design offers highly

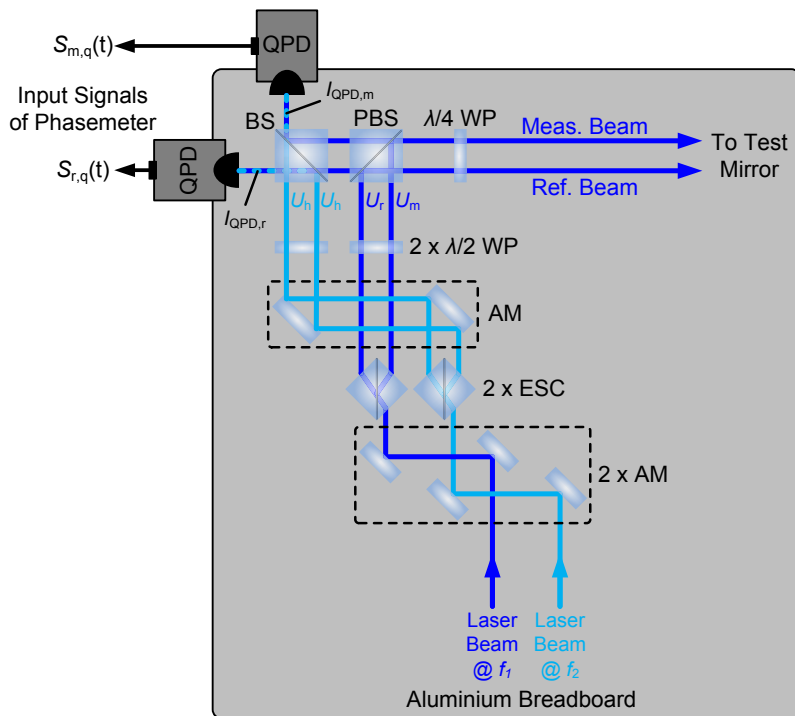


Figure 2.3: Schematic of the heterodyne interferometer's optical setup. AM: Set of (adjustable) Alignment Mirrors; ESC: Energy Separator Cube; WP: Wave Plate; BS: 50/50 Beam Splitter; PBS: Polarising Beam Splitter; QPD: Quadrant Photo Detector; $S_{m,r}$: QPD Output Signal;

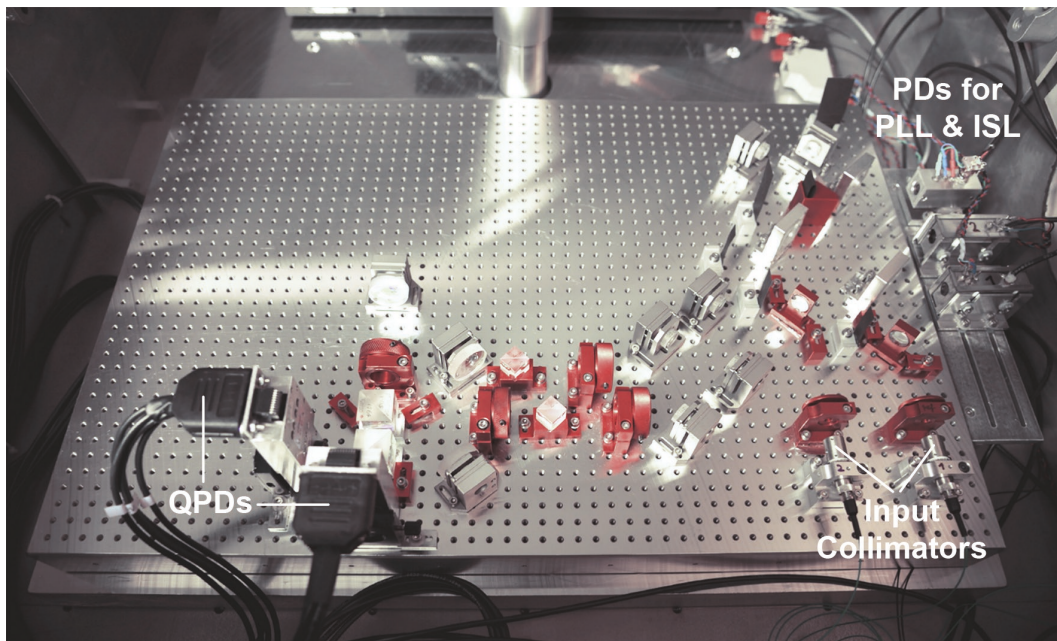


Figure 2.4: Photograph of the optical setup of the heterodyne interferometer employed.

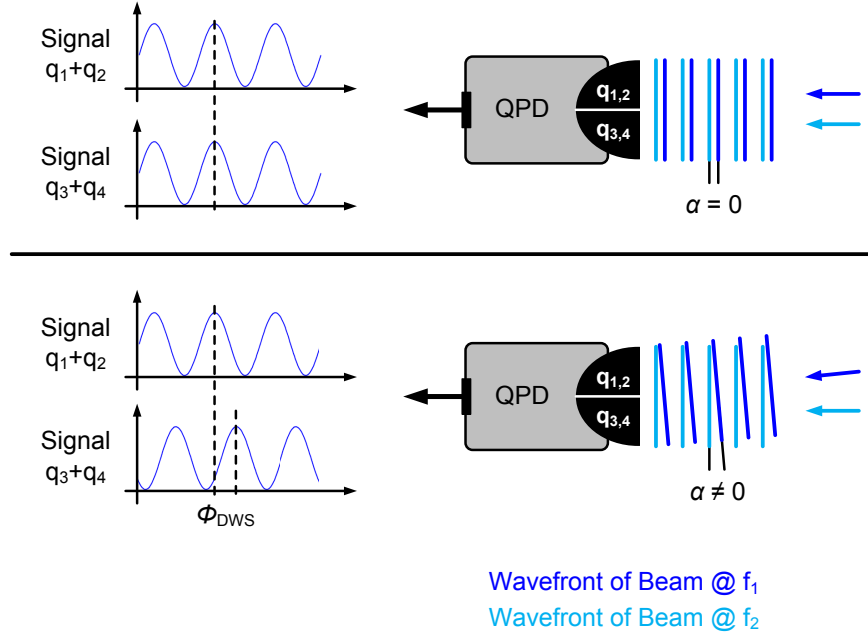


Figure 2.5: Principle of differential wavefront sensing (DWS), enabled by a quadrant photo detector (QPD). A wavefront tilt α leads to a differential phase shift ϕ_{DWS} between the output signals of the individual QPD quadrants (q_1 to q_4), which is detected and used to calculate α .

symmetric optical paths for excellent common mode rejection of thermally driven effects, like changes in optical path length or changes in refractive indices.

The measurement and the reference laser beam in the interferometer are each detected by a QPD, enabling besides the measurement of linear wavefront displacements also the measurement of wavefront tilts $\alpha_{m,r}$ when applying the differential wavefront sensing (DWS) technique [45, 46] illustrated in Figure 2.5. As the name suggests, the active area of a QPD's photo diode is divided into four individual segments, called quadrants, arranged in a 2×2 array and separated by a small gap. A relative wavefront tilt α between the (superimposed) laser beams introduces a differential linear wavefront displacement, which is detected by the QPD and results in a differential phase shift ϕ_{DWS} between the output signal of the individual QPD quadrants. Based on this phase shift the wavefront tilt α can be calculated.

Each QPD detects the interference signal between the two laser beams of frequency f_1 and f_2 , which can mathematically be described by a superposition. The analytical fields of the measurement and the reference laser beam $U_{m,r}$ (both at frequency f_1) are given by

$$U_m(t) = \sqrt{I_1} \cdot e^{i(2\pi f_1 t - \phi_m(t) - \phi_1(t))} \quad (2.1)$$

$$U_r(t) = \sqrt{I_1} \cdot e^{i(2\pi f_1 t - \phi_r(t) - \phi_1(t))} \quad (2.2)$$

when assuming identical field amplitudes. Whereas the analytical fields of the heterodyne laser beams U_h (both at frequency f_2) are given by

$$U_h(t) = \sqrt{I_2} \cdot e^{i(2\pi f_2 t - \phi_2(t))}. \quad (2.3)$$

Herein $\sqrt{I_{1,2}}$ represent the field amplitudes, $\phi_{1,2}$ represent the initial field phases and $\phi_{m,r}$ represent the field phases of measurement and reference laser beam including topography induced and tilt induced linear wavefront displacements, generated by the test mirror. These phases can also be expressed as $\phi_m(t) = \vec{k}_m \cdot \vec{l}_m(t)$ and $\phi_r(t) = \vec{k}_r \cdot \vec{l}_r(t)$, with $\vec{k}_{m,r}$ representing the propagation vectors and $\vec{l}_{m,r}$ representing the corresponding wavefront displacement vectors (the optical pathlength) of measurement and reference laser beam.

In the interferometer, one QPD detects the (superimposed) light including the measurement laser beam $I_{\text{QPD},m}$, and another QPD detects the (superimposed) light including the reference laser beam $I_{\text{QPD},r}$, which can be described by

$$\begin{aligned} I_{\text{QPD},m} &= \left\langle |\Re \{U_m(t) + U_h(t)\}|^2 \right\rangle_t \\ &= I_1 + I_2 + 2\sqrt{I_1 I_2} \cdot C_{\eta,m} \cdot \cos(2\pi f_h t + \phi_m(t) - \phi_0) \end{aligned} \quad (2.4)$$

$$\begin{aligned} I_{\text{QPD},r} &= \left\langle |\Re \{U_r(t) + U_h(t)\}|^2 \right\rangle_t \\ &= I_1 + I_2 + 2\sqrt{I_1 I_2} \cdot C_{\eta,r} \cdot \cos(2\pi f_h t + \phi_r(t) - \phi_0) \end{aligned} \quad (2.5)$$

when defining $\phi_0 = \phi_2(t) - \phi_1(t)$ and $\phi_0 \approx \text{const}$, due to the symmetric optical paths in the interferometer as well as the PLL employed. The time-related averaging is introduced for considering the limited bandwidth of the QPDs with respect to the laser frequency and the coefficient $C_{\eta,m,r}$ accounts for the heterodyne efficiency of the superposition.

In the presented setup, each QPD quadrant is detecting $\approx 1/4$ of the light intensity, if the beam quality as well as the beam alignment is ideal, and converts it into a proportional electrical signal $S_{m,r}$. The proportionality factor of the conversion is defined by the quadrant diode's responsivity as well as the gain of the subsequent transimpedance amplifier and affects the offset values $O_{m,r}$ and amplitudes $A_{m,r}$ of each electrical signal, which is given by

$$S_{m,q}(t) = O_{m,q} + A_{m,q} \cdot \cos(2\pi f_h t + \phi_{m,q}(t) - \phi_0) \quad (2.6)$$

$$S_{r,q}(t) = O_{r,q} + A_{r,q} \cdot \cos(2\pi f_h t + \phi_{r,q}(t) - \phi_0) \quad (2.7)$$

where $q \in \{1, 2, 3, 4\}$ represents the QPD quadrant index. Further on, these signals are low-pass filtered by a 6th order Bessel filter with a corner frequency of 20 kHz and subsequently fed into the digital phasemeter. This phasemeter comprises two parts, the first part is a program implemented on a field programmable gate array (FPGA) card, which generates the signals for an in-phase and quadrature data analysis. The second part is a host program, running on a PC, which calculates the phase and displacement values for each QPD quadrant. Both programs are based on the software LabVIEW (by National Instruments). A schematic of their structure and interaction is displayed in Figure 2.6.

The FPGA card features eight 16 bit onboard analog-to-digital converters (ADCs) running at the sampling frequency $f_{s,1} = 160$ kHz, which are used to digitize the time continuous QPD signals into time-discrete signals depending on the (index) variable k_1 with $k_1 \in \mathbb{N}$ and $k_1 = t \cdot f_{s,1}$ given by

$$S_{m,q}(k_1) = O_{m,q} + A_{m,q} \cdot \cos\left(2\pi \frac{f_h}{f_{s,1}} k_1 + \phi_{m,q}(k_1) - \phi_0\right) \quad (2.8)$$

$$S_{r,q}(k_1) = O_{r,q} + A_{r,q} \cdot \cos\left(2\pi \frac{f_h}{f_{s,1}} k_1 + \phi_{r,q}(k_1) - \phi_0\right). \quad (2.9)$$

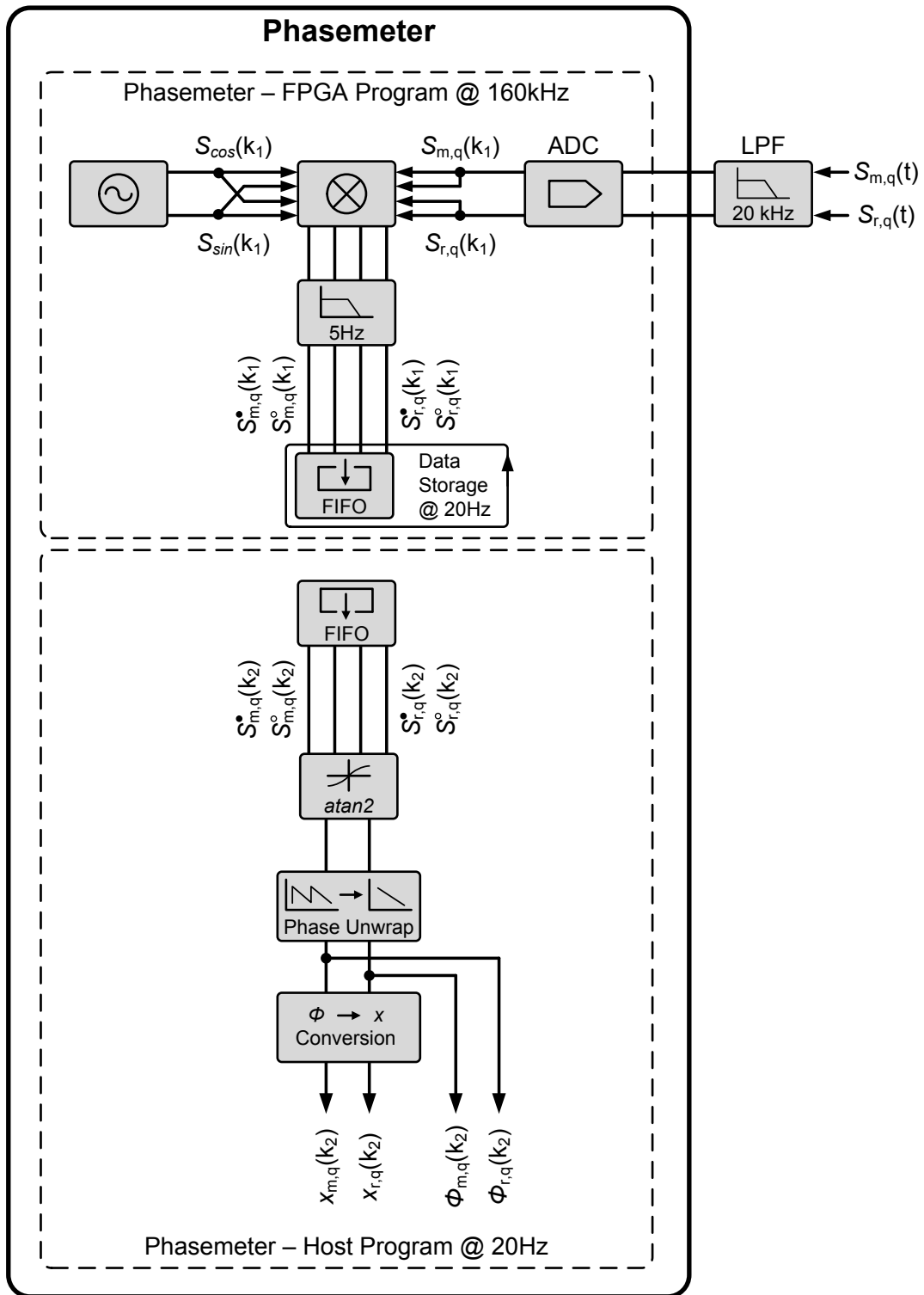


Figure 2.6: Schematic of the interferometer’s phasemeter, which is divided into two parts. One part is implemented on a field programmable gate array (FPGA) card and includes the in-phase and quadrature signal generation. The second part runs on a PC and includes the phase $\phi_{m,r}$ and displacement $x_{m,r}$ calculation of each QPD quadrant.

In line with the in-phase and quadrature analysis employed, each signal $S_{m,r}$ is mixed with an internally generated cos and sin oscillator signal S_{\cos} and S_{\sin} , both of amplitude A_i and frequency f_h , leading to the in-phase signals $S_{m,r}^\bullet$ and the quadrature signal $S_{m,r}^\circ$. All signals are subsequently low pass filtered by a digital 2nd order Butterworth filter with a corner frequency at 5 Hz in order to suppress the fast oscillating signal parts at $2f_h$ and to avoid aliasing effects during the subsequent data storage described by

$$\begin{aligned} S_{m,q}^\bullet(k_1) &= f_{\text{LPF}}[S_{m,q}(k_1) \cdot S_{\cos}(k_1)] \\ &= \frac{1}{2}A_{m,q}A_i \left(\cos(\phi_{m,q}(k_1) - \phi_0 - \phi_i) \right) \end{aligned} \quad (2.10)$$

$$\begin{aligned} S_{m,q}^\circ(k_1) &= f_{\text{LPF}}[S_{m,q}(k_1) \cdot S_{\sin}(k_1)] \\ &= \frac{1}{2}A_{m,q}A_i \left(\sin(\phi_{m,q}(k_1) - \phi_0 - \phi_i) \right) \end{aligned} \quad (2.11)$$

$$\begin{aligned} S_{r,q}^\bullet(k_1) &= f_{\text{LPF}}[S_{r,q}(k_1) \cdot S_{\cos}(k_1)] \\ &= \frac{1}{2}A_{r,q}A_i \left(\cos(\phi_{r,q}(k_1) - \phi_0 - \phi_i) \right) \end{aligned} \quad (2.12)$$

$$\begin{aligned} S_{r,q}^\circ(k_1) &= f_{\text{LPF}}[S_{r,q}(k_1) \cdot S_{\sin}(k_1)] \\ &= \frac{1}{2}A_{r,q}A_i \left(\sin(\phi_{r,q}(k_1) - \phi_0 - \phi_i) \right) \end{aligned} \quad (2.13)$$

where f_{LPF} represents the filter function of the 2nd order Butterworth filter and ϕ_i represents the initial phase of S_{\cos} and S_{\sin} , respectively.

The signals are stored in a FIFO memory at 20 Hz and are read-out by the host program at a matched sampling frequency $f_{s,2} = 20$ Hz, leading to signals depending on a new (index) variable k_2 with $k_2 \in \mathbb{N}$ and $k_2 = t \cdot f_{s,2}$. This host program calculates the phase of each QPD quadrant signal $\phi_{m,r}$ by applying the atan2 function to both, the in-phase and quadrature signals, described by

$$\phi_{m,q}(k_2) = \text{atan2} \left[S_{m,q}^\circ(k_2), S_{m,q}^\bullet(k_2) \right] \quad (2.14)$$

$$\phi_{r,q}(k_2) = \text{atan2} \left[S_{r,q}^\circ(k_2), S_{r,q}^\bullet(k_2) \right]. \quad (2.15)$$

Herein the initial phases ϕ_0 and ϕ_i are assumed to be 0. The host program also counts the number of phase jumps $n_{m,r}$ in each signal, increasing the dynamic range of the phasemeter to values $> \pm\pi$. Subsequently, the phase signals are converted into a proportional linear displacement signal $x_{m,r}$ given by

$$x_{m,q}(k_2) = \frac{\phi_{m,q}(k_2) \lambda_0}{4\pi n_{m,q}(k_2)} \quad (2.16)$$

$$x_{r,q}(k_2) = \frac{\phi_{r,q}(k_2) \lambda_0}{4\pi n_{r,q}(k_2)}, \quad (2.17)$$

which represent the displacement in the measurement and reference laser beam introduced by the test mirror surface topography and parasitic test mirror movements (in measurement direction) due to an actuation with the pendulum mechanism.

In order to quantify the performance of the setup, a measurement is conducted in which measurement and reference laser beam are reflected on the static, non moving test mirror. The result is depicted in Figure 2.7 in form of an amplitude spectral density (ASD) of the differential linear displacement between measurement and reference laser beam $x(k_2) = x_m(k_2) - x_r(k_2)$, representing the interferometer's displacement noise with

$$x_m(k_2) = \frac{1}{4} \sum_{q=1}^4 x_{m,q}(k_2) \quad (2.18)$$

$$x_r(k_2) = \frac{1}{4} \sum_{q=1}^4 x_{r,q}(k_2). \quad (2.19)$$

The results show values at the low pm level at frequencies down to $\approx 3 \cdot 10^{-2}$ Hz and raising with an $1/f$ slope at lower frequencies. This behaviour is attributed to thermal fluctuations within the setup.

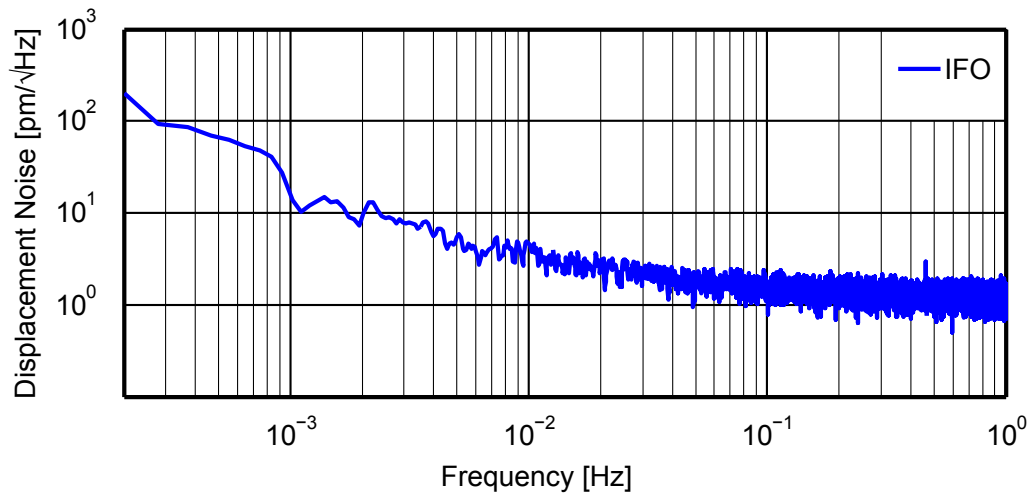


Figure 2.7: Performance of the measurement setup. Depicted is the ASD of the interferometer's displacement noise with values at the low pm level at frequencies down to $\approx 3 \cdot 10^{-2}$ Hz and raising with an $1/f$ slope at lower frequencies.

2.1.1.2 Pendulum Mechanism

In order to move the test mirror lateral with respect to the output laser beams of the interferometer, a customised mechanism has been manufactured, depicted in Figure 2.8. This mechanism is made of an aluminium alloy and features a flexure hinge at its top, which defines the axis of rotation of the kinematic trace of the test mirror. The test mirror itself is mounted in an attachable mirror support, which employs a low stress mounting concept, minimising internal stress, hence surface deformation. The driving force is generated by a NEXLINE linear piezo stepping actuator (by Physik Instrumente) featuring a maximum actuation range of $y_{a,\max} = 5$ mm.

The initial hinge design is displayed in Figure 2.9 (left). Its shape is defined by two triangular slots, hence offering a well defined (small) deformation area. The minimal thickness of the hinge is 0.8 mm, which was demanded by the manufacturer due to the choice of material (aluminium alloy EN-AW7075) as well as the manufacturing method applied (electrical discharge machining). Some advantages of flexure hinges are:

- A simple design consisting of only one monolithic part.
- A precise movement, since flexures can be manufactured very accurately, hence reducing coupling between the individual DoFs and therefore minimising parasitic movements.
- A highly reproducible movement, since flexures are free of backlash. However it is mandatory to use them within the material's linear-elastic range.
- Low friction since they only feature internal friction at an atomic level, caused by elastic deformation.

An estimation of the internal stress in the hinge is performed with the help of the finite element method (FEM) simulation tool implemented in Inventor (by Autodesk). The mesh employed consists of tetrahedron elements with midside nodes (cubic approach). A mesh refinement of the deformation area is applied in order to get realistic results. The calculated equivalent tensile stress in the hinge for a linear FEM simulation, including an actuation of 5 mm (at the point of force application) shows considerably higher values than the elastic limit of the aluminium alloy employed given at $R_e = 385 \text{ MPa}$. This means in first instance that the calculated results are invalid, since a non-linear FEM simulation is required in order to obtain representative values for a plastic deformation. However, since the flexure hinge should be operated within its elastic range in order to ensure reproducible movements, this result calls either for a change in material (for example a titanium alloy) or a re-design with reduced stress levels.

Considering the costs, the latter solution was chosen, which led to a re-designed flexure hinge, represented by two $\varnothing 38 \text{ mm}$ bores, see Figure 2.9 (right). This new design is easy to manufacture and reduces the internal stress in the hinge, due to a reduced notch effect. The design also features an increased deformation area, which helps distributing the load over a larger extent of the hinge. On the other hand, this increased deformation area leads to a more complex kinematics of the mechanism. But it is expected that this effect will not reduce the reproducibility of the movement and thus is acceptable. This assumption is additionally supported when considering an averaging of the surface topography over the cross section of the laser beams involved in the measurements. The resulting equivalent tensile stress in the re-designed hinge is now reduced to $\sigma \approx 250 \text{ MPa}$ for a linear FEM simulation with an identical actuation of 5 mm (at the point of force application) as applied before. This result is well below the elastic limit of the material employed leading to a reasonable factor of safety of $s_F = R_e/\sigma \approx 1.5$. The new hinge design is manufactured via electrical discharge machining realising a tolerance $< 0.01 \text{ mm}$ in thickness, which ensures a defined test mirror movement with low DoF coupling, hence low parasitic movements.

The attachable mirror support is designed to accommodate two $\varnothing 25 \text{ mm}$ test mirrors and is also made of an aluminium alloy. First measurements are performed with measurement and reference laser beam aligned onto the same test mirror, since this configuration does not involve major changes to the optical design of the setup. This addresses in particular the separation between the beams, which is originally set to $\approx 4.5 \text{ mm}$. Only if the measurement

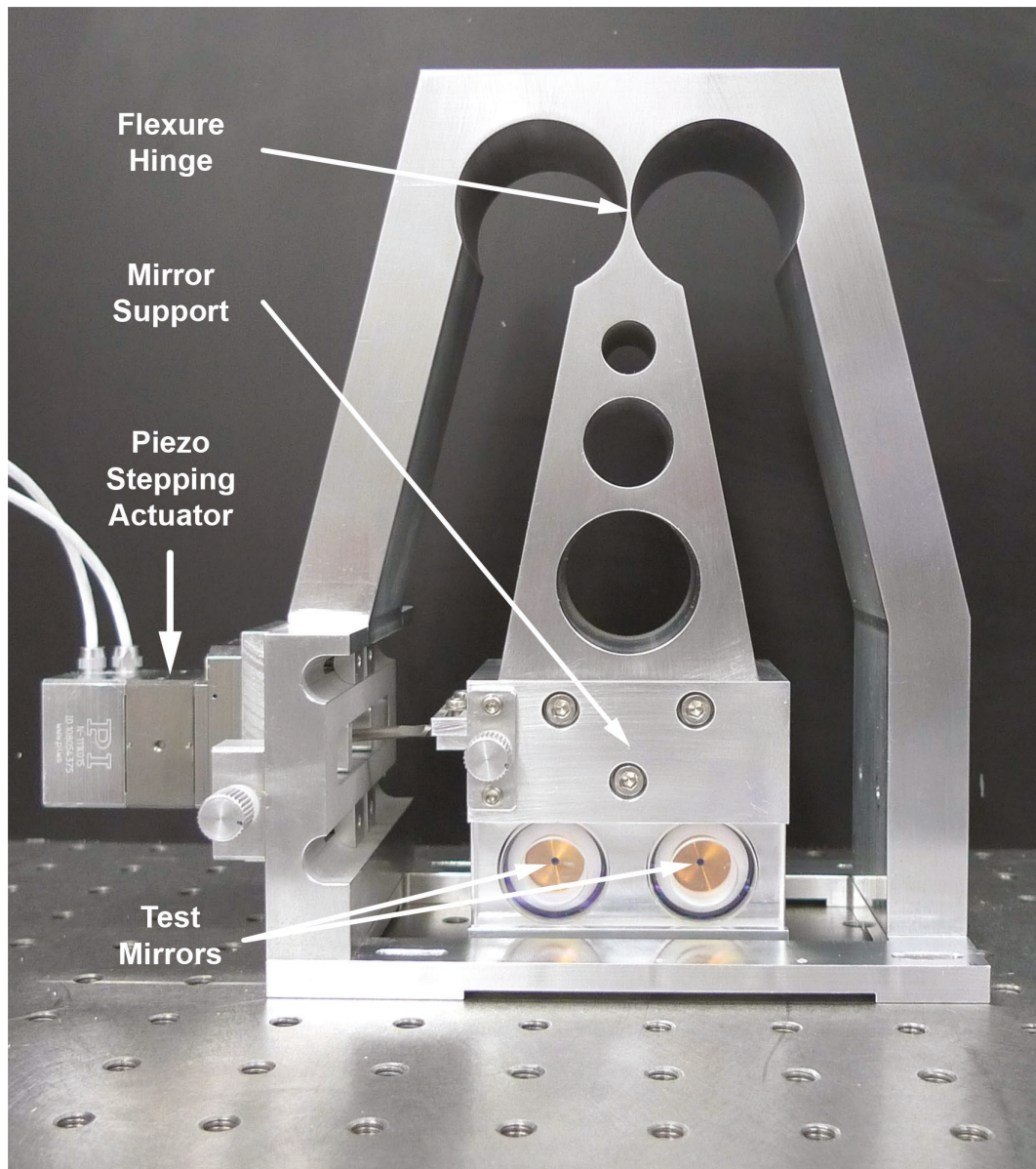


Figure 2.8: Photograph of the pendulum mechanism, which provides a precise guidance of the test mirrors during movement. The mechanism is driven by a NEXLINE linear piezo stepping actuator.

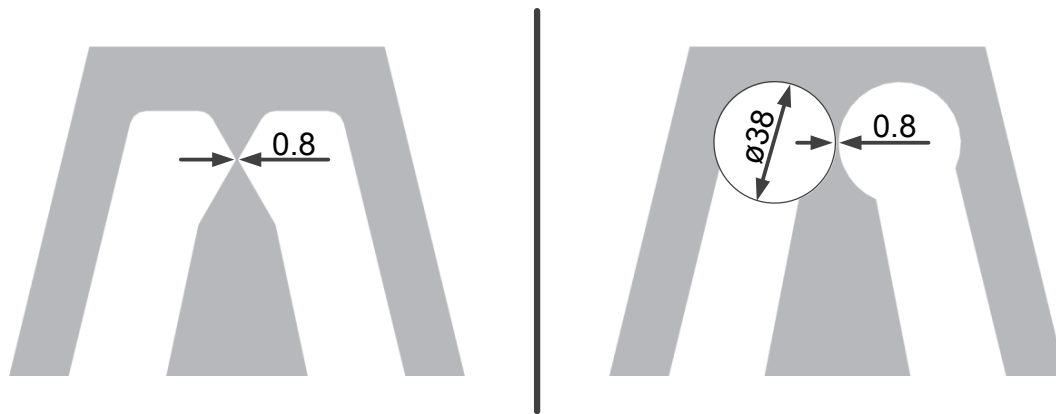


Figure 2.9: Rendering of the initial hinge design (left), represented by two triangular slots. This design features a defined (small) deformation area, but is subject to high internal stress. The final hinge design (right) is represented by two bores ($\varnothing 38$ mm). This design features a reduced notch effect as well as a larger deformation area, hence reduced internal stress.

results show correlation effects - potentially generated by surface regularities of the test mirror due to manufacturing - the measurement configuration will be changed to separate test mirrors for the laser beams involved.

The support of the test mirrors is realised by a low-stress mounting concept, depicted in Figure 2.10. Hereby, the outer ring area of each test mirror is pressed against a (common) limiting plate made of fused quartz with a flatness of $\lambda/10$. This solution ensures a parallel orientation of the test mirror surfaces as well as low surface deformations due to a reduced, homogeneous areal load. Thereby the clamping force is generated by screws and transferred via a Teflon ring as well as an elastic O-ring onto the backside of the corresponding test mirror. In this configuration, the Teflon ring is used to reduce torsional stress and the elastic O-ring to generate a homogeneous load as well as compensating for differential thermal expansion between the mounting parts.

The pendulum mechanism is driven by a NEXLINE linear piezo stepping actuator (by Physik Instrumente), see Figure 2.8. Its operating principle is based on the coordinated motion of two piezo stack pairs, which drive a runner. Each piezo stack consists of a contraction actuator segment for clamping / unclamping the runner and a shear actuator segment for driving the runner. This configuration enables two actuation modes:

- An analogue mode in which all piezo stack pairs work simultaneously. Its principle is depicted in Figure 2.11 (top). The contraction actuator segments (of both piezo stack pairs) are activated and clamping the runner, while the shear actuator segments are driving the runner. Maximum actuation range in this mode is $2.5 \mu\text{m}$.
- A stepping mode in which all piezo stack pairs work in a coordinated movement of their contraction and shearing segments. Its principle is depicted in Figure 2.11 (bottom). Piezo stack 1 is clamping and driving the runner, while piezo stack 2 (in unclamped condition) moves back towards the initial position. When reaching the travel limit of the shear segment, piezo stack 1 unclamps and starts moving back to its initial position while piezo stack 2 is clamping the runner and continues its movement. Maximum actuation range in this mode is 5mm .

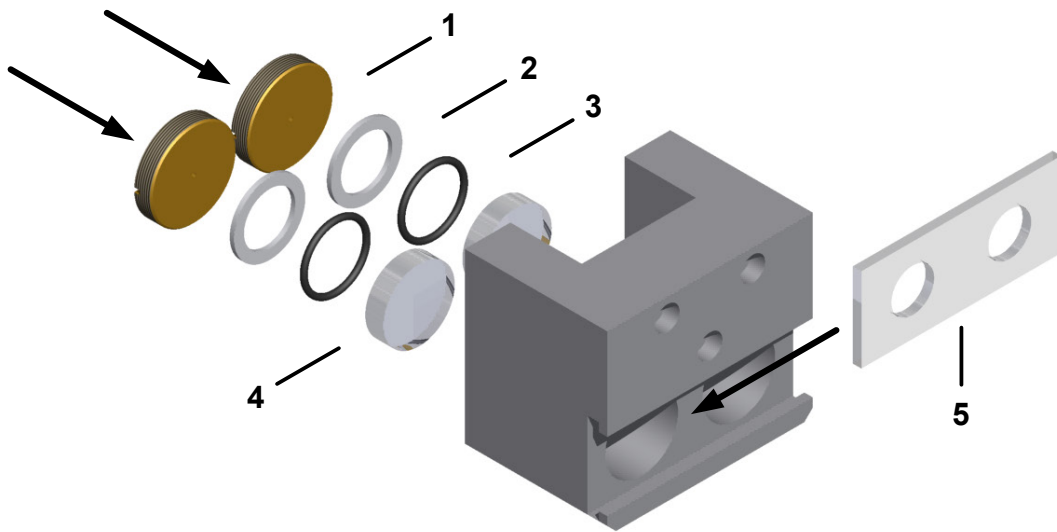


Figure 2.10: Rendering of the mirror support including its low-stress mounting concept of the test mirrors. 1: Clamping Screws; 2: Teflon Rings (for minimising torsional stress); 3: Elastic O-rings (for homogeneous load distribution and compensation of differential thermal expansion between the mounting parts); 4: Test Mirrors; 5: Limiting Plate (for parallel alignment of the test mirror surfaces).

The driving program of the piezo actuator is based on the software LabVIEW (by National Instruments) and is implemented in the interferometer's host program. This configuration simplifies a simultaneous sampling of the interferometer signals and the encoder signals of the piezo actuator for position and velocity. This integrated encoder features a resolution of 5 nm, hence ensuring a precise position determination of the test mirror.

In analogue mode the runner of the piezo actuator moves without parasitic movements. However, in stepping mode the piezo actuator shows some unique characteristics, see Figure 2.12. During handover between the piezo stacks, the clamping and unclamping processes introduce parasitic movements of the runner in displacement and tilt in the order of $\approx 2 \mu\text{m}$ and $\approx 40 \mu\text{rad}$ respectively. These parasitic movements are independent of the driving speed and occur regularly every $\approx 3.3 \mu\text{m}$ of travel distance. Since they will generate error movements of the test mirror, they are avoided by driving the pendulum in steps, in which the measurements are only performed in static condition between movement.

The driving force of the piezo actuator is transmitted to the pendulum via an actuation bar made of a titanium alloy (Ti3.7164), which is depicted in Figure 2.13. It features two integrated cardan hinges in form of flexures with a thickness of 0.6 mm, which compensate the (varying) offset between the actuator and the point of force application on the mirror support during actuation. Additionally, the cardan hinges reduce the impact of the parasitic movements of the actuator's runner in stepping mode, due to its flexibility.

Manufacturing tolerances of the mechanism generate additional error movements of the test mirror, since they introduce an offset / an inclined direction of the driving force. In particular parasitic tilts are most critical, since they introduce non-common-mode contributions to the displacement in measurement direction, which have to be considered in order to reduce measurement errors. These parasitic tilts can be corrected using the DWS signals of the interferometer, at least up to $\approx \pm 1 \text{ mrad}$. Beyond that limit, the DWS signals are subject to a non-linear response and can not be corrected easily. That is why the pendulum mechanism

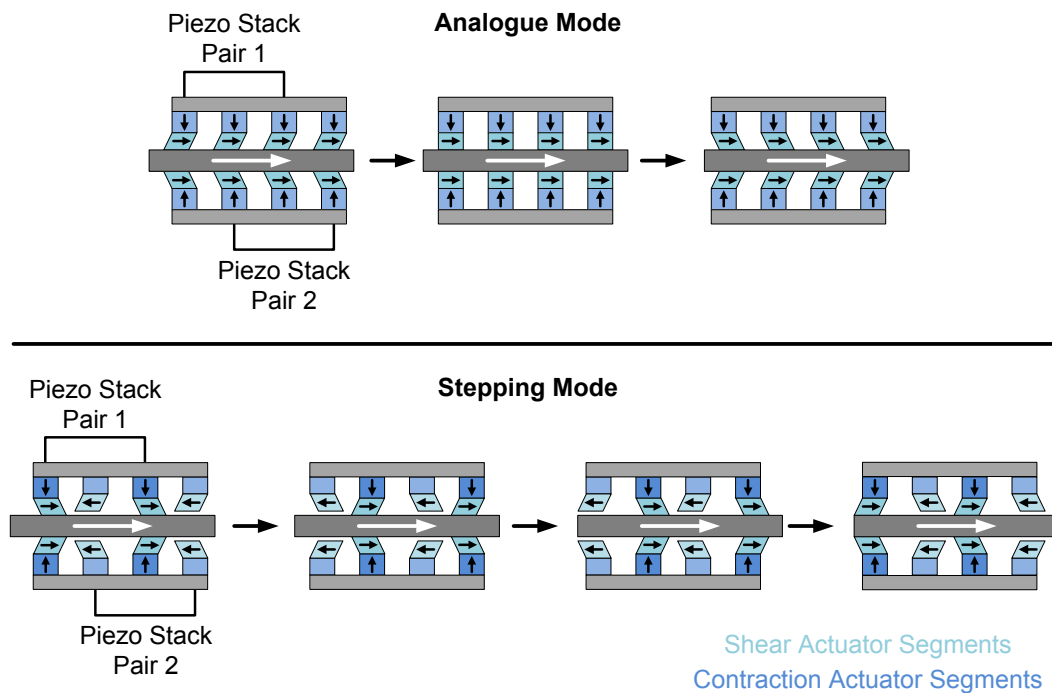


Figure 2.11: Principle of the two different driving modes of the NEXLINE linear piezo stepping actuator. In analogue mode all piezo stack pairs work simultaneously (top), whereas in stepping mode all piezo stack pairs work in a coordinated movement of their contraction and shearing segments (bottom).

is equipped with two adjusters for separate positioning of the piezo actuator as well as the point of force application on the mirror support, which enable an alignment of the driving force, if required.

2.1.2 Measurements & Results

First, the measurement and reference laser beam are characterised, since their cross-section (defined by the diameter $d_{m,r}$) on the test mirror surface introduce a low-pass filter effect, which has a major influence in the measurement results as well as the selection of an appropriate actuation step size of the pendulum mechanism. Further on, the characterisation of the test mirror surface is presented, in which both laser beams are aligned onto the same (common) test mirror. This configuration is applicable, since there are no surface correlation effects evident / observed in the measurement results. Additional measurements are performed in order to investigate the influence of different measurement configurations, especially the correlation between the laser beam sizes on the test mirror surface and their impact in lateral resolution. Finally, a validation of the results is conducted, which includes a comparison of the presented interferometric measurements with comprehensive measurements performed by the Physikalisch-Technische Bundesanstalt (PTB) applying interference microscopy. The validated results are used to calibrate a (theoretical) surface model of the test mirror topography, which will be the basis for the piston estimation in the LISA IFP wide-field telescope.

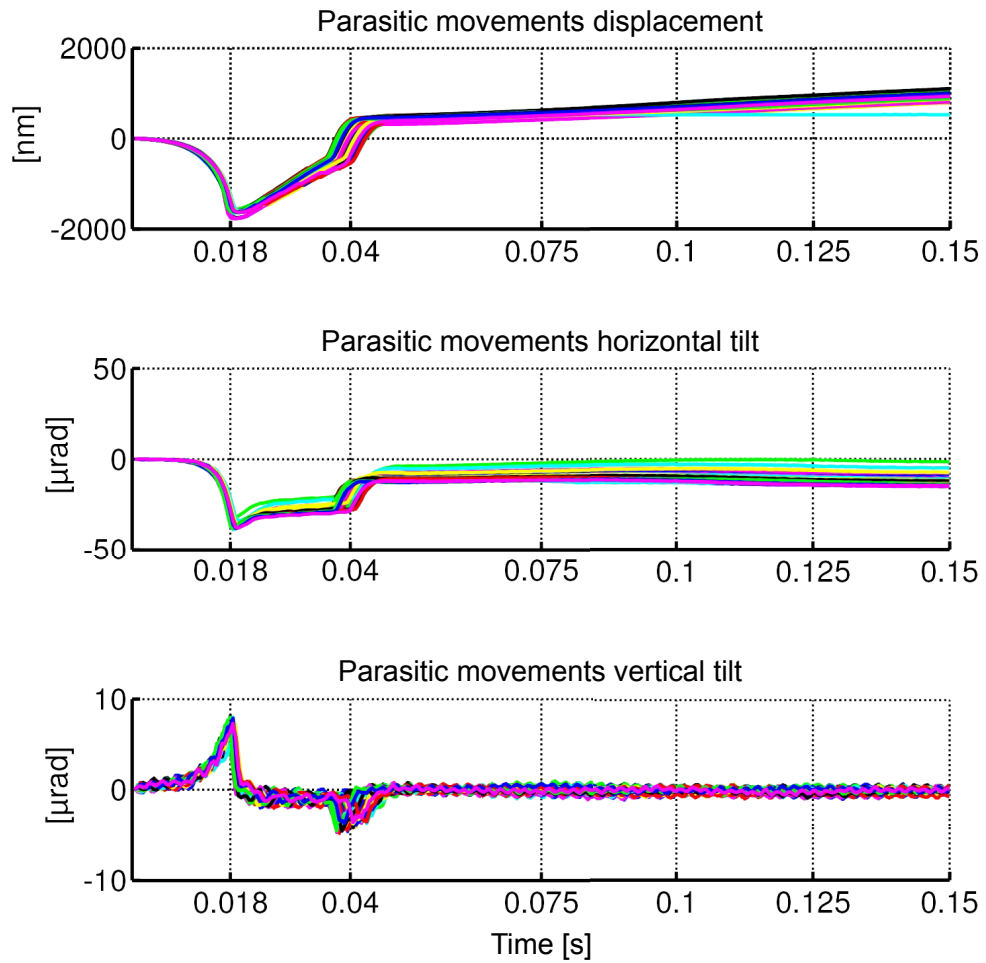


Figure 2.12: Parasitic movements of the piezo actuator's runner during handover of the piezo stacks. These parasitic movements occur solely in stepping mode and appear every $\approx 3.3 \mu\text{m}$ of travel distance.

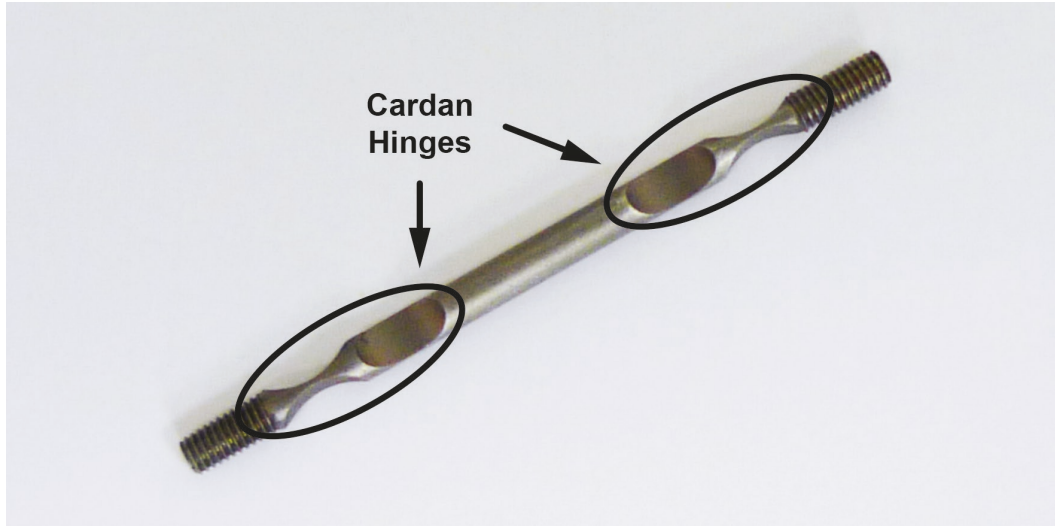


Figure 2.13: Photograph of the actuation bar, which transmits the driving force of the piezo actuator to the pendulum. The integrated cardan hinges compensate the (varying) offset between the actuator and the point of force application on the mirror support during actuation.

2.1.2.1 Laser Beam Characterisation

In order to interpret the measurement results correctly, it is mandatory to estimate the sizes of the measurement and reference laser beam on the test mirror surface as their diameters $d_{m,r}$ have a large impact in the spatial resolution as well as the measured topography amplitudes of the results. Generally, the measured surface topography is averaged over the cross-section of the laser beam, which introduces a low pass filter effect, suppressing surface details at spatial frequencies smaller than $\approx 2/(\pi \cdot d_{m,r})$.

An estimation of the laser beam diameters is made based on beam characterisation via the razor blade method with the assumption that the intensity distribution $I_{m,r}$ of the laser beams under investigation is consistent with a Gaussian beam given by

$$I_G(x_b, y_b, z_b) = I_{G,\max} \frac{d_{b,0}}{d_b(x_b)} \cdot e^{-8 \left(\frac{y_b^2 + z_b^2}{d_b^2(x_b)} \right)} \quad (2.20)$$

for a position along the beam propagation direction x_b , with $I_{G,\max}$ representing the maximum intensity, $d_{b,0}$ representing the beam diameter ($1/e^2$) in the beam waist ($x_b = 0$) and d_b representing the beam diameter ($1/e^2$) dependent on the position x_b .

The optical power of a Gaussian laser beam P_b can be calculated by integrating the intensity over its section area given by

$$P_b = \int_{-\infty}^{\infty} \int_{-\infty}^{\infty} I_G(x_b, y_b, z_b) dy_b dz_b. \quad (2.21)$$

The procedure of the razor blade method involves the movement of a razor blade lateral through a laser beam, hence obstructing it at an increasing level, while the transmitted power is measured by a photo detector. When the active area / the diameter of the photo diode is considerably larger then the laser beam diameter under investigation ($d_{PD} \gg d_b$), the

normalised received power $\hat{P}_{n,b}$ as a function of the razor blade position y_c can be described by

$$\begin{aligned}\hat{P}_{n,b}(x_b, y_c) &= \frac{1}{P_b} \int_{-\infty}^{\infty} \int_{y_c}^{\infty} I_G(x_b, y_b, z_b) dy_b dz_b \\ &= \frac{1}{2} \left(\operatorname{erf} \left(2\sqrt{2} \frac{y_c}{d_b(x_b)} \right) + 1 \right).\end{aligned}\quad (2.22)$$

with the solutions

$$\begin{aligned}\hat{P}_{n,b} \left(-\frac{1}{4} d_b(x_b) \right) &\approx 0.16 \\ \hat{P}_{n,b} \left(+\frac{1}{4} d_b(x_b) \right) &\approx 0.84\end{aligned}$$

for the beam radius $r_b = d_b/2$, which is measured at the $1/\sqrt{e}$ positions of the Gaussian intensity distribution. After the analysis of the measured data, the initial beam diameters of measurement and reference laser beam d_m and d_r are both estimated to be 1.3 mm on the test mirror surface.

2.1.2.2 Surface Topography Characterisation

As mentioned earlier, the interferometer's laser beams are aligned onto the same test mirror during measurement. Due to the actuation of the pendulum mechanism, they scan over the mirror surface (each one on an individual circular line) enabling the characterisation of its surface topography ρ_{TM} .

Mathematical Model Besides individual surface topography details, the recorded displacement signals x_m (measurement beam) and x_r (reference beam) of the interferometer also include systematic and random error movements $s_{d,t}$ (due to parasitic displacements and tilts) of the mechanism, introduced by manufacturing tolerances and the piezo actuator. All error movements of the test mirror in measurement direction are suppressed by calculating the differential translation $x(k_2) = x_m(k_2) - x_r(k_2)$ between both displacement signals, since they appear in common-mode. As a reminder, k_2 still represents the index variable of the digitised signals in the phasemeter host program.

However, parasitic tilts α of the test mirror generate error contributions in the differential displacement signal, which are not suppressed and have to be considered. A correction is implemented based on the test mirror tilt, which is calculated by averaging the DWS signals of the measurement and the reference laser beam $\alpha(k_2) = (\alpha_m(k_2) + \alpha_r(k_2))/2$. Together with the known beam separation y_s , the displacement contribution x_α due to a tilt of the test mirror can be calculated by

$$x_\alpha(k_2) \approx \alpha(k_2) \cdot y_s \quad (2.23)$$

for a perfectly flat mirror surface and small angles α . This correction process is also illustrated in Figure 2.14. Furthermore, random errors introduced by the piezo actuator are reduced by averaging the results of several measurement runs.

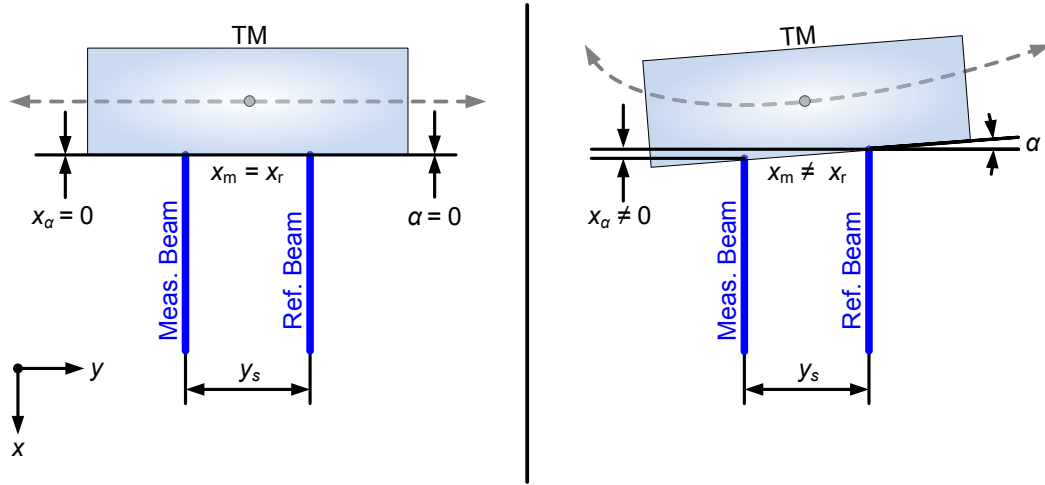


Figure 2.14: Correction process for contributions in the differential displacement signal due to parasitic tilts α of the test mirror. TM: Test Mirror; α : Tilt of Test Mirror; y_s : Beam Separation; x_m : Displacement in Measurement Beam; x_r : Displacement in Reference Beam; x_α : Displacement Contribution due to Test Mirror Tilt;

Data Analysis & Results The pendulum mechanism is actuated in steps of $10 \mu\text{m}$ every 5 s during the initial measurements, see Figure 2.15, where 2 s were used for driving and 3 s were spent in static condition. The data evaluation of the interferometer signal is only conducted during the static condition, including a data averaging over 2 s (corresponding to 40 data points) in order to minimise error contributions due to measurement noise of the interferometer.

The overall driving distance of the actuator exploited here is $y_a = 3 \text{ mm}$, leading to a movement of the test mirror centre of $l_{\text{TM}} \approx 3.5 \text{ mm}$ along its circular trajectory. A conversion of the recorded actuator position is implemented by a coordinate transformation based on a simplified polynomial approximation of the mechanism's kinematic trace, which considers besides the position of the test mirror centre c_{TM} also non-linearities introduced by a tilt of the actuation bar during movement. For details concerning the conversion see Appendix A.1. However, when only considering measurements including large laser beam sizes - as present in this case with $d_{\text{m,r}} = 1.3 \text{ mm}$ - the position errors introduced by the actuation bar can be neglected, since they are small (with just a few μm) compared to the large averaging effect of the mirror surface topography over the cross-section of the laser beams.

All measurements have been performed with a slight pre-load of the mechanism's flexure hinge in order to avoid movements around its zero point, where hysteresis effects could occur. Typical interferometer signals for displacement x and test mirror tilt α (measured via DWS) are depicted in Figure 2.16. It is clear that there is a cross coupling from the test mirror tilt to the displacement signal, degrading the measurement performance. This can be compensated using Equation 2.23, which leads to the corrected displacement $x^c(k_2) = x(k_2) - x_\alpha(k_2)$ with amplitudes at the low nm level. This corrected signal is assumed to be mainly generated by surface topography induced displacements in measurement and reference laser beam.

The measured (corrected) signals x^c for several runs of the initial measurement configuration (Figure 2.17, configuration **A**) are depicted in Figure 2.18 (top) including their average. The figure also displays the deviation ϵ of each run with respect to the average signal, which shows

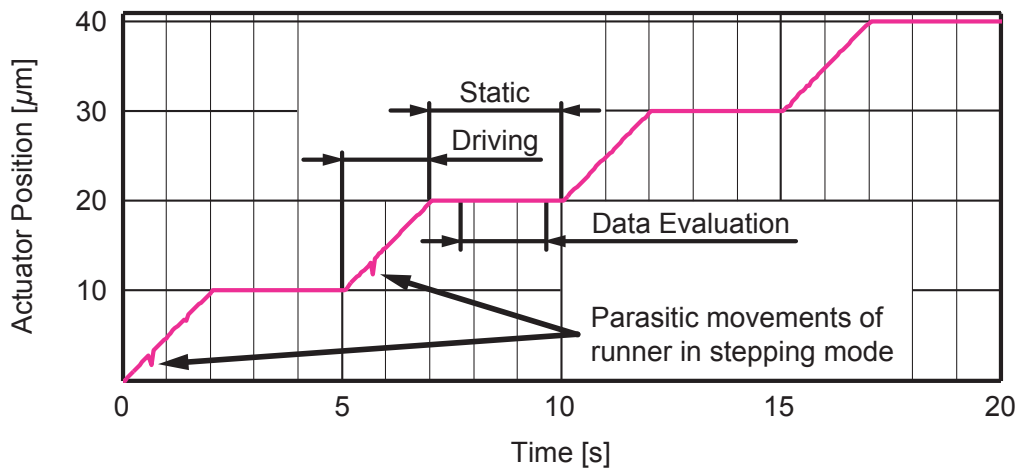


Figure 2.15: Example of the movement pattern of the piezo actuator, which is driven in steps. The data evaluation is conducted in static condition, which reduces error contributions in the recorded data, due to parasitic movements of the actuator's runner in stepping mode.

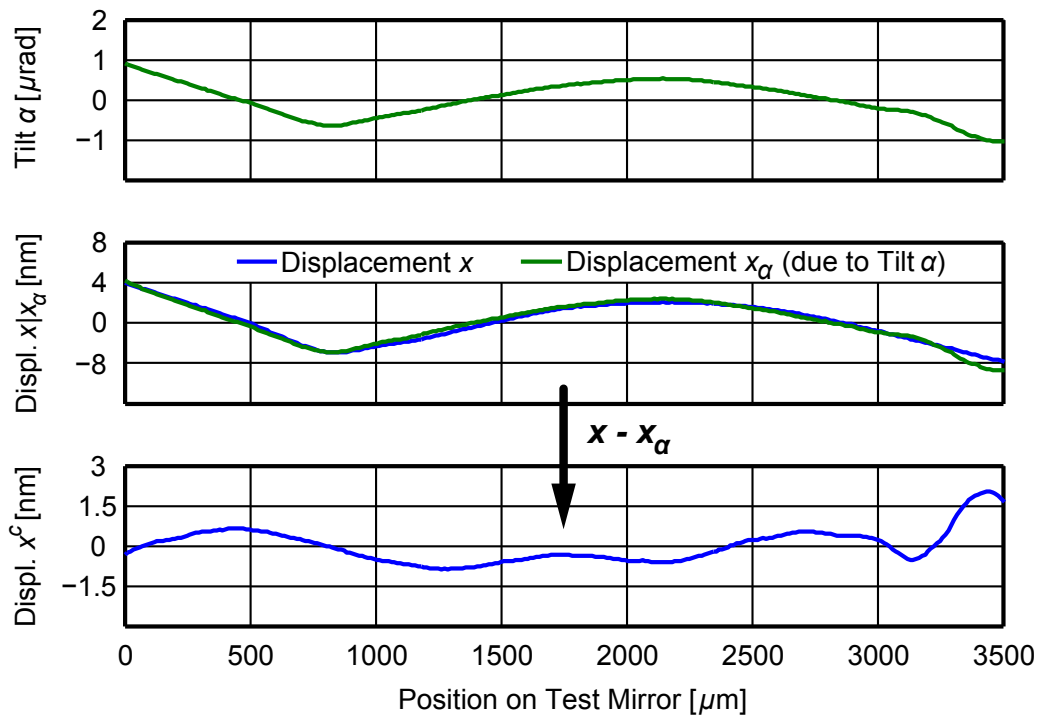


Figure 2.16: Measured test mirror tilt α (top) and the measured (differential) displacement x as well as the calculated displacement x_α , which represents the error contributions in x due to test mirror tilt α (middle). The corrected displacement $x^c(k_2) = x(k_2) - x_\alpha(k_2)$ (bottom) represents a signal, which is directly coupled to the test mirror surface topography ρ_{TM} however, does not represent it. This is due to the fact that it contains both, surface topography induced displacements of the measurement as well as the reference laser beam.

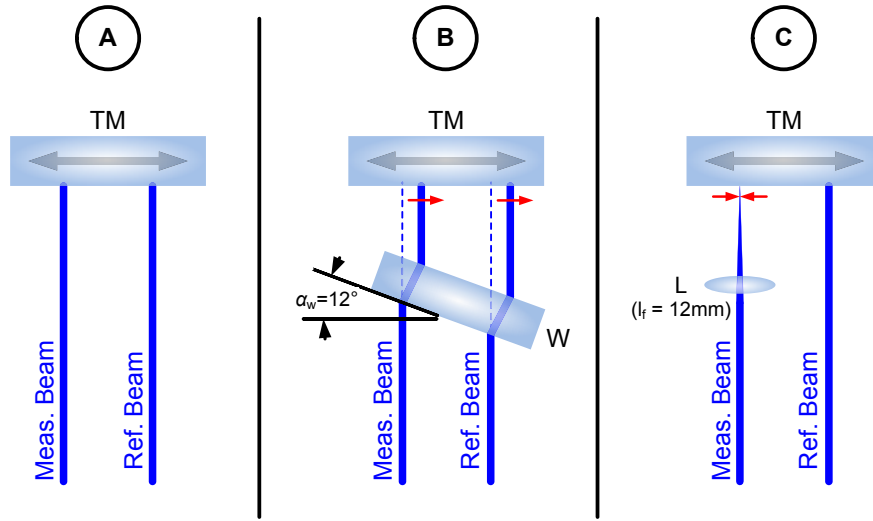


Figure 2.17: Overview of the three different measurement configurations employed. Configuration **A** (left) represents the initial configuration. Configuration **B** (middle) includes a tilted (plane-parallel) window for proving the validity of the measurement results. Configuration **C** (right) includes an aspheric lens for increasing the lateral resolution of the measurements.

that the results are highly reproducible, especially when considering the long measurement durations of ≈ 1500 s per run.

In order to quantify the reproducibility, the standard deviation σ is calculated based on the deviation values and is stated in the individual legend, featuring values in the order of ≈ 20 μm . In a subsequent measurement these results are validated with respect to the previous assumption that their main contribution is indeed generated by the test mirror surface topography and not by systematic error motions of the pendulum mechanism. Therefore a (plane-parallel) window made of BK-7 with a thickness of $l_w = 6.35$ mm is placed - at a small angle of $\alpha_w \approx 12^\circ$ - into both laser beams (Figure 2.17, configuration **B**), introducing an equal lateral offset y_w of measurement and reference laser beam. Using Snell's law the offset yields to

$$y_w \approx l_w \cdot \sin(\alpha_w) \left(1 - \frac{n_a}{n_w} \right) \quad (2.24)$$

resulting in $y_w \approx 450$ μm , when considering the refractive index of air ($n_a = 1$) and BK-7 ($n_w = 1.52$). The measurement results are depicted in Figure 2.18 (bottom) and show a virtual copy of the initial curves, shifted by ≈ 460 μm . This result confirms that the (corrected) measured signals x^c are indeed mainly generated by the test mirror surface topography. Minor differences in the observed signals might be attributed to the circular movement of the test mirror and the slightly shifted measurement line caused by the offset. After removing the window from the setup, the initial measurement condition is recovered and the measurements are continued leading to curves, which are identical to the ones obtained a few days earlier in the initial measurement, see Figure 2.19.

As described above, a reduction of the laser beam size on the test mirror will lead to an increased lateral resolution of the measurement results, since the surface topography is averaged over a smaller beam cross-section. This relation is demonstrated by placing an aspheric lens with a focal length of $l_f = 12$ mm into the measurement beam (Figure 2.17, configuration **C**),

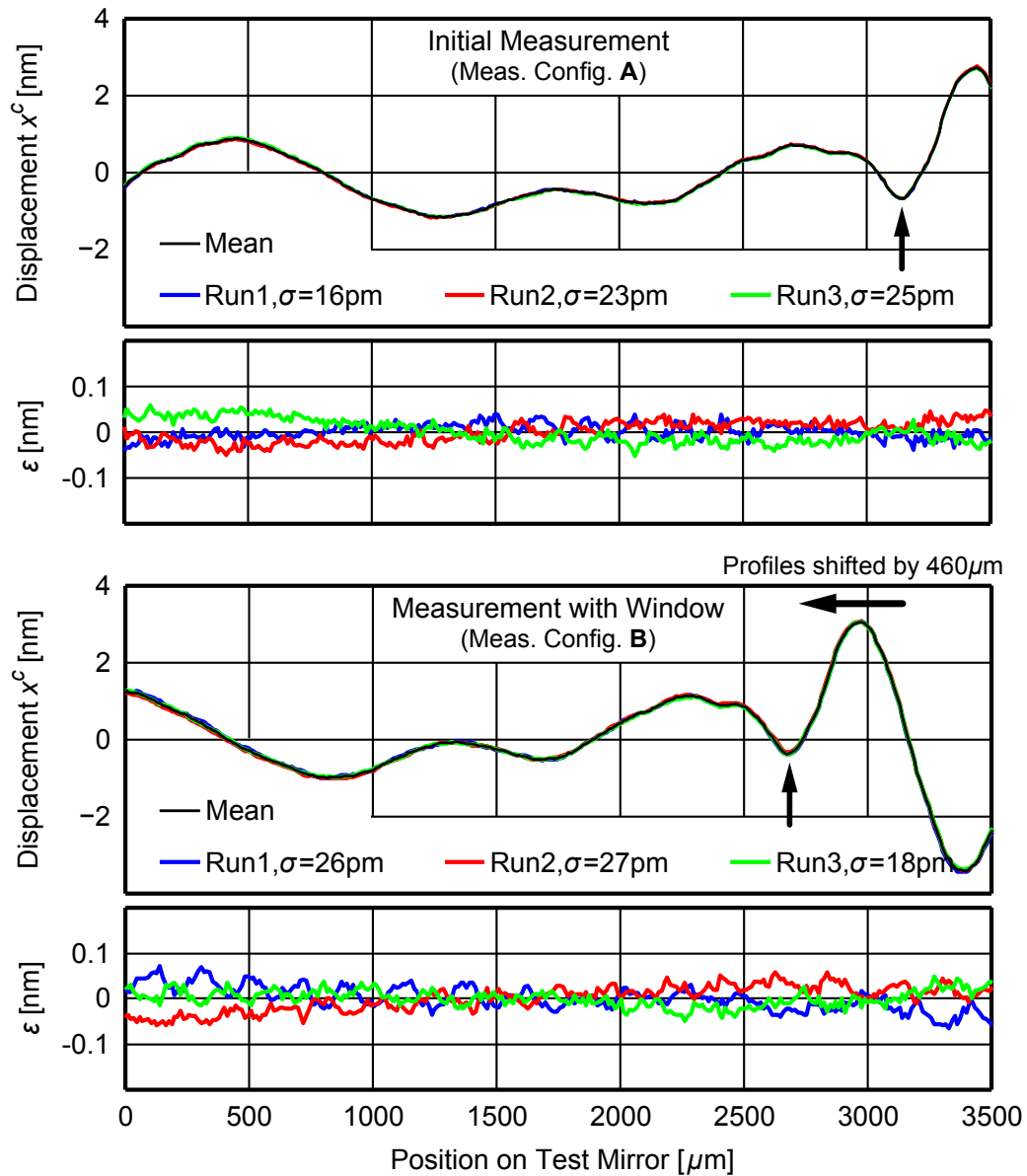


Figure 2.18: The initial measurement (top, measurement configuration **A**) shows highly reproducible (surface topography induced) signals over several measurement runs with amplitudes at the low nm level. The reproducibility is quantified by the standard deviation σ (stated in the legend), which is based on the deviation ϵ of each run with respect to the average signal. The subsequent measurement (bottom, measurement configuration **B**) includes a plane-parallel window, which is placed (at a small angle) in the measurement and reference laser beam for introducing a lateral beam offset on the test mirror surface. Since the offset is observed in the results, it can be concluded that the measured signals are indeed mainly generated by the surface topography. Both measurements show similar levels in standard deviation σ of the individual runs.

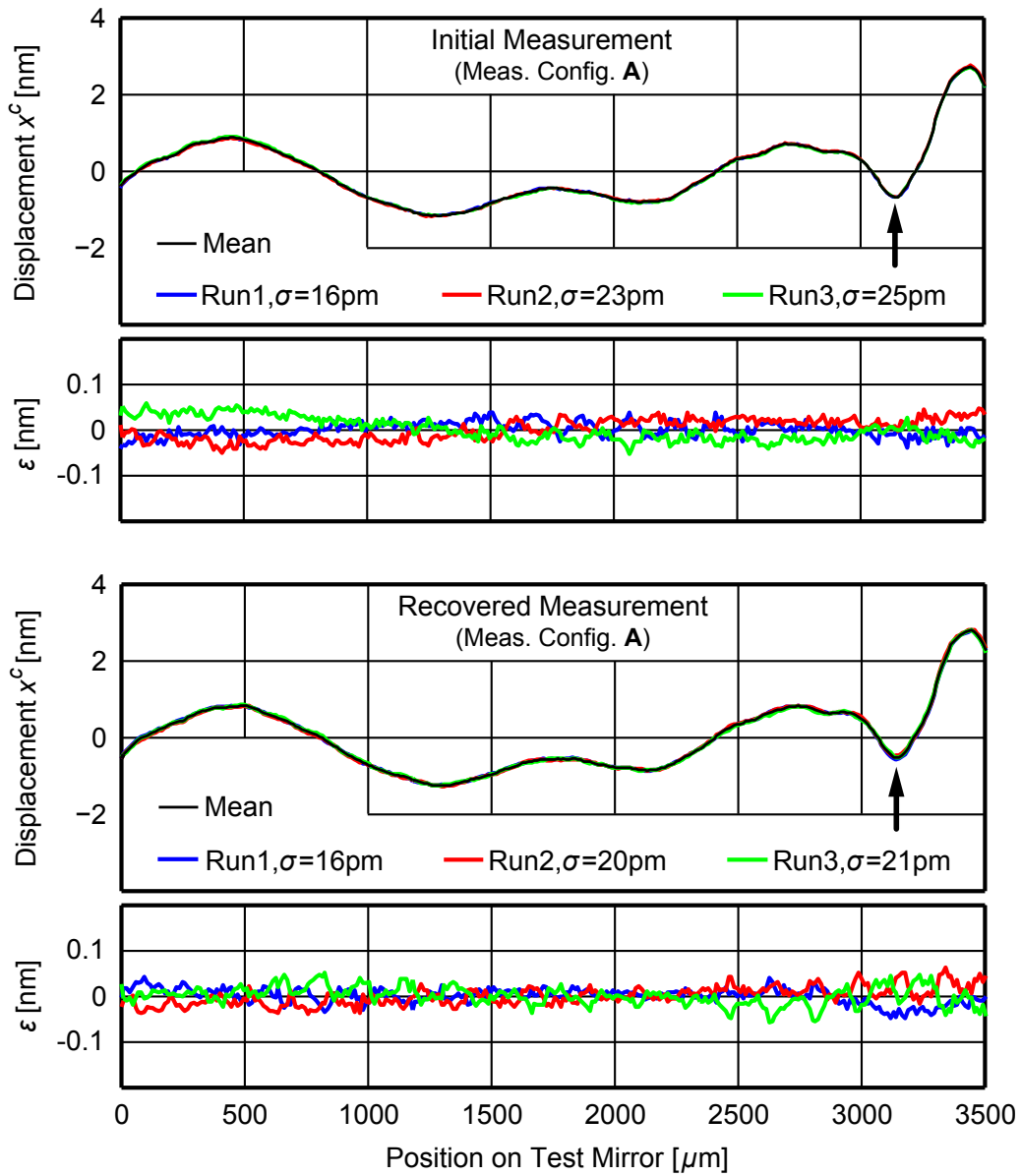


Figure 2.19: After removing the window from the measurement setup, the initial condition is recovered. Hence the measured curves (bottom) should be identical to the ones obtained in the initial measurement (top), which is confirmed to be true. Both measurements show similar levels in standard deviation σ of the individual runs.

hence reducing its diameter to a calculated value of $d_m \approx 13 \mu\text{m}$ in the beam waist. This is ≈ 100 times smaller than the beam size utilised in the previous measurements. The longitudinal position of the lens along the direction of beam propagation is set to put the beam waist onto the test mirror surface. This considerable change in beam size requires an adaption of the applied step size of the pendulum mechanism in order to guarantee adequate surface overlap between the steps. The new step size was chosen to be $2 \mu\text{m}$, since smaller values showed no further improvements in measurement accuracy. Additional changes to the data analysis are applied, since the DWS signal of the measurement beam is now influenced by the local curvature of the surface topography. In consequence, the correction for test mirror tilt is now conducted only by the DWS signal of the reference laser beam α_r , which is kept at the initial size ($d_r = 1.3 \text{mm}$).

The measured (corrected) signals of this new configuration are displayed in Figure 2.20 and show a highly improved lateral resolution as well as slightly higher displacement values, as expected. Both effects can be explained by the smaller cross-section, hence reduced averaging of the surface topography. However, the standard deviation σ shows increased values in the order of $50 \text{pm} - 100 \text{pm}$ for the different runs, attributed to the extended measurement bandwidth to higher spatial frequencies as well as the longer measurement duration. Additional systematic contributions are expected due to the modified correction for parasitic test mirror tilts based solely on the DWS signal of the reference mirror mentioned above. In principle these results reflect the test mirror surface topography ρ_{TM} , at least when only considering the spatial frequency range, which is attenuated in the reference signal due to the averaging over the large cross-section of the reference beam.

Result Comparison & Modelling A validation and comparison of the measurement results is conducted using comprehensive surface measurements of a similar mirror - of the same manufacturing batch - as the test mirror employed. These measurements were performed by the PTB, using interference microscopy with phase shifting at a wavelength of 549.9nm . Figure 2.21 (top) shows the raw data, recorded over an area of $416 \mu\text{m} \times 312 \mu\text{m}$ at a sampling interval of $0.65 \mu\text{m}$. In order to generate comparable results, the low-pass-filter effect of a Gaussian laser beam with a diameter of $d_b = 13 \mu\text{m}$, has to be applied to the data. A comparison of the results utilising the larger beam diameter $d_b = 1.3 \text{mm}$ is not performed, due to the small measured area of the microscopic measurements. The filter function g_G for a laser beam with Gaussian intensity distribution is given by

$$g_G(y, z, y_0, z_0, d_b) = \frac{8}{\pi d_b^2} \cdot e^{-8 \left(\frac{(y-y_0)^2 + (z-z_0)^2}{d_b^2} \right)} \quad (2.25)$$

with d_b representing the $1/e^2$ diameter of the laser beam on the mirror surface and the factor $8/(\pi d_b^2)$ is used for normalisation. In the next step, this filter function is applied on the PTB surface data ρ_{PTB} , which corresponds mathematically to a two-dimensional convolution described by

$$\rho_{\text{PTB}}^c(y_0, z_0, d_b) = \rho_{\text{PTB}}(y, z) * g_G(y, z, y_0, z_0, d_b). \quad (2.26)$$

Figure 2.21 (bottom) shows the results after applying the filter function for a Gaussian laser beam of diameter $d_b = 13 \mu\text{m}$, which leads to a reduced lateral resolution compared to the raw data. This result is consistent with the findings of the interferometric measurements, and thus can be compared since both of them are similarly filtered.

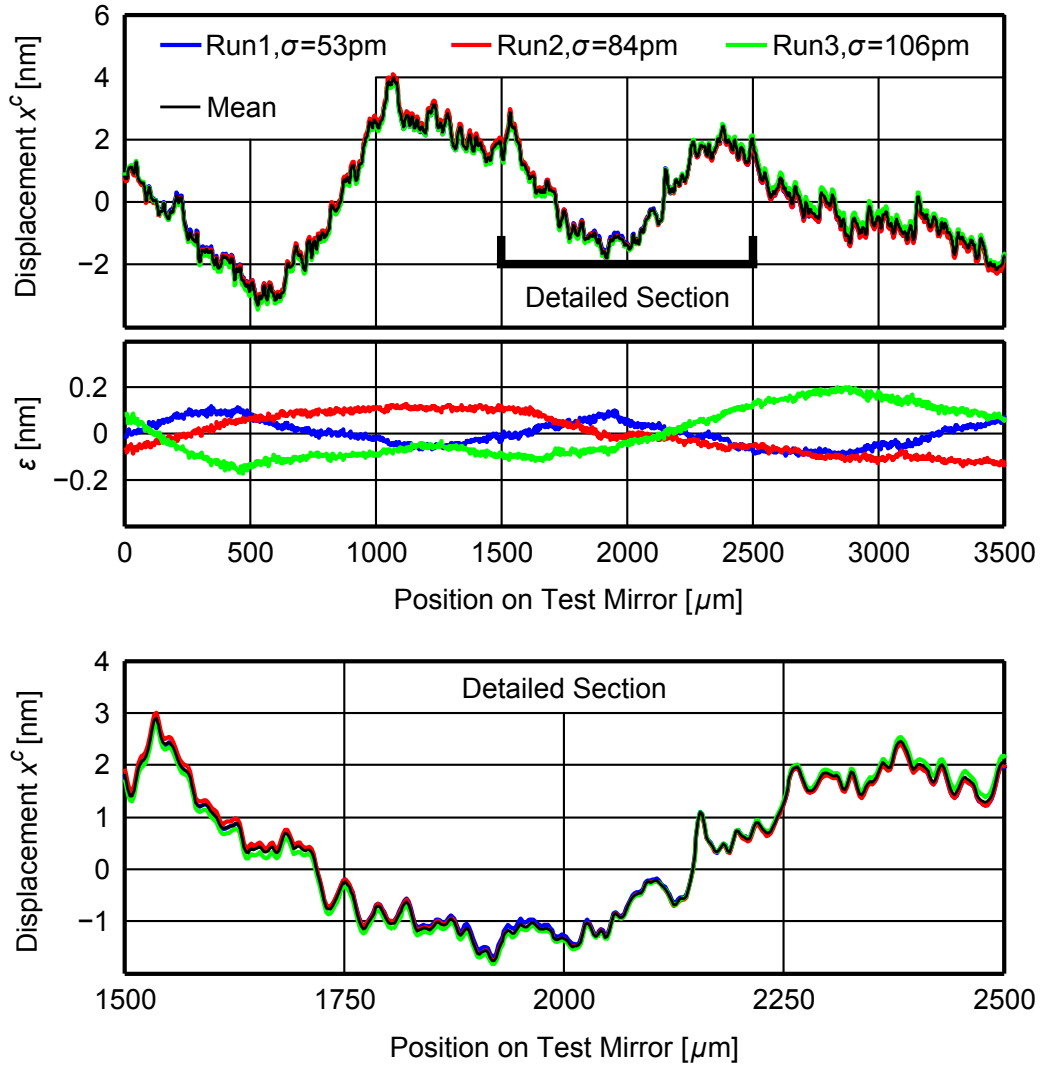


Figure 2.20: The results of measurement configuration **C** with focused measurement beam ($d_m \approx 13 \mu\text{m}$) shows signals with an improved lateral resolution as well as higher topography amplitudes compared to the initial measurement. Both effects can be explained by the smaller cross-section of the measurement beam, hence reduced surface averaging. However, the standard deviation σ of the individual run has slightly increased.

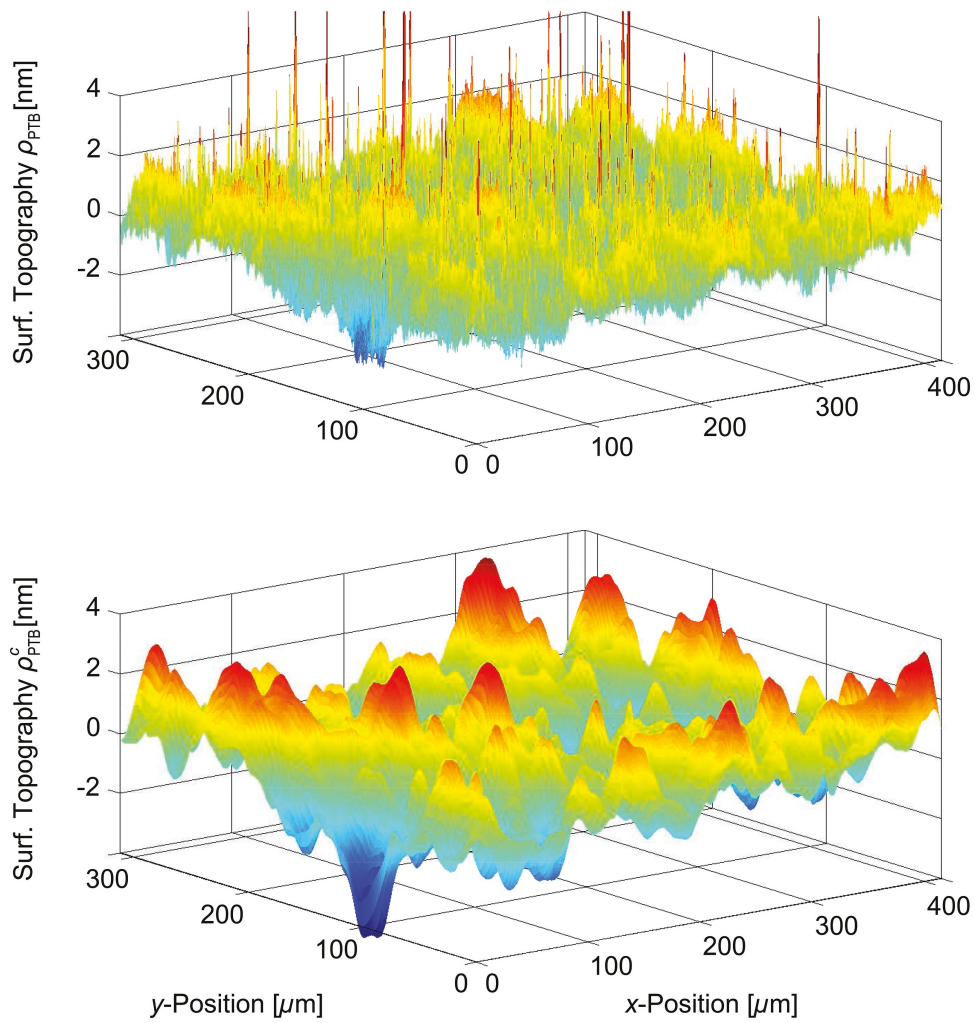


Figure 2.21: Measured surface topography ρ_{PTB} of a similar laser mirror as the test mirror employed (top). The measurements were performed by the PTB using interference microscopy with phase shifting. After low-pass filtering of the data with a simulated (Gaussian) laser beam of diameter $d_b = 13 \mu\text{m}$, the results show some similarity to the results of the interferometric measurements (bottom).

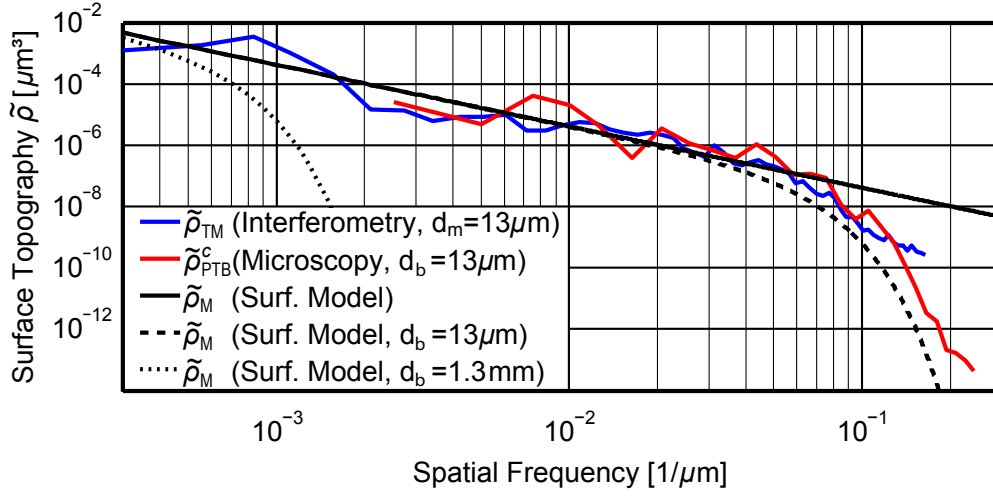


Figure 2.22: Surface spectrum ($\tilde{\rho}_{TM}$) of the interferometric measurements with focused measurement beam ($d_m = 13 \mu\text{m}$) and the accordingly filtered microscopic measurements ($\tilde{\rho}_{PTB}^c$) performed by the PTB. They show full agreement with a similar drop at spatial frequencies above $\approx 5 \cdot 10^{-2} \mu\text{m}^{-1}$, caused by the actual / simulated low-pass filter effect of a Gaussian laser beam. The theoretical surface spectrum ($\tilde{\rho}_M$) shows a similar behaviour, after accounting for a Gaussian laser beam of the same diameter. A filtering of the theoretical surface spectrum with a simulated laser beam of diameter $d_b = 1.3 \text{ mm}$ validates, that the surface spectrum extracted from the interferometric measurements is indeed representing the surface topography, since surface induced displacements in the reference laser beam are sufficiently suppressed at spatial frequencies above $\approx 10^{-3} \mu\text{m}^{-1}$.

A full comparison of the results is conducted using the spectrum of the surface topography. Hereby the results with focused measurement beam ($d_m = 13 \mu\text{m}$) as well as the correspondingly filtered PTB data are compared with respect to each other. The surface PSDs are calculated based on the average signal (interferometric measurements), or on one line of the low-pass filtered PTB surface data (microscopic measurements), respectively. Both surface PSDs show full agreement, see Figure 2.22, with a similar drop at spatial frequencies above $\approx 5 \cdot 10^{-2} \mu\text{m}^{-1}$ due to the low-pass filter effect of the laser beam.

Further on, a theoretical model of the surface topography is derived. The spectrum of this model can be described by

$$\tilde{\rho}_M = C_a \left(\frac{\nu}{\nu_0} \right)^{-a} \quad (2.27)$$

(given by DIN ISO 10110 – 8). Herein C_a is a constant factor, which describes the level of the topography amplitudes, ν represents the spatial frequency and the constant $\nu_0 = 1 \mu\text{m}^{-1}$ is used for normalisation. The exponent $a \in \{1, 2, 3\}$ describes the distribution of the topography amplitudes over the spatial spectrum.

Based on the measurement data, the values of the different variables are determined to be $C_a = 4.1 \cdot 10^{-10} \mu\text{m}^3$ and $a = 2$. In order to account for the low pass filter effect of averaging surface irregularities over the laser beam cross-section, the convolution theorem of Equation 2.26 is applied, resulting in a multiplication of the mirror surface spectrum $\tilde{\rho}_M$ with

the spectrum of a Gaussian laser beam \tilde{g}_G in the spatial frequency domain, described by

$$\tilde{\rho}_M \approx C_a \left(\frac{\nu}{\nu_0} \right)^{-a} \cdot \tilde{g}_G(\nu) \quad (2.28)$$

with the filter function for a Gaussian laser beam

$$\tilde{g}_G(\nu) = e^{-\left(\frac{\pi}{2} d_b \nu\right)^2} [47]. \quad (2.29)$$

The results of this model, filtered assuming laser beam diameters of $d_b = 13 \mu\text{m}$ and $d_b = 1.3 \text{mm}$, as present in the experimental measurements, are also displayed in Figure 2.22. Especially the curve for $d_b = 13 \mu\text{m}$ shows excellent agreement with the experimental data, whereas the curve for $d_b = 1.3 \text{mm}$ is only used to check, in which spatial frequency range displacement contributions of the reference beam can be expected. One can see that spatial frequencies above $\approx 10^{-3} \mu\text{m}^{-1}$ are sufficiently suppressed, which implies that the results do indeed represent the test mirror surface topography ρ_{TM} , hence $\tilde{\rho}_{\text{TM}}$.

2.2 The LISA IFP Telescope Design

The IFP wide-field telescopes onboard the LISA spacecraft are used to transmit and receive the laser light for interferometry to and from the remote spacecraft. Some of the telescope's requirements are listed below:

- Provide an accessible intermediate pupil plane for the IFPM, which implements an in-plane beam pointing for changing the line of sight of the telescope in order to account for (angular) changes in the LISA spacecraft formation.
- Provide an accessible exit pupil plane for the point ahead angle mechanism (PAAM), which implements an out-of-plane beam steering for generating an angular offset between transmit and receive laser beam, in order to account for the travelling time of the laser light between the local and remote spacecraft.
- Provide a high level optical performance over the complete field of view, in particular concerning the far field quality of the transmitted beam as well as the achievable heterodyne efficiency for reception of a plane wave in order to enable the required measurement accuracy. This attribute also demands to minimise potential sources of measurement noise associated with dynamic changes in optical path length and stray light.

Considering these attributes, a conceptual design of the IFP wide-field telescope has been developed within a LISA mission formulation study [48] resulting in a specialised off-axis Schiefspiegler telescope with the off-axis plane orthogonal to the pointing plane and an external pupil of $\varnothing 400 \text{mm}$. This telescope consists of 6 mirrors with power (M1 - M6), three flat folding mirrors (F1 - F3) and one flat scan mirror (S1). They are divided in two stages with a magnification of 10 in each stage, see Figure 2.23.

Stage one (M1, M2, F1, M3, F2 and S1) is an off-axis mirror system representing a Korsch telescope including the IFPM for beam pointing (with S1). Hereby the IFPM will cover the required field of view, which is calculated to be $\pm 0.5^\circ$ based on the orbital data. The afocal optical system of the presented telescope is fully reflective (10 reflections in total), which helps

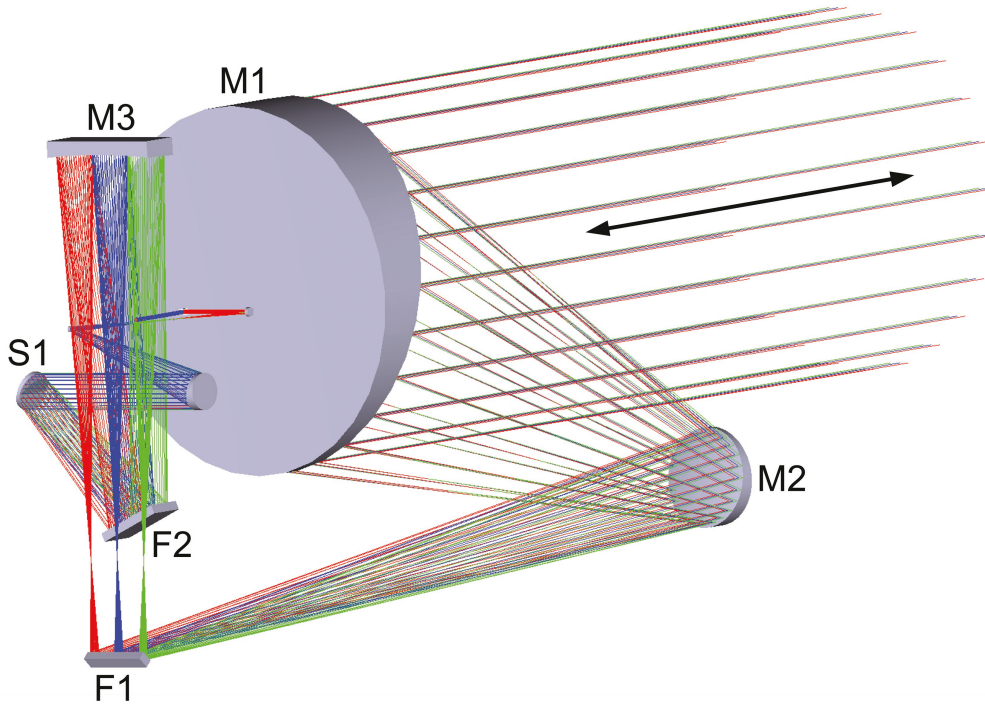


Figure 2.23: Schematic of the off-axis Schiefspiegler telescope with IFP. Marked are the mirrors of stage one (M: Mirrors with Power; F: Flat Folding Mirrors; S: Flat Scan Mirror;). The mirror S1 is actuated by the IFPM in order to enable beam pointing. Three different positions of S1 are illustrated with different colours of the optical paths, blue for 0° , red for $+2.5^\circ$ and green for -2.5° .

Mirror	F1	M3	F2
Assumed Surface-Figure	$\lambda/10$	$\lambda/10$	$\lambda/10$
Beam Diameter on Mirror Surface d_t	10 mm	40 mm	40 mm
Beamwalk Distance l_p	57 mm	85 mm	31 mm
Beamwalk Velocity v_p	14.9 nm/s	22.2 nm/s	8.1 nm/s
Surf. Gradient Coupl. Factor $C_{u,G}$ (Gauss)	$9.56 \cdot 10^{-7}$	$4.78 \cdot 10^{-7}$	$4.78 \cdot 10^{-7}$
Surf. Gradient Coupl. Factor $C_{u,F}$ (Flat-Top)	$9.35 \cdot 10^{-7}$	$4.67 \cdot 10^{-7}$	$4.67 \cdot 10^{-7}$

Table 2.1: Data for the piston estimation in the IFP wide-field telescope due to beam pointing and associated beamwalk over mirror surfaces.

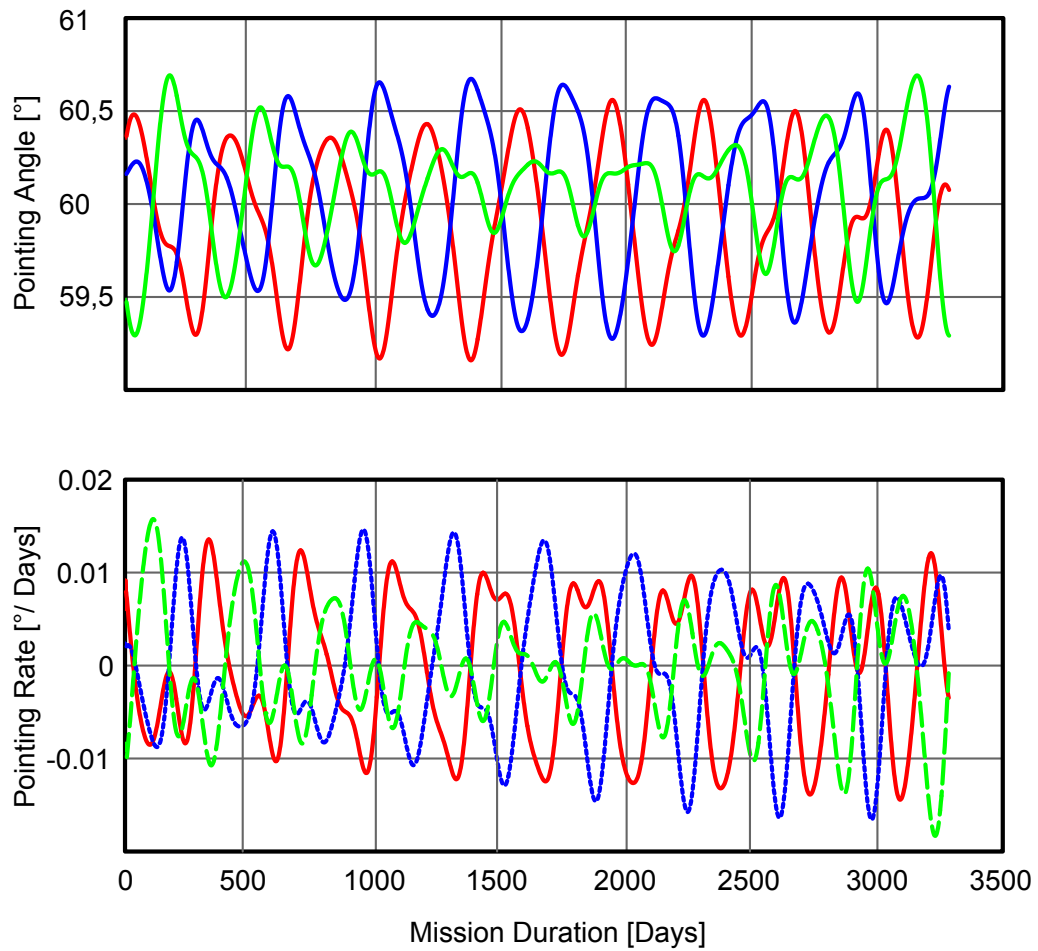


Figure 2.24: Expected pointing angle (top) and angular pointing rate (bottom) of the in-plane inter-arm angle of the LISA spacecraft formation, plotted over the mission duration. Variations are generated by constellation breathing. The three LISA spacecraft are distinguished by different colours of the curves.

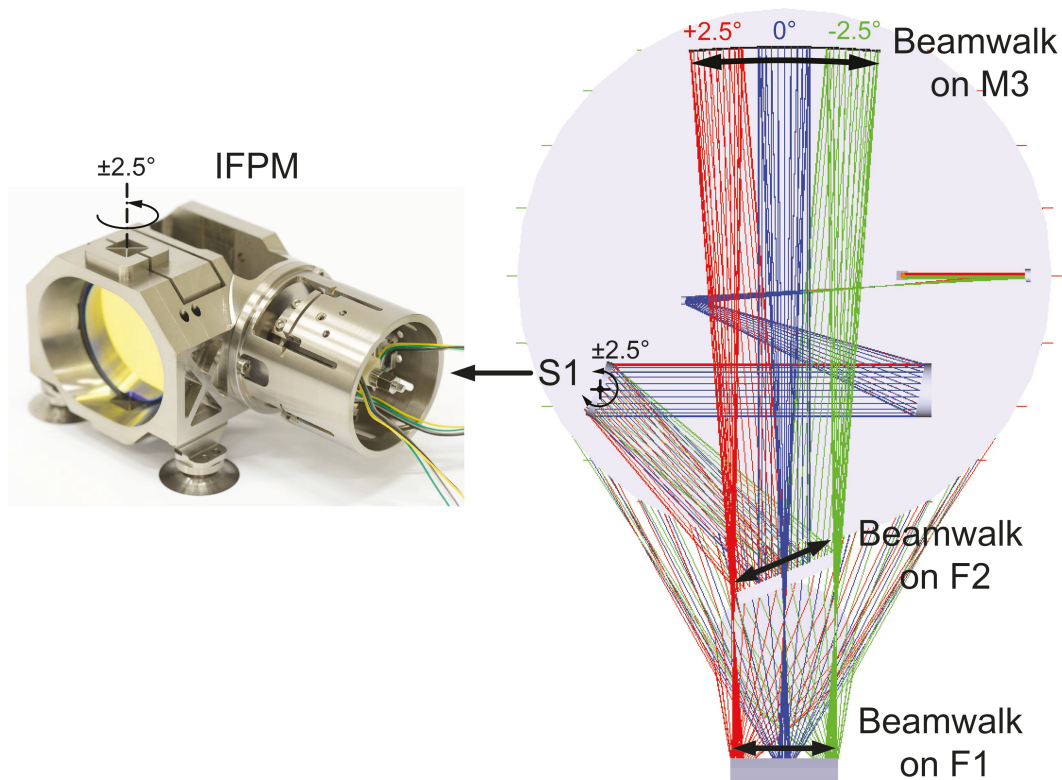


Figure 2.25: Photograph of the IFPM for beam pointing, positioned within the LISA IFP wide-field telescope (left) [Courtesy of TNO]. Schematic of the beamwalk on the telescope mirrors F2, M3 and F1 (right). The small beamwalk on M1 and M2 is considered negligible. Three different positions of S1 are illustrated with different colours of the optical paths.

reduce optical path length changes due to bulk material inhomogeneities or thermally driven changes in refractive index of the optics.

In the telescope design presented, beamwalk due to IFPM beam pointing is mainly present on the three mirrors F2, M3 and F1. The beamwalk on M1 and M2 is considerably smaller, thus has been neglected in the scope of this investigation. For further estimation of associated surface induced piston, it is required to determine the beamwalk distance l_p , beamwalk velocity v_p and the laser beam diameter d_t on each of these mirrors, based on the telescope's geometry and the orbital data of the LISA spacecraft formation, depicted in Figure 2.24. The orbital data show an expected maximum value in inter-arm angle of $\approx \pm 0.8^\circ$ per spacecraft resulting in an individual inter-arm angle of $\approx \pm 0.4^\circ$ for a single telescope. Based on these values the beamwalk distance l_p is calculated for an actuation of the scanning mirror S1 of $\pm 2^\circ$, which accounts for the magnification factor of 10 in stage one of the telescope. The occurring beamwalk is also schematically shown in Figure 2.25.

As a simplification for calculating the beamwalk velocity v_p , the pointing rate is assumed to be constant at $3.65 \cdot 10^{-6}$ mrad/s or $1.825 \cdot 10^{-6}$ mrad/s per telescope, extracted from the orbital data. This represents a worst-case scenario, since this value is the highest pointing rate to be expected during LISA lifetime. Table 2.1 summarises the results, which are used for the piston estimation within the IFP wide-field telescope generated by beam pointing and the associated beamwalk.

2.2.1 Estimation of Piston Generated by Beamwalk

The surface topography spectra obtained from the experimental data, which are displayed in Figure 2.22, multiplied by a factor of 2 (for considering path length changes in the incident and reflected beam) represent the piston of a Gaussian laser beam of diameter $d_b = 13 \mu\text{m}$ scanning over a $\lambda/10$ or $3/0.2$ mirror surface. The results show typical piston in the order of a few nm depending on the laser beam diameter utilised. At this point, it is not self-evident that this scale of piston complies with the required pm sensitivity of the LISA metrology instrument for the detection of gravitational waves. Thus, the piston within the IFP wide-field telescope generated by beam pointing and the associated beamwalk over the mirror surfaces of F2, M3 and F1 have been estimated based on the theoretical surface model introduced previously. The results have been checked against the allocated requirement for IFPM piston \tilde{q}_p given by

$$\tilde{q}_p(f) \approx 2 \cdot 10^{-12} \frac{\text{m}}{\sqrt{\text{Hz}}} \cdot \sqrt{1 + \left(\frac{2.8 \text{ mHz}}{f}\right)^4}, \quad (2.30)$$

where f represents the time frequency, which is given by the LISA measurement bandwidth ($3 \cdot 10^{-5} \text{ Hz} - 1 \text{ Hz}$) [49]. Since this value covers all noise sources related to the IFPM, including geometrical coupling of tilt to piston and thermo-elastic effects coupling to piston, the resulting estimated values should be well below this limit. The estimation is both performed for piston due to deterministic pointing p_p , which systematically compensates for variations in the inter-arm angle of the spacecraft formation as well as for piston due to pointing-jitter p_j , caused by random mechanical jitter of the IFPM.

2.2.1.1 Piston due to Deterministic Pointing

In the context of IFP, the laser beam diameters d_t and beamwalk distances l_p are considerably larger than those applied in the previously presented experimental investigations for surface characterisation of the test mirror. The theoretical surface model therefore is scaled to these new conditions, see Figure 2.26, in order to estimate the surface topography spectrum $\tilde{\rho}_M$ for a Gaussian (transmitted) as well as a flat-top (received) laser beam of diameter $d_t = 10 \text{ mm}$ (mirror F1) and $d_t = 40 \text{ mm}$ (mirror M2 and M3). The filter function applied for a Gaussian beam has already been introduced in Equation 2.29 and the filter function for a flat-top beam can be written as

$$\tilde{g}_F(\nu) = \left(\frac{2J_1(\pi\nu d_t)}{\pi\nu d_t}\right)^2 \quad [47] \quad (2.31)$$

with J_1 representing the first kind Bessel function. These surface topography spectra are transferred from the spatial frequency domain ν into the frequency domain f for a comparison with the IFP piston requirement. To this end, the beamwalk velocity v_p is taken into account, using the conversion of the respective spatial frequencies to frequencies with $f = \nu \cdot v_p$ and

$$\tilde{\rho}_M(f) = \frac{\tilde{\rho}_M(\nu)}{v_p}. \quad (2.32)$$

By multiplying the resulting spectra with a factor of 2 they yield to the expected piston due to deterministic pointing \tilde{p}_p and the associated beamwalk, displayed in Figure 2.27 including the IFP piston requirement \tilde{q}_p . One can see that the piston caused by a Gaussian beam appears well outside the LISA measurement bandwidth and is therefore negligible, which is attributed

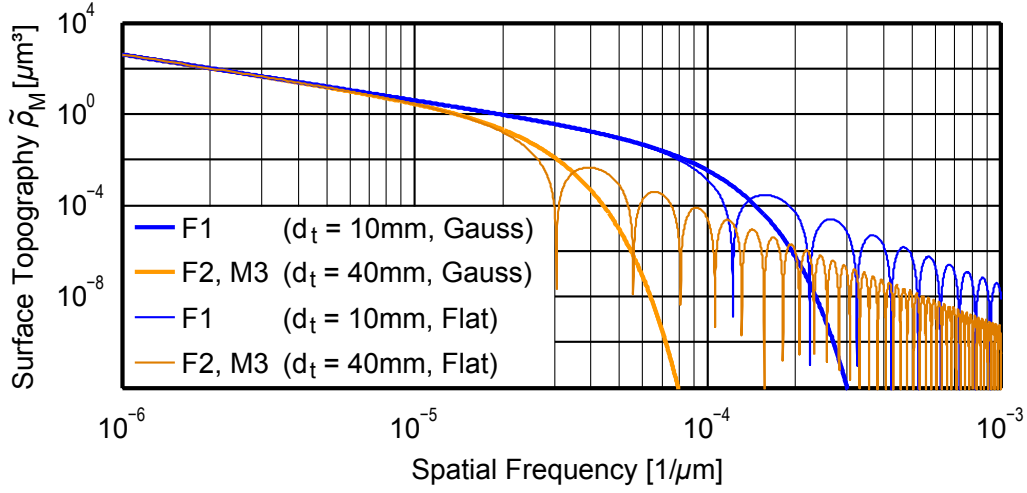


Figure 2.26: Estimated surface topography spectra of a Gaussian and a flat-top laser beam of diameter $d_t = 10$ mm and $d_t = 40$ mm as incident on the telescope mirrors F2, M3 and F1.

to the low beamwalk velocities v_p as well as the extensive averaging due to the large beam sizes on the telescope mirrors. The piston caused by a flat-top beam, however, shows some contributions within the LISA measurement bandwidth, but they are ≈ 2 orders of magnitudes below the requirement. This effect is in particular caused by the assumed shape of the flat-top beam, including an edge all around, which does not suppress high frequency content of the surface topography at higher spatial frequencies as effective as a Gaussian beam. Thus, they appear in the LISA measurement bandwidth after the conversion.

Altogether these results predict that piston due to deterministic pointing is negligible when considered by itself. Nonetheless its final impact has to be investigated in more detail together with the results of the estimation of the surface topography induced piston due to pointing-jitter p_j , in order to come to a final conclusion.

2.2.1.2 Piston due to Pointing-Jitter

The calculation of the piston spectrum due to pointing-jitter \tilde{p}_j is conducted by multiplying the spectrum of beamwalk \tilde{l}_j (caused by pointing-jitter) on the three telescope mirrors F2, M3 and F1 with a coupling factor $C_{u,G}$ or $C_{u,F}$, which represent the RMS value of the local gradient of the surface topography for a Gaussian as well as flat-top beam, respectively, leading to

$$\tilde{p}_j(f) \approx 2 \cdot 3 C_{u,G,F} \cdot \tilde{l}_j(f). \quad (2.33)$$

For a conservative assumption, the coupling factor is multiplied by a factor of 3, leading to the 3σ value, which accounts for $\approx 99.7\%$ of the piston gradients occurring. Since the amplitude of the pointing-jitter induced beamwalk is considerably smaller than the laser beam diameter and consequently also much smaller than the relevant spatial frequencies of the piston (meaning that the effect is only locally induced), this first order modelling / linearisation is justified.

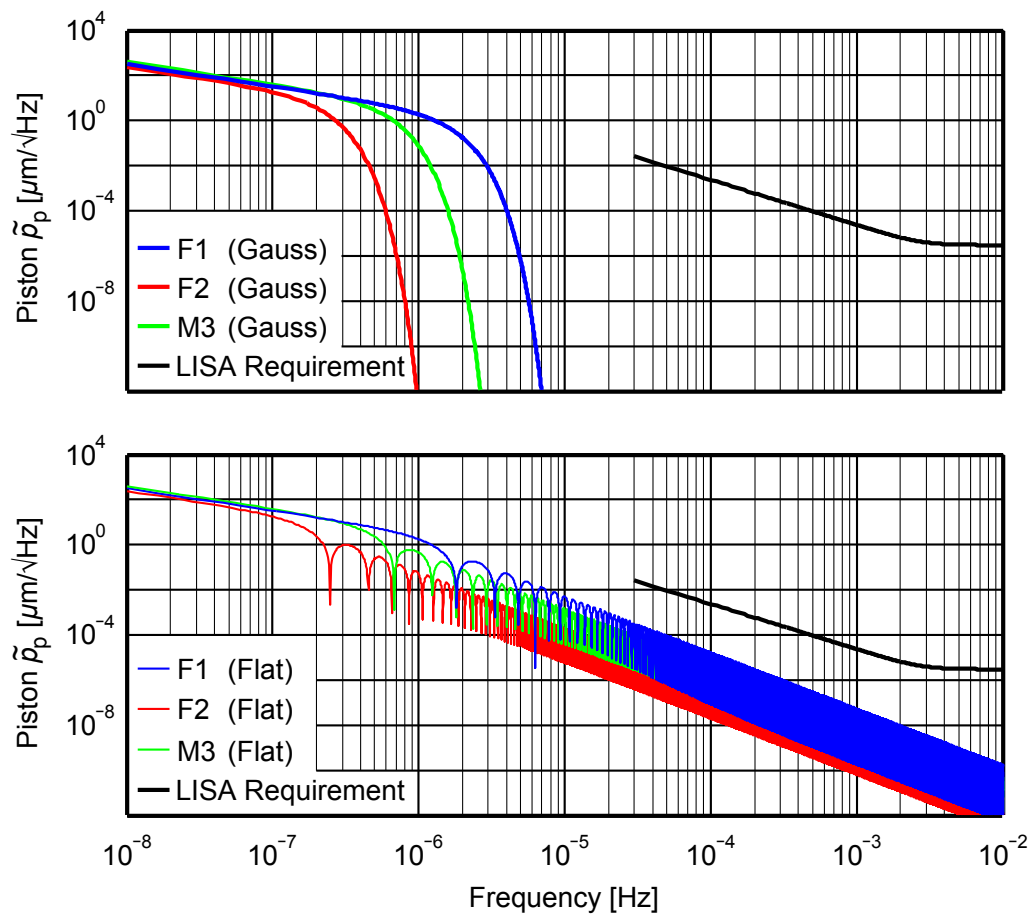


Figure 2.27: Estimated piston spectra \tilde{p}_p due to deterministic pointing, which systematically compensates for variations in inter-arm angle of the spacecraft formation. Displayed are the results for a Gaussian (top) and flat-top beam (bottom). All spectra meet the IFP piston requirement \tilde{q}_p (black curve) with considerable margin, however in quite different ways. The spectra simulating a Gaussian beam decline strongly at frequencies well below the LISA measurement bandwidth and show therefore no contribution. On the other hand, the spectra simulating a flat-top beam indeed show contributions within the LISA measurement bandwidth, however, they are well below the requirement.

The spectrum of beamwalk due to pointing-jitter \tilde{l}_j is calculated by transforming the power spectral density (PSD) of the angular pointing-jitter requirement \tilde{q}_j , given by

$$\tilde{q}_j(f) = 10 \cdot 10^{-9} \frac{\text{rad}}{\sqrt{\text{Hz}}} \cdot \sqrt{1 + \left(\frac{2.8 \text{ mHz}}{\nu}\right)^4} \quad (2.34)$$

into a beamwalk on each mirror, displayed in Figure 2.28, by using the geometrical data of the telescope.

The coupling factor $C_{u,G,F}$ is defined as the rms value of the PSD of the piston gradient $\tilde{u}_{G,F}$, calculated by multiplying the corresponding spatial spectra of the piston \tilde{p} with the square spatial angular frequency given by

$$C_{u,G,F} = \text{rms} [\tilde{u}_{G,F}(\nu)] = \sqrt{\int_0^{\infty} \tilde{u}_{G,F}(\nu) d\nu} \quad (2.35)$$

with

$$\tilde{u}_{G,F}(\nu) = \tilde{\rho}_M(\nu) \cdot (2\pi\nu)^2. \quad (2.36)$$

The spectra of the piston gradient $\tilde{u}_{G,F}$ for the relevant telescope mirrors, including the parameters for laser beam type and diameter are shown in Figure 2.29, whereas the calculated coupling factors $C_{u,G,F}$ are indicated in Table 2.1. Based on these results the piston due to pointing-jitter \tilde{p}_j is calculated, depicted in Figure 2.30. All curves meet the IFP pointing requirement \tilde{q}_p with considerable margin. The low piston amplitudes can be explained by the small jitter-beamwalk amplitudes and the large laser beam diameters on the telescope mirrors, which lead to substantial averaging effects of the surface topography and thus small piston gradients. Additionally, one can see that the spectra of a Gaussian and a flat-top laser beam are rather similar, which is attributed to the small difference in the coupling factors $C_{u,G}$ versus $C_{u,F}$.

Finally, in order to consider a worst-case scenario, the piston spectra due to deterministic pointing \tilde{p}_p and the piston spectra due to pointing-jitter \tilde{p}_j of the telescope mirrors F2, M3 and F1 are summed up, which is equivalent to the assumption of fully correlated piston contributions, leading to the maximum expected piston due to surface irregularities (for a specific type of laser beam). The results are displayed in Figure 2.31 and show piston levels, which are consistently $\approx 1.5 - 2$ magnitudes below the requirement. These results leads to the conclusion that the piston due to deterministic pointing and pointing-jitter can be neglected indeed, for the presented IFP wide-field telescope design. However, changes in the telescope's geometrical or optical design can possibly introduce increased piston levels, which then have to be investigated in more detail again.

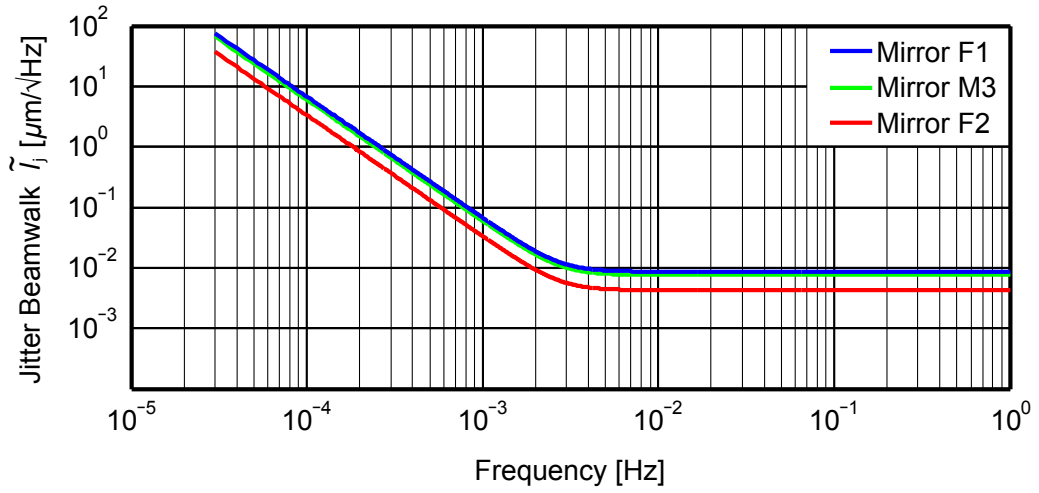


Figure 2.28: Spectra of the beamwalk due to IFPM pointing-jitter \tilde{l}_j on the three telescope mirrors F2, M3 and F1. The spectra are calculated based on the telescope's geometry.

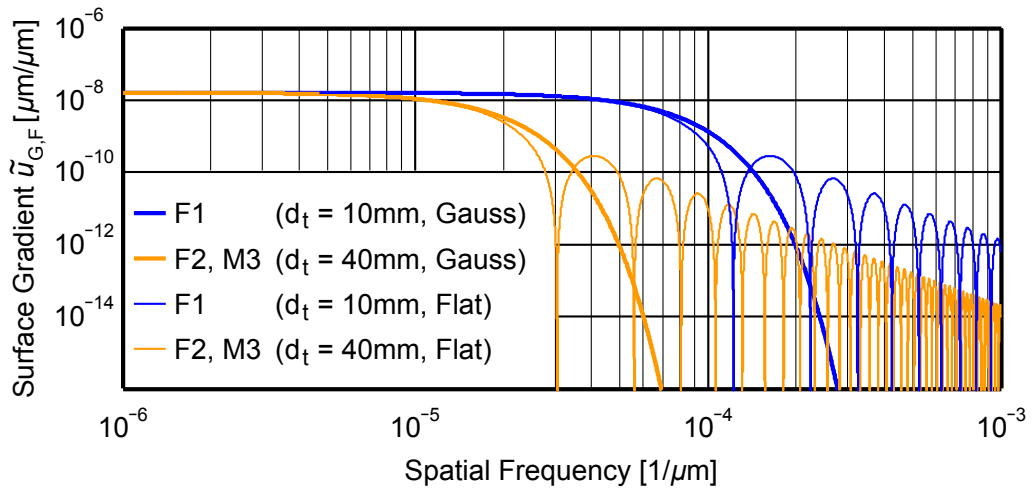


Figure 2.29: Spectra of the piston gradient \tilde{u} for the three telescope mirrors F2, M3 and F1 considering both, Gaussian as well as flat-top beams.

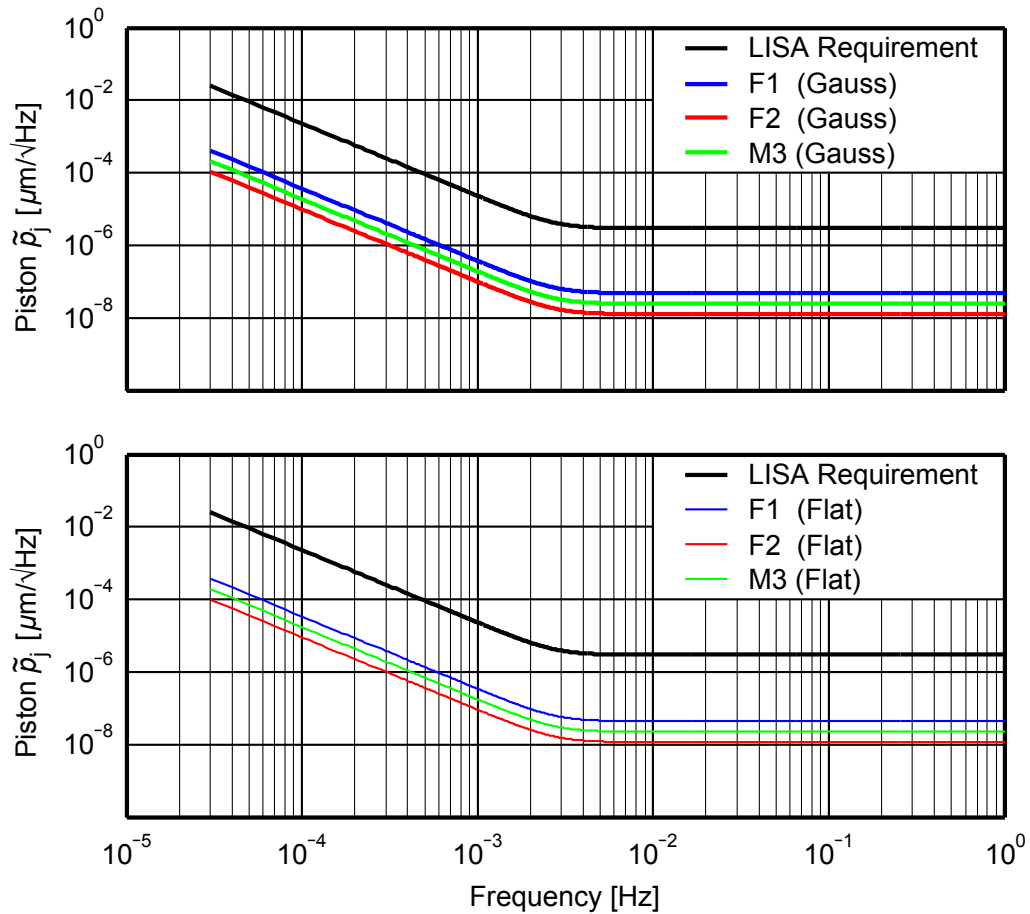


Figure 2.30: Estimated piston spectra due to pointing-jitter \tilde{p}_j , which is caused by random mechanical jitter of the IFPM / the actuated mirror S1. Displayed are the results for a Gaussian (top) and flat-top beam (bottom). All spectra meet the IFP pointing requirement \tilde{q}_p (black curve) with considerable margin.

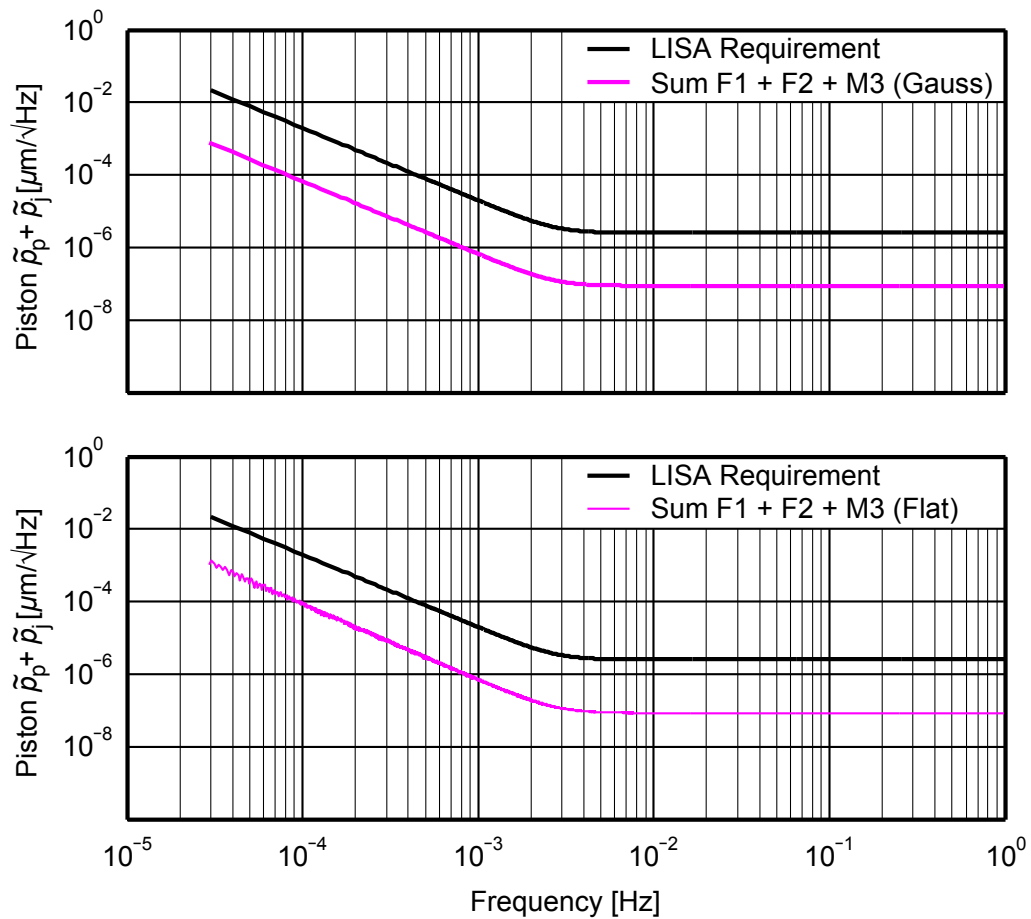


Figure 2.31: Estimated spectra of the maximum expected piston in the IFP wide-field telescopes caused by surface irregularities for Gaussian (top) and flat-top beams (bottom). Displayed is the sum of the piston spectra due to deterministic pointing \tilde{p}_p and pointing-jitter \tilde{p}_j of the three telescope mirrors F2, M3 and F1, representing a worst-case scenario by assuming fully correlated piston contributions. The curves show piston levels, which are consistently $\approx 1.5 - 2$ magnitudes below the requirement. This result leads to the conclusion, that the surface induced piston within the IFP wide-field telescope can be neglected, at least for the considered telescope design.

3 An Inertial Sensor Concept featuring a SPM

Within the alternative LISA IFP payload concept, presented in Chapter 1 of this thesis, the use of a single active GRS including a SPM is considered. This concept enables a fully drag-free operation of the proof mass in the absence of any suspension forces in all DoFs, at least during science measurements. Additionally, SPMs in combination with an all optical read-out can be implemented with a large gap size between the proof mass and the surrounding housing, which further reduces residual forces generated by charges of the proof mass. Both of these effects promise a potential reduction in residual acceleration noise of the proof mass, hence an improved measurement performance.

A conceptual design of a LISA GRS with SPM has already been investigated including several variations in configuration [37]. One major limitation identified are errors in position determination of the SPM centre of mass (CoM), due to its surface topography and related optical path length changes under rotation, which will be misinterpreted as changes in CoM position by the optical read-out. It is expected, that even with modern technologies the surface of a SPM can only be manufactured to a precision in the order of a few tens of a μm (peak to valley amplitudes of the topography). Since this value is $\approx 10^3$ times higher than the allocated LISA requirement for displacement noise (see Equation 1.1), the SPM topography will represent a dominant source of error, which has to be considered.

At the moment, two complementary solutions are discussed and investigated to address this issue:

- The application of a defined spin (≥ 10 Hz) onto the SPM in order to average its surface, thus (spectrally) shifting topography induced errors as well as mass centre offset errors due to inhomogeneities in density outside the LISA measurement bandwidth between $3 \cdot 10^{-5}$ Hz - 1 Hz.
- The implementation of a correction algorithm, which utilises a detailed SPM surface map, measured on ground prior to launch of the satellites, for a subsequent correction of the topography induced errors in the recorded in-orbit measurement data.

This chapter describes the development of an optical measurement setup, which features two heterodyne interferometers for optical surface topography measurements of a sphere, in order to address the latter solution in more detail and to investigate its feasibility. It also contains first results of one-dimensional interferometric topography measurements of a proof mass dummy, representing a first step to a complete surface map [50].

The second part of this chapter covers the development of a levitation system for spheres, which enables additional detailed investigations in this novel inertial sensor concept, including the read-out configuration, the different concepts (mentioned above) for compensating topography induced errors in the SPM CoM position determination as well as contact-free SPM discharge systems. The levitation system presented here features an electro-magnet for levitating a magnetic proof mass dummy in combination with an optical read-out for height control.

Parameter	Value
Quality Class	G20
Nom. Diameter d_{SPM}	40 mm
Max. Deviation of d_{SPM}	$\pm 11.5 \mu\text{m}$
Max. Fluctuation of d_{SPM}	$\pm 0.5 \mu\text{m}$
Surface Roughness	$0.032 \mu\text{m}$

Table 3.1: Specification of the SPM dummy employed, which has been manufactured according to DIN5401.

3.1 Surface Mapping of a Sphere

The topic of surface mapping has been explored using a commercially available sphere made of tungsten carbide with a nominal diameter of $d_{\text{SPM}} = 40$ mm, originally intended for use in large ball bearings. This SPM dummy (in the further course only referred to as SPM) has been manufactured according to DIN5401. Its specification is summarised in Table 3.1, showing only small manufacturing tolerances and a high surface quality, suitable for interferometric measurements without the need for additional surface finishing or coating. The measurements are performed along a great circle of the sphere as a proof of principle of the setup and a first step towards generating a complete surface map.

3.1.1 Measurement Setup

A schematic of the measurement setup is depicted in Figure 3.1. The measurement principle involved is based on (non-tactile) profilometry using heterodyne interferometry [40, 41]. To this end, the measurement beam of the interferometer is aligned onto the surface of the SPM, which is rotated by an automated rotation stage. Thus, the measurement beam scans over the SPM surface topography, which leads to changes in distance, measured by the interferometer. In order to compensate for error movements of the sphere's geometrical centre, introduced by misalignment and parasitic movements of the rotation stage, the setup features two interferometers arranged in an opposed configuration, which enables a direct compensation for these errors by summing up the displacement signals.

3.1.1.1 Heterodyne Interferometer & Electronics

The interferometers utilised are based on the optical design already presented in Chapter 2 of this thesis. Also adopted is the optical design of the heterodyne frequency generation, in duplicate for supplying two interferometers. Figure 3.2 shows a photograph of the heterodyne frequency generation setup employed. However, changes include the PI control loops for intensity stabilisation (ISL) and phase lock (PLL), which have been changed to a digital implementation, running on a FPGA board. Hereby, the PLL input signal is derived as the sum signal of one of the QPDs, which stabilises the complete length of the reference path and not only the path length in the optical fibres.

The interferometers' optical setup has also been subject to small changes and is depicted in Figure 3.3. It features Kösters prisms (KPs) instead of ESCs for generating the parallel beam pairs of different frequencies f_1 and f_2 . A major advantage of KPs in general is the increased

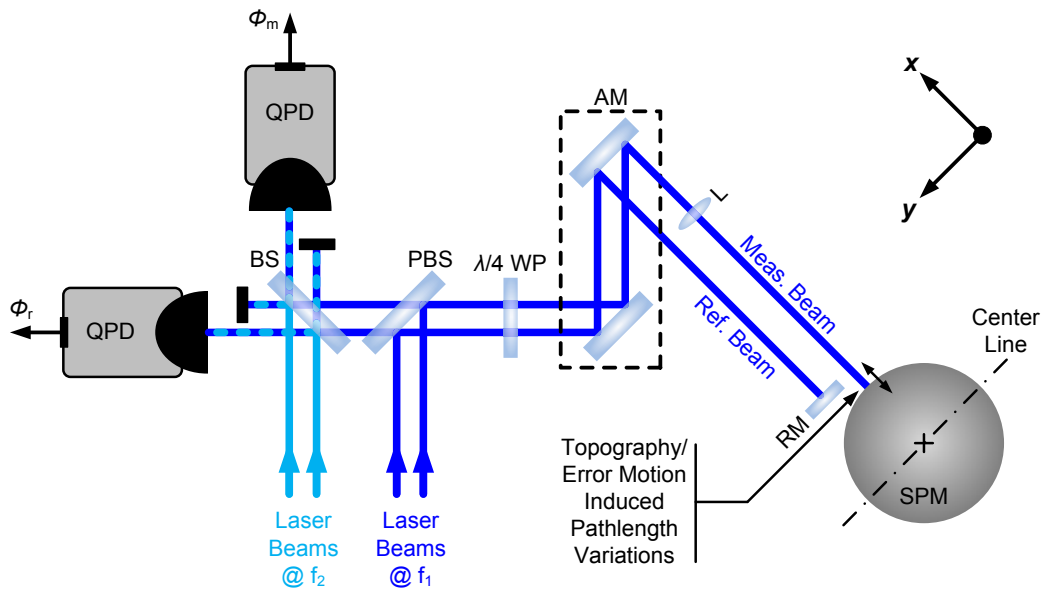


Figure 3.1: Simplified schematic of the measurement principle involved for the interferometric surface mapping of a sphere. Depicted is only one interferometer, the second one is positioned in an opposed configuration, mirrored at the centre line. BS: 50/50 Beam Splitter; PBS: Polarising Beam Splitter; WP: Wave Plate; AM: Set of (adjustable) Alignment Mirrors; L: Lens (for longitudinal mode match); RM: Reference Mirror; SPM: Spherical Proof Mass; QPD: Quadrant Photo Detector;

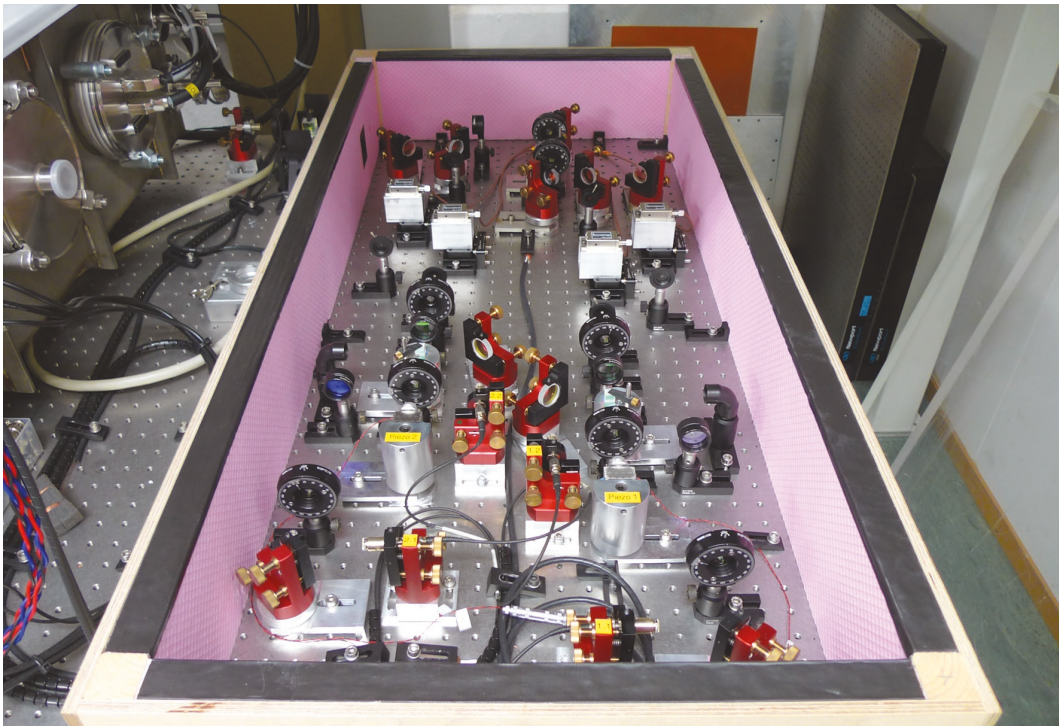


Figure 3.2: Photograph of the setup for heterodyne frequency generation in duplicate for supplying two interferometers.

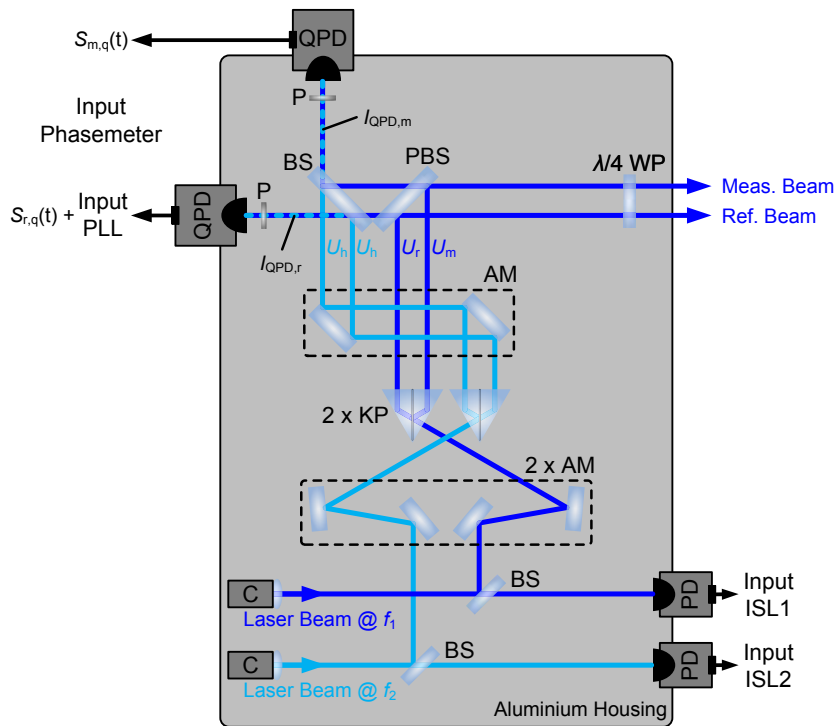


Figure 3.3: Schematic of the interferometers' optical setup. Compared to previous versions it features Köster prisms for generating the parallel beam pairs. C: Collimator; AM: Set of (adjustable) Alignment Mirrors; KP: Köster Prism; PBS: Polarising Beam Splitter; BS: 50/50 Beam Splitter; WP: Wave Plate; P: (thin film) Polarisers; QPD: Quadrant Photo Detector; PD: Photo Detector; ISL: Intensity Stabilisation Loop; PLL: Phase Locked Loop; $S_{m,r}$: QPD Output Signal;

accuracy in the (differential) out of plane angle between the output beam pair, specified to be $< \pm 1$ arcsec, which helps to maintain high contrast after long travel distances. The contrast achieved during measurement varied between $\approx 0.7 - 0.95$, dependent on the level of movement of the geometrical centre of the SPM during measurement. Back-reflections at the entrance and exit surface of the KPs are minimised by an anti-reflective (AR) coating. Additional changes include the PBS and BS for beam superposition, represented by plates (also AR coated at the backside) instead of cubes, in order to avoid additional back-reflections and etalons in the optical path. Further changes include additional thin film polarisers in front of the QPDs, which increase the heterodyne contrast and reduce polarisation variations due to coupling with different polarisation states, for minimising phase noise.

In the previous interferometer, cracking of optical components has been observed, caused by large variations of the ambient temperature in the laboratory. Since the optical components have been directly glued to the aluminium supports without a proper compensation for differential thermal expansion, the components were subject to high internal stress, which sometimes caused damage. In order to avoid such damages, a new optics support has been developed featuring flexures in order to compensate for differential thermal expansion between the support and the optical component. More specifically, the support features three flexures arranged at equidistant angles of 120° for the radial mounting of the optical component. Figure 3.4 shows a rendering of the new optics support. The thickness of the flexures is 0.6 mm for the version intended to hold $\varnothing 25\text{ mm}$ optics and 0.4 mm for the version intended to hold

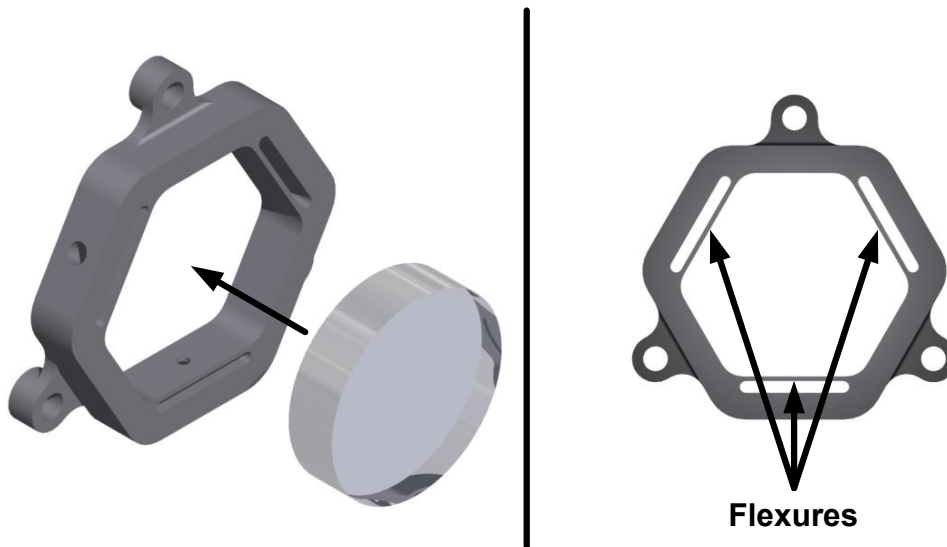


Figure 3.4: Rendering of the new optics support, made of an aluminium alloy, which features 3 flexures for a compensation of differential thermal expansion between the support and the optical component. The holes in the frame are used to glue the optics onto the flexures. The figure shows the version for $\varnothing 25$ mm optics.

$\varnothing 12.7$ mm optics. These values are demanded by the manufacturer considering the geometry, the choice of material (aluminium alloy EN-AW6061) as well as the manufacturing method applied (electrical discharge machining). By using the FEM simulation tool implemented in Inventor (by Autodesk), the stiffness of the flexures is calculated to be $\approx 0.94 \text{ N}/\mu\text{m}$ and $\approx 0.90 \text{ N}/\mu\text{m}$ respectively for the two different versions of the optics support. This leads to the temperature dependent force coefficients of 0.27 N/K and 0.13 N/K respectively (per flexure), when considering coefficients of thermal expansion (CTE) of $23.1 \cdot 10^{-6} \text{ K}^{-1}$ for the optics support (aluminium alloy) and $0.5 \cdot 10^{-6} \text{ K}^{-1}$ for the optical component (fused silica). These values are low enough to avoid damage of the optical component, at least within the normal ambient temperature range in the laboratory ($\approx 18^\circ\text{C} - 32^\circ\text{C}$). In the final step, the optics are glued to the flexure hinges in order to fix their position. For that, holes are drilled in the frame of the optics support as well as the middle of the individual flexure.

All adjustment mirrors (AMs) in the interferometer are mounted in commercially available, top-adjustable mirror supports (by New Focus). These mounts promise high pointing stability and provide the DoFs for beam alignment within the interferometer. The alignment is in particular critical for the KPs, since it defines the parallelism of the beam pair, as well as the final BS, since it defines the quality of the superposition of the laser beams. Figure 3.5 and 3.6 show photographs of both interferometers, which feature housings milled from a single block with additional screwed covers for increased stiffness. The PDs (for the ISL) and QPDs (for the PLL as well as displacement measurements) are screwed to the rigid side walls of the housings.

The redesigned interferometers also feature new electronics, specifically developed for signal detection and processing at the heterodyne frequency of $f_h = 10 \text{ kHz}$. It comprises the front-end electronics including the PDs / QPDs for laser light detection and the back-end electronics with the ADCs for digitisation. All circuit diagrams are included in Appendix A.2.

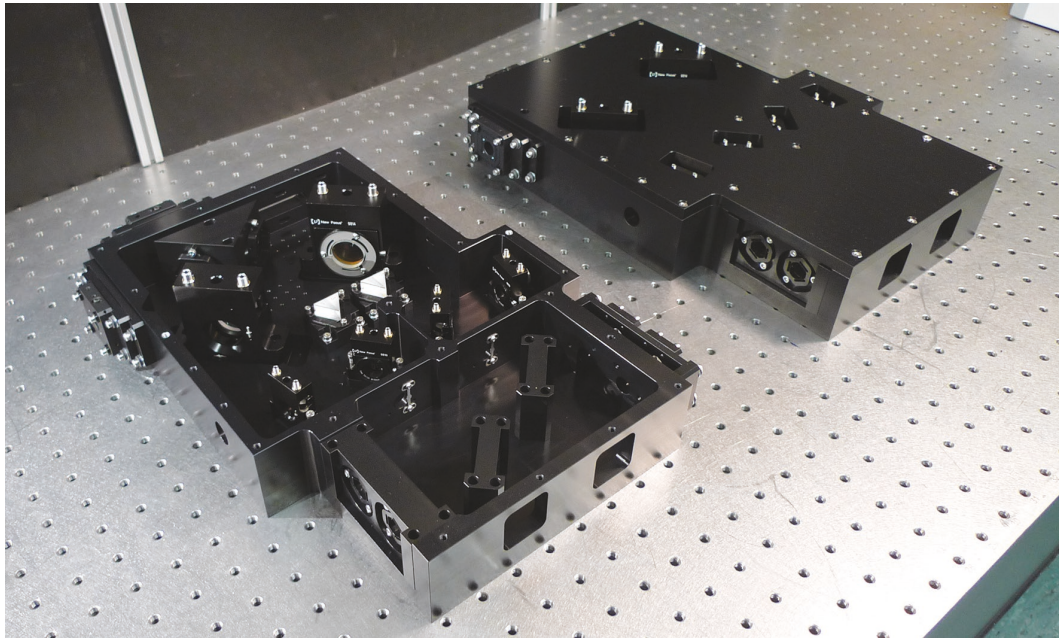


Figure 3.5: Photograph of both heterodyne interferometers employed, the one in front with removed cover.

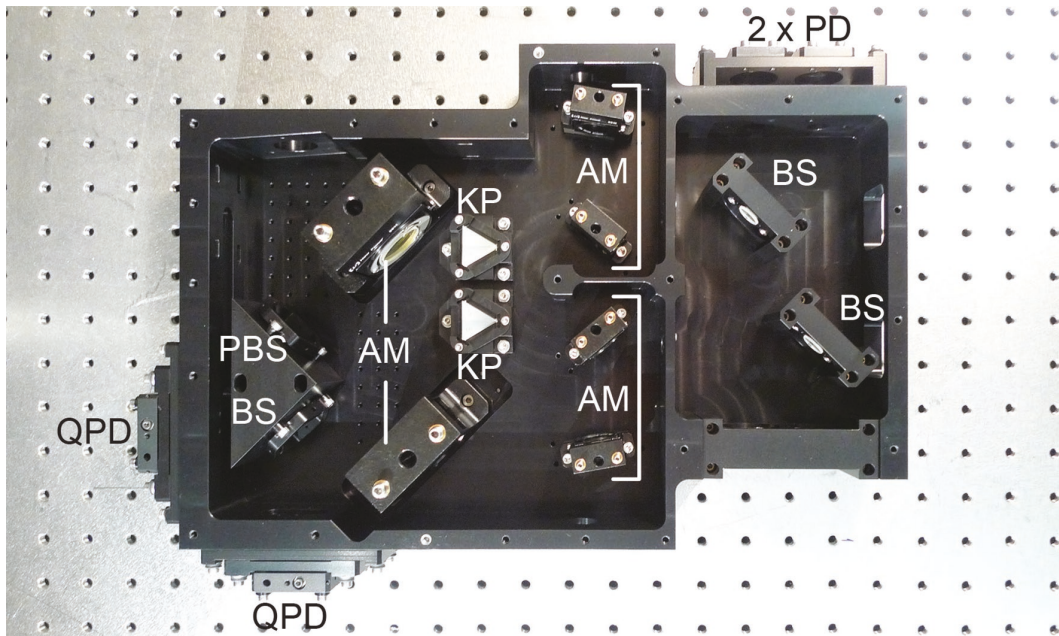


Figure 3.6: Photograph (top view) of one of the heterodyne interferometers during assembly. BS: 50/50 Beam Splitter; AM: Set of (adjustable) Alignment Mirrors; KP: Köster Prism; PBS: Polarising Beam Splitter; QPD: Quadrant Photo Detector; PD: Photo Detector;

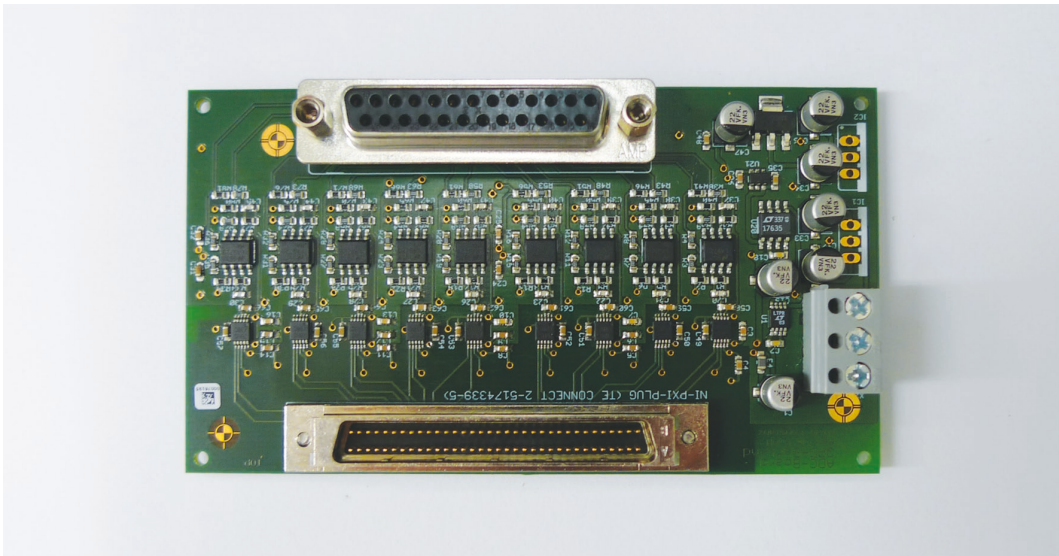


Figure 3.7: Photograph of the ADC circuit board of the back-end electronics.

The ADC circuit board is depicted in Figure 3.7 and holds the power supply unit (PSU) for voltage regulation and 9 channels, each with a 16 bit ADC-IC (8 channels for the QPD signals and 1 optional channel). The PSU mainly consists of voltage regulators with $\pm 8\text{ V}$ output voltage in the first stage (which is also used to feed the PSU of the front-end electronics including the QPDs) and $\pm 5\text{ V}$ output voltage in the second stage. This second stage is subdivided into a symmetrical $\pm 5\text{ V}$ supply line feeding the analogue electronics on the circuit board and a $+5\text{ V}$ supply line feeding the digital domain of the ADC chips. The latter one additionally includes a ferrite bead for decoupling in order to suppress high frequency voltage noise in the supply lines. The ADC channels are designed for symmetrical input signals in order to enable differential signalling between front-end and back-end electronics. This method ensures a high level of common mode rejection and is therefore more robust against outer disturbances compared to single ended signalling. Each channel features an amplification stage, a low-pass filter and an offset stage with a $+2.5\text{ V}$ voltage shift for adapting the input signals to the ADC (common mode) input range (0 V to $+5\text{ V}$) before the signal is fed into the ADC-IC. The ADC-ICs are additionally thermally coupled via thermal bridges made of copper in order to:

- Run them at lower temperatures, hence reducing measurement noise.
- Keep them at equal temperatures, which increases the level of common mode rejection for (measurement) errors driven by thermal fluctuations.
- Increase their thermal stability by raising the thermal capacitance, which further reduces thermal driven (measurement) noise.

During measurement all 9 ADC channels are clocked simultaneously at a sampling rate of 160 kS/s as used in the original interferometer design. Oversampling with respect to the heterodyne frequency is used for averaging, hence increasing the signal to noise ratio.

The QPD circuit board, depicted in Figure 3.8 holds the PSU for voltage regulation, an InGaAs pin quadrant photo diode and 4 channels for signal processing. The PSU is fed by the

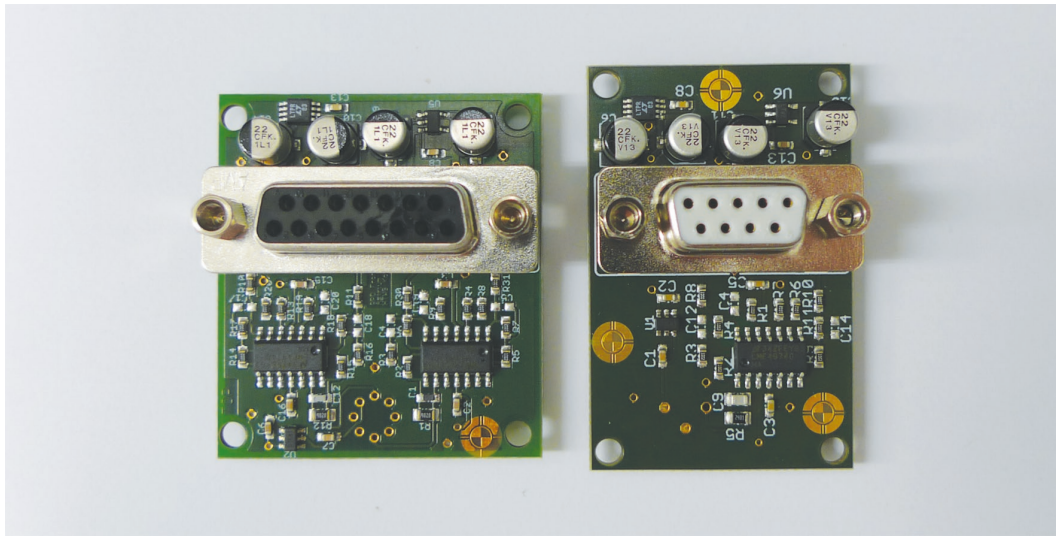


Figure 3.8: Photograph of the QPD (left) and PD circuit board (right) of the front-end electronics.

back-end electronics with $\pm 8\text{ V}$ from its first stage. From that, voltage regulators are used for generating a symmetrical $\pm 5\text{ V}$ supply line feeding the analogue electronics on the circuit board. Additionally the PSU holds a band gap voltage reference for generating a reverse bias voltage for the photo diode in order to reduce its junction capacitance. This bias voltage has to be highly stable, since variations in bias voltage will introduce measurement noise. An InGaAs pin photo diode (by Hamamatsu) is selected since this semiconductor material shows high sensitivity at a wavelength of 1064 nm . Its active area has a diameter of 2 mm . Each channel on the circuit board for processing the diode signals features an amplification stage with a transimpedance amplifier in order to convert the diode's output current into a proportional output voltage, a 30 kHz low-pass filter and a balancer circuit to generate the symmetrical signal for differential signalling to the back-end electronics. The PD circuit board for single element photo diodes, which is used for the ISL, is based on the electrical design of the QPDs, however, reduced to one channel.

A performance measurement of the new electronics has been performed, in which 8 synthetic and phase correlated 10 kHz signals, generated by a signal generator are fed via $20\text{ k}\Omega$ resistors into the input channels of the QPD boards. These synthetic signals simulate the optical signals detected by the QPDs (the optical system of the interferometers is not used in this measurement). The results are depicted in Figure 3.9, presented as the ASD of the recorded differential displacement signal between the QPDs, thus representing the displacement noise. It shows amplitudes of $\approx 100\text{ fmHz}^{-0.5}$, rising with an $1/f$ slope at frequencies below $\approx 1\text{ Hz}$, which is most likely attributed to fluctuations in ambient temperature in the laboratory, in which the electronics is operated.

Further on, the performance of both interferometers is measured. Hereby the interferometer's measurement and reference laser beam were reflected on a common reference mirror, which is screwed to the interferometer housing. By applying this configuration, differential path length changes in the interferometer are measured, which represent the interferometer's displacement noise including its electronics. The results are displayed in Figure 3.10, also presented as the ASD of the recorded differential displacement signals between the QPDs. They show amplitudes of $\approx 200\text{ fmHz}^{-0.5}$, rising with an $1/f$ slope at frequencies below $\approx 10^{-1}\text{ Hz}$.

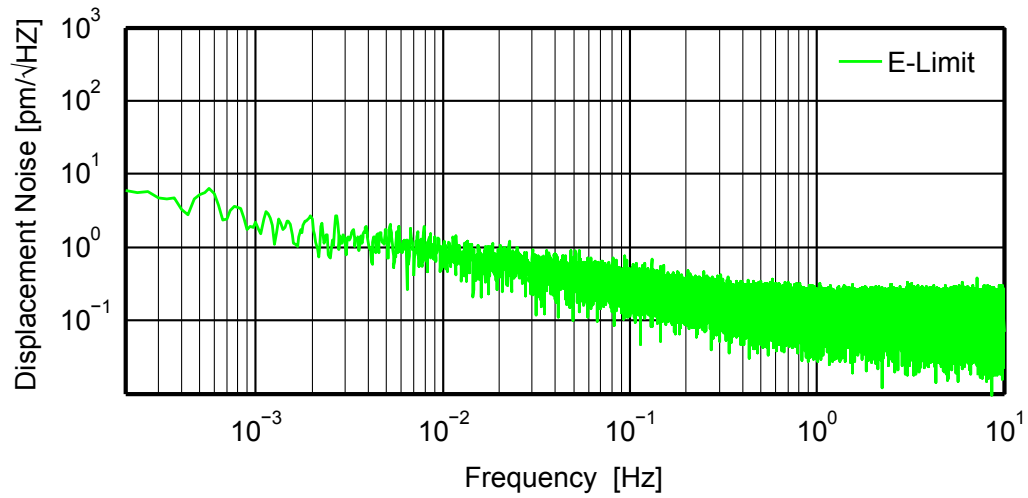


Figure 3.9: ASD of the displacement noise of the new interferometer electronics. The measurement includes 8 synthetic, phase correlated 10 kHz signals, which are fed into the input channels of the QPD boards, thus simulating the optical signals detected by the QPDs.

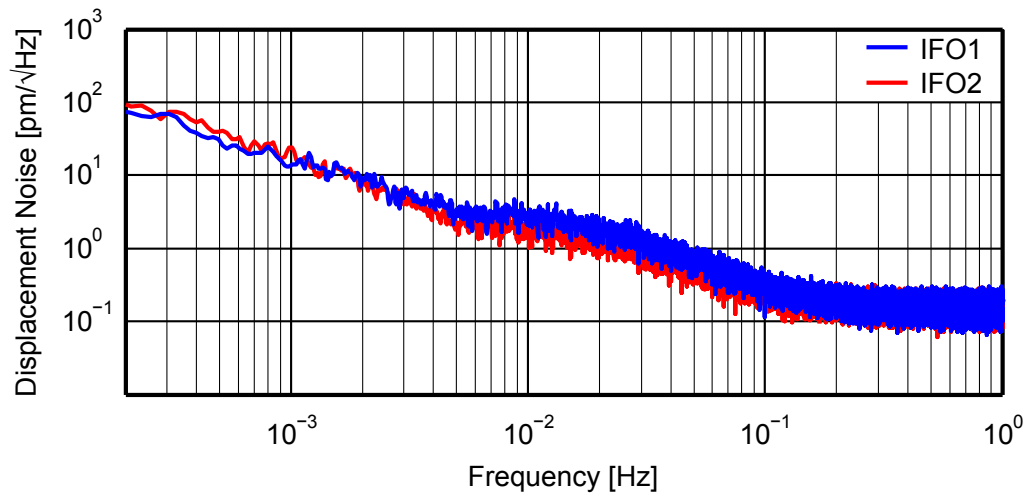


Figure 3.10: ASD of the displacement noise of the heterodyne interferometers employed. For this measurement, the interferometers' measurement and reference laser beams are reflected on a common reference mirror, which is screwed to the interferometer housing.

3.1.1.2 Structure & Optical Setup

A schematic of the complete measurement setup for performing surface topography measurements of spheres is depicted in Figure 3.11. The two heterodyne interferometers are mounted in an opposed configuration and constantly measure the distance to the individual reference mirror and to the SPM surface. For this, the interferometers' reference laser beams are aligned onto the reference mirrors near the SPM, and the measurement beams are aligned onto the geometrical centre of the SPM. The opposed interferometer configuration has been chosen, since it enables the determination of parasitic SPM movements and the derivation of associated correction functions / a direct compensation for parasitic SPM movements in measurement direction, when summing up the displacement signals x_1 and x_2 .

The interferometers are placed onto an aluminium base structure using an isostatic mounting concept with one locating bearing and two floating bearings. Therefore each interferometer is equipped with a support structure made of aluminium featuring three contact interfaces made of steel, a bore with chamfer, a slot with chamfers and a plane, which are situated on three posts made of Zerodur with hemispheric top ends. The contact points are designed to be within the optical plane of the interferometer in order to reduce changes in beam height in the setup, due to thermal expansions. A photograph of the setup (during assembly) is depicted in Figure 3.12 featuring the base structure and both interferometers including the support structure and posts. The positions of the locating bearing of each interferometer is chosen to be in line with its measurement laser beam and the geometrical centre of the SPM in order to reduce lateral movements of the measurement beams caused by thermal expansions of the setup. Two adjustable mirror supports (by Lees) are mounted at the side walls of each interferometer housing, which enable the alignment of the output beams, more specifically the measurement beams onto the geometrical centre of the SPM.

The SPM is rotated by an automated rotation stage ALAR 100-LP (by Aerotech), which is positioned in the centre of the setup between the two interferometers and mounted at the underside of the base structure. An additional support is positioned on the rotation stage in order to hold the SPM. This support is depicted in Figure 3.13 and can be aligned with respect to the rotation axis of the rotation stage by a measurement gauge (for rough alignment) and the interferometer displacement signals (for fine alignment). It is made of stainless steel and features three contact faces for holding the SPM leading to a nearly ideal three point support, at least when ignoring deformation in the contact points due to the SPM's weight. Additionally the support features a mechanism at its top, realised by a shaft-hub joint, in order to enable a relative rotation φ_{SPM} of the SPM with respect to the rotation axis. This facilitates a differentiation between topography and error motion induced signals in the data analysis of the measurement results as discussed in the next section.

The mirrors for reflecting the interferometers' reference laser beams are located near the SPM surface in order to compensate for thermal expansion of the aluminium base structure as well as to avoid the necessity of a laser frequency stabilisation. Each reference mirror is glued to a flexure hinge, which enables an adjustment around the vertical axis. Additionally, each flexure hinge is glued onto an individual pivoted plate made of Zerodur, which enables an adjustment around the horizontal axis. Figure 3.14 shows a photograph of the reference mirror setup. This configuration enables proper alignment of the reference laser beams, since their direction of propagation is directly coupled to the direction of propagation of the corresponding measurement laser beam, due to the shared mirrors at the output of the interferometers. The material Zerodur is used due to its low CTE, hence providing high thermal stability. Hereby,

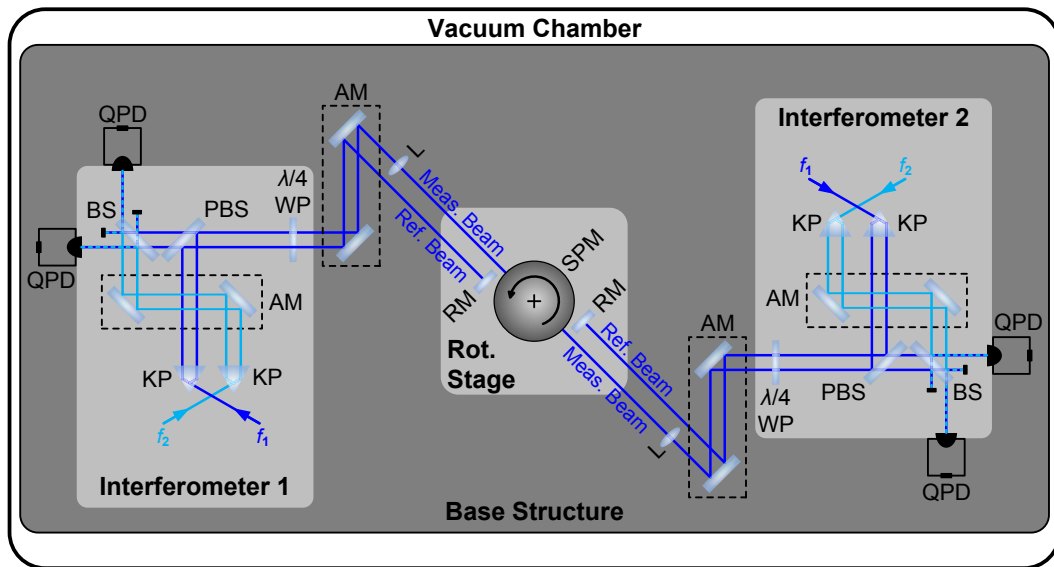


Figure 3.11: Schematic of the measurement setup for performing surface topography measurements of spheres including its two opposed heterodyne interferometers for non-tactile optical measurements. The measurement laser beams are aligned onto the geometrical centre of the SPM in the middle of the setup, which sits on an automated rotation stage for actuation, while the reference laser beams are aligned onto individual reference mirrors. KP: Köster Prism; AM: Set of (adjustable) Alignment Mirrors; BS: 50/50 Beam Splitter; PBS: Polarising Beam Splitter; WP: Wave Plate; L: Lens (for longitudinal mode match); RM: Reference Mirror; SPM: Spherical Proof Mass; QPD: Quadrant Photo Detector;

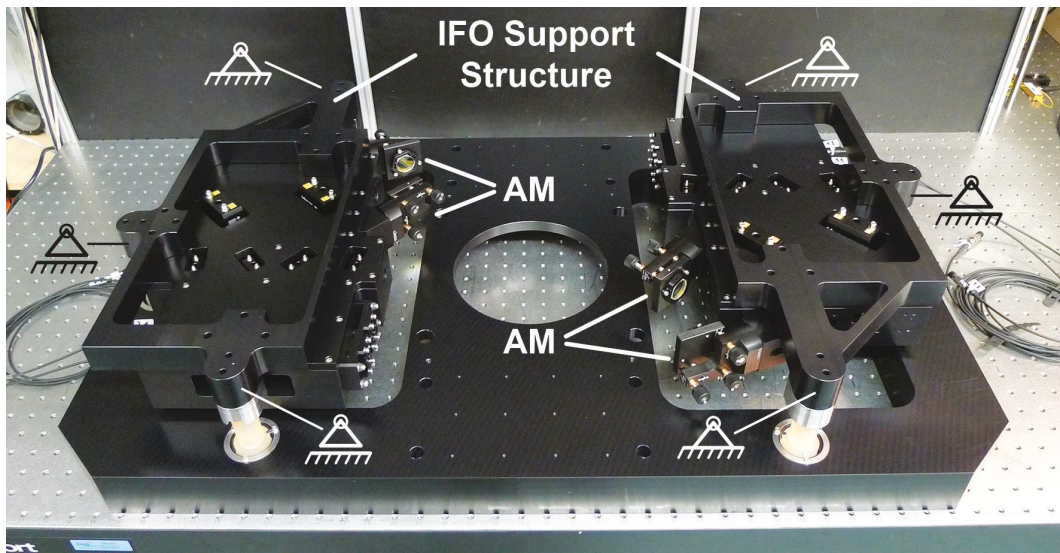


Figure 3.12: Photograph of the measurement setup during assembly, including the base structure and both heterodyne interferometers with their support structure and Zerodur posts. AM: Set of Alignment Mirrors (for beam alignment onto the SPM);

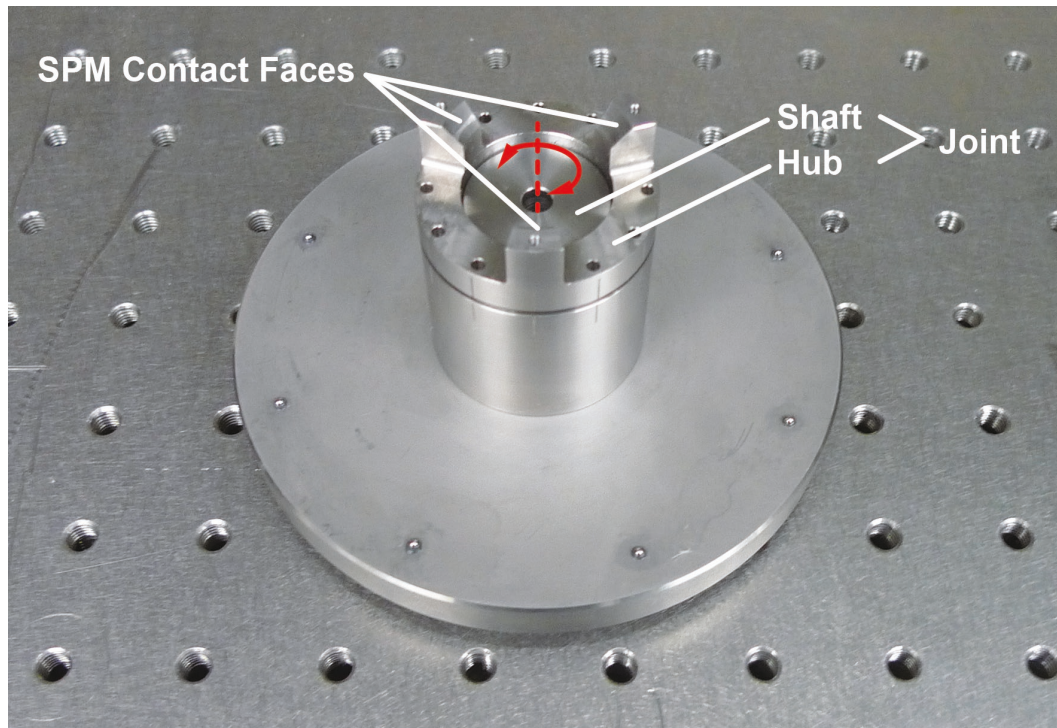


Figure 3.13: Photograph of the SPM support employed, featuring a mechanism (shaft-hub joint) for relative rotation of the SPM with respect to the rotation stage. This facilitates a differentiation between topography and error motion induced signals in the data analysis of the measurement results.

the Zerodur plates sit on ceramic spheres, which are positioned on the neutral lines of the base structure with respect to the direction of propagation of the measurement beams. This solution enables a compensation of differential thermal expansion between the individual parts. In order to ensure modularity, the reference mirror setup is placed on a separate plate, which is screwed onto the base structure.

The longitudinal mode match of the measurement beams onto the SPM surface is realised via optical lenses. Thereby the lens supports are mounted on the same plate as the reference mirror setup. This mode match is required, since a normal reflection of the measurement beams requires that their wavefront curvature matches the curvature of the SPM surface. By varying the lens position, the wavefront curvature can be adjusted individually. For the first measurements, the mode match is performed with only one spherical lens in each measurement beam. However, the setup's design also allows for the use of multiple lenses per measurement beam. Besides an adaption of the wavefront curvature, this configuration would also enable the use of a defined / specific beam size on the SPM surface. Thereby, the achievable beam sizes are only limited by the available space between the alignment mirrors at the output of the interferometers and the SPM surface as well as the availability of specific focal lengths of the lenses.

The lenses are mounted in an adapted version of the optics support described previously, which also features flexures for the compensation of differential thermal expansion. These supports are screwed at commercially available 3-axis translation stages in order to enable precise alignment. Additionally, each translation stage is mounted onto a sliding carriage for a quick positioning of the lens along the beam propagation direction, see Figure 3.15.

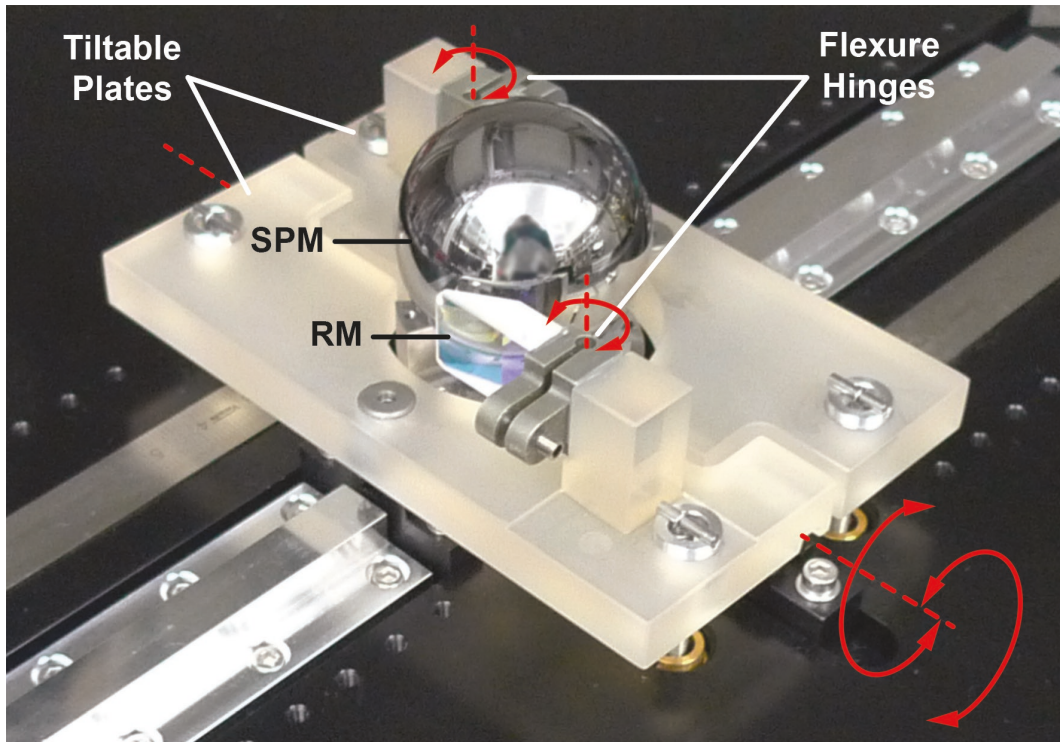


Figure 3.14: Photograph of the reference mirror setup. The mirrors are glued to the flexure hinges as well as to the (tiltable) Zerodur plates, which enables proper alignment of the individual reference beam. SPM: Spherical Proof Mass; RM: Reference Mirror;

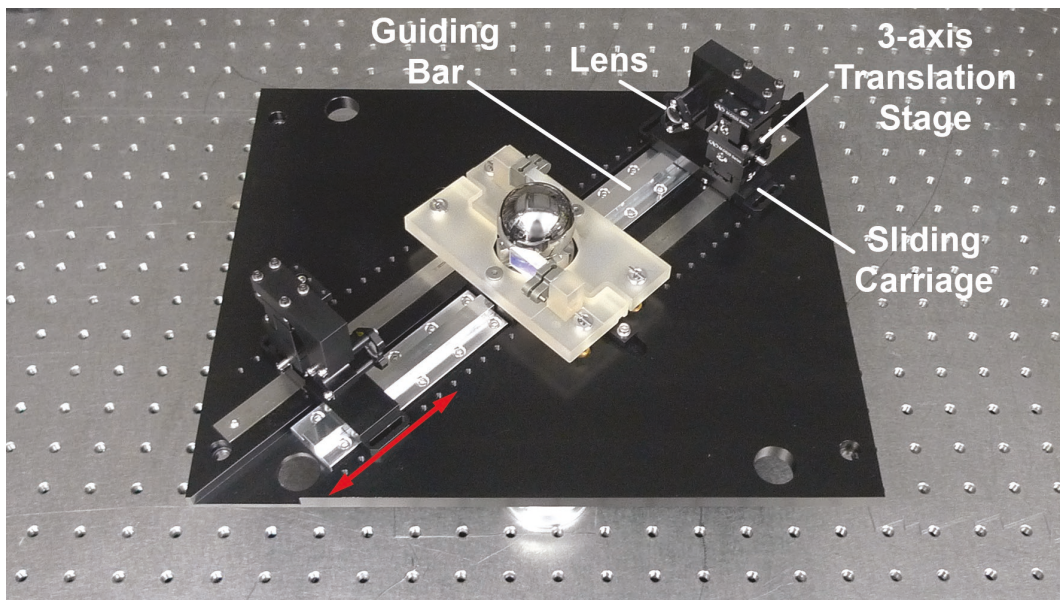


Figure 3.15: Photograph of the lens supports including the 3-axis translation stages for lens alignment and the sliding carriages for quick lens positioning along the propagation direction of the measurement beams.

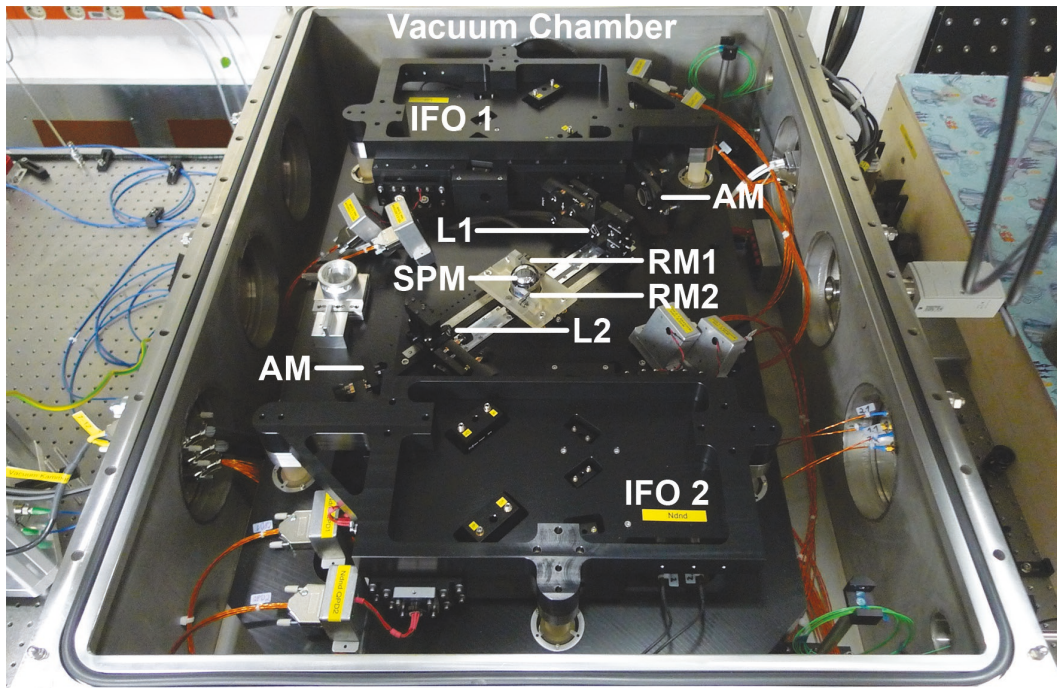


Figure 3.16: Photograph of the measurement setup in the vacuum chamber. IFO: Heterodyne Interferometer; AM: Set of Alignment Mirrors (for beam alignment onto the SPM); L: Lens (for longitudinal mode match); RM: Reference Mirror; SPM: Spherical Proof Mass;

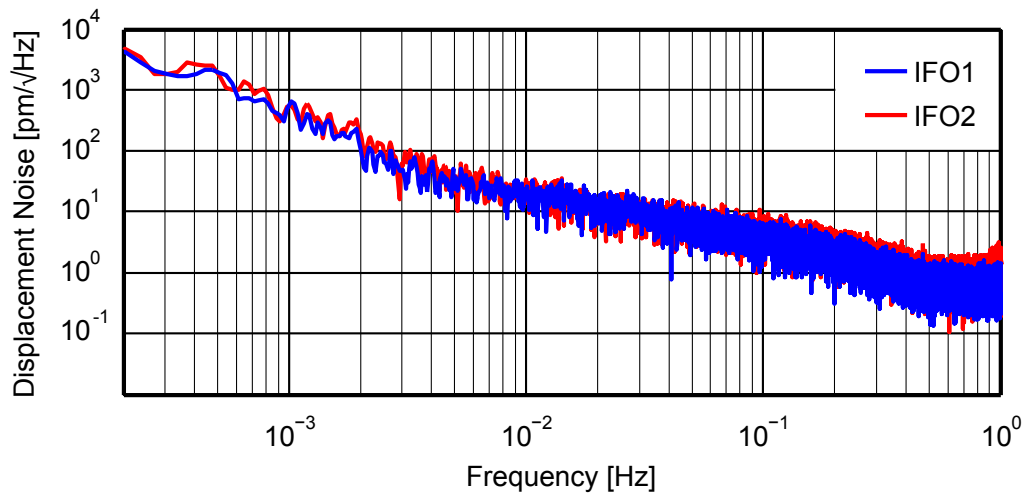


Figure 3.17: ASD of the displacement noise of the measurement setup as a function of frequency. For the measurement, the interferometers' measurement laser beams are reflected on the static SPM surface and the reference laser beams are reflected on the reference mirrors.

In order to reduce measurement noise due to air fluctuations, the setup is located in a vacuum chamber, see Figure 3.16, equipped with a turbo-molecular pump. External to the chamber are the optical setup for heterodyne frequency generation and the data acquisition / processing electronics, which are both operated in ambient laboratory conditions. The ASD of the setup's displacement noise is shown in Figure 3.17, with the interferometers' measurement laser beams reflected on the static SPM surface and the reference laser beams reflected on the reference mirrors. The results show displacement amplitudes at the low pm level, rising with an $1/f$ slope. Compared to the results of the interferometer performance (presented earlier), the level of the white noise floor as well as the corner frequency of the $1/f$ slope have both been increased, as expected. The increased noise floor is attributed to the larger number of optics, supports and mechanism within the setup, rising its sensitivity against mechanical vibrations. The increased corner frequency of the $1/f$ slope is most likely caused by the longer optical paths. These are subject to path length changes due to thermal fluctuations as well as additional noise due to pointing errors, introduced by the mirror supports at the interferometer output and the 3-axis translation stages of the lenses, whose parasitic movements couple to pointing. Nonetheless the setup shows an adequate performance to enable reproducible sub- μm surface topography measurements. However, this assumption does not consider influences introduced by movements of the geometrical centre of the SPM during measurement, which are expected to generate additional noise.

3.1.2 Measurements & Results

First step is the beam characterisation of both of the measurement laser beams involved. In general, they introduce a low-pass filter effect on the measurement data, dependent on their sizes, which has to be considered in the selection of the actuation step size / rate of the rotation stage or SPM, respectively. Subsequent investigations serve for the selection and assignment of the actuation mode and parameters. Finally, several topography measurements along a great circle of the SPM have been performed, including the development of a suitable data evaluation algorithm for the correction of error movements of the SPM's geometrical centre due to misalignment and parasitic movements of the rotation stage. Such a correction is required in order to suppress their dominant contribution in the measurement results.

3.1.2.1 Laser Beam Characterisation

During measurement, the SPM surface topography is averaged over the cross-section of the measurement laser beams, which introduce a low-pass filter effect, suppressing surface details smaller than $\approx 2/(\pi \cdot d_m)$ with d_m representing the beam diameter of the corresponding measurement laser beam. This effect has a major influence in the resolution and the topography amplitudes of the results and calls for a proper determination of the beam sizes. The diameters $d_{m,1,2}$ of the measurement laser beams on the SPM surface can be estimated based on measurements involving the razor blade method, which has already been described in more detail in Chapter 2 of this thesis.

The measurements have been performed directly in front of the SPM, thus including the lenses for longitudinal mode match (both with a focal length of $\approx 100\text{mm}$), which leads after data evaluation to estimated beam diameters (on the SPM surface) of $d_{m,1} = 175\ \mu\text{m}$ (interferometer 1) and $d_{m,2} = 181\ \mu\text{m}$ (interferometer 2). These values result in a low-pass filter effect for spatial frequencies below $\approx 3.6 \cdot 10^{-3}\ \mu\text{m}^{-1}$ and influence the selection of

Input Beam	$r_{b,0}$	$x_{b,0}$
IFO 1, f_1	391.8 μm	740.6 mm
IFO 1, f_2	405.0 μm	751.0 mm
IFO 2, f_1	375.5 μm	737.1 mm
IFO 2, f_2	371.0 μm	733.3 mm

Table 3.2: Estimated parameters of the interferometer’s input laser beams $r_{b,0}$ (beam radius in waist) and $x_{b,0}$ (distance of waist behind collimator), based on measurements using the razor blade method. These parameters are one of the major inputs of the OptoCad model, which is used for fast diameter estimation of the measurement beams.

the actuation step size / rate of the SPM (depending on the actuation mode used), which is described in more detail in the following section.

As described above, the setup is able to accommodate two lenses in each measurement beam for future beam adaption, hence forming a telescope, which enables the application of specific beam diameters on the SPM surface. This flexibility is required, since the final beam sizes of the optical read-out within the inertial sensor have not been defined yet and the surface map should be adapted to the final sensor configuration. Additionally this flexibility also enables an assessment of finding suitable beam sizes for the optical read-out, which will achieve the best performance in the SPM’s CoG position determination with respect to accuracy and speed. However, in order to exploit this flexibility it is reasonable to implement a solution for a fast estimation of the laser beam diameters $d_{m,1,2}$ in the setup, without using the time-consuming razor blade method every time.

The chosen solution involves a calculation of the beam propagation within the measurement setup using a paraxial Gaussian model - more specifically a ray transfer matrix analysis - based on the parameters of the interferometer input beams at the fibre collimators. These parameters have already been determined during interferometer assembly using the razor blade method and are illustrated in Table 3.2. The simulation tool utilised is the OptoCad software, which is a freeware for ray tracing in optical systems, see Figure 3.18. This tool calculates a selection of beam parameters on all optical surfaces within the model, including the curvature of the wavefront and the laser beam diameter. All under consideration of the position, alignment, geometry and material of the optical components involved. A validation of the model’s results is performed using the beam diameters presented above. When locating the lenses in the model at the same position, the simulated beam diameters are calculated to be $d_{m,1} = 174 \mu\text{m}$ and $d_{m,2} = 186 \mu\text{m}$, which is in good agreement with the results based on the razor blade method, showing only negligible errors of 0.6% and 2.8%, respectively. This solution enables a considerably faster and simpler approach for an estimation of the beam diameters on the SPM surface.

3.1.2.2 Proof Mass Actuation Mode

The rotation stage offers a choice of its actuation mode, a stepwise SPM movement - similar as applied in the mirror characterisation measurements featuring the pendulum mechanism (presented in Chapter 2 of this thesis) - and continuous SPM movement. Although the stepwise movement enables an averaging of the measured displacement value at each position, which helps reducing measurement uncertainty, this mode exhibits long measurement durations

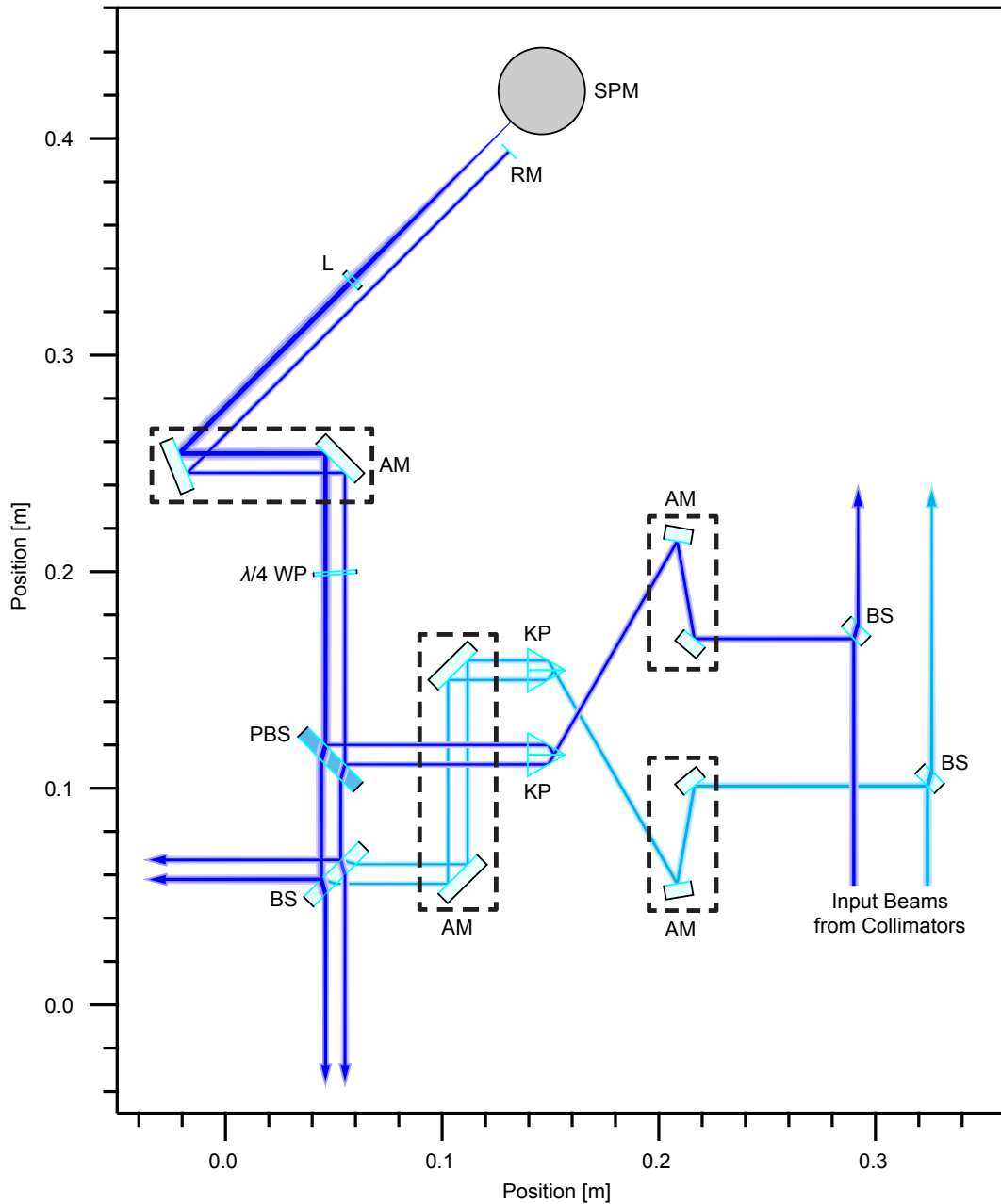


Figure 3.18: Picture of the OptoCad model, used for a fast estimation of the measurement beam diameters on the SPM surface. BS: 50/50 Beam Splitter; AM: Set of (adjustable) Alignment Mirrors; KP: Köster Prism; PBS: Polarising Beam Splitter; WP: Wave Plate; L: Lens (for longitudinal mode match); RM: Reference Mirror; SPM: Spherical Proof Mass;

due to the constant starting and stopping processes. Additionally, one has to consider a ring-down time after each stop in order to suppress oscillations and to ensure a static SPM condition. However, long measurement durations work against the positive averaging effect, when considering the limited long-term stability of the measurement setup. Therefore both actuation modes have been tested by a set of measurements with stepwise and continuous SPM movement, where the latter has been investigated in more detail by applying different (constant) angular rates between $\omega = 0.3^\circ/\text{s}$ and $\omega = 24.0^\circ/\text{s}$.

In order to quantify the measurement uncertainty, each measurement is performed over multiple rotations and the standard deviation σ is calculated based on the deviation from the averaged signal. The continuous SPM movement at low and medium angular rates show the lowest uncertainties, whereas stepwise SPM movement and continuous SPM movement at high angular rates exhibit increased uncertainties. This behaviour can be explained by the long measurement durations involved for the stepwise movement as well as the low sampling rate of the interferometers for the continuous movement (at high angular rates), which limit the dynamic range of the phasemeters at high frequencies.

Regarding the selection of a suitable angular rate of the rotation stage, it is important to mention, that a continuous SPM movement will lead to an additional low-pass filter effect of the measurement data, besides the averaging over the cross-section of the measurement laser beams involved. This effect is caused by the data acquisition and processing scheme of the phasemeters - already presented in more detail in Chapter 2 of this thesis - in which the QPD signals are sampled at $f_{s,1} = 160 \text{ kHz}$ and later on low-pass filtered and down-sampled to $f_{s,2} = 20 \text{ Hz}$, hence introducing an averaging of the SPM surface topography. The filter utilised is a 3rd order Butterworth low-pass filter with a corner frequency at $\approx 6 \text{ Hz}$, whose transfer function spectrum \tilde{g}_{LPF} in the frequency domain can be described by:

$$\tilde{g}_{\text{LPF}}(f) = \left(\frac{C_{\text{LPF}} \cdot z}{z - (1 - C_{\text{LPF}})} \right)^n \quad (3.1)$$

with

$$z = e^{(i2\pi f t_{s,1})} \quad (3.2)$$

where $n = 3$ represents the filter order, $C_{\text{LPF}} = 2^{-11}$ represents the filter parameter and z represents the complex z -variable with $t_{s,1} = 1/f_{s,1}$. This implementation avoids the use of the rare DSP48 slices on the FPGA board, which are used for multiplications.

A transformation of this transfer function into the spatial frequency domain ν accounts for the angular rate ω of the SPM and is performed using the conversion of the respective spatial frequencies to frequencies with $f = \nu \cdot \omega$. Figure 3.19 (top) displays the transferred filter spectra, which show the dependency between the angular rate ω applied and the cut-off frequency of the filter in the spatial frequency domain. An increased angular rate enlarges the averaging of the SPM topography, hence reducing resolution and alters the topography amplitudes of the results. The figure also includes the spectrum of the low-pass filter effect introduced by a (Gaussian) laser beam of diameter $d_b = 175 \mu\text{m}$ (see Equation 2.29), as utilised in the measurements.

Based on these results the angular rate is chosen to be $\omega = 1.2^\circ/\text{s}$, which is a good compromise between short measurement durations and low losses in resolution / errors in topography amplitudes, resulting in measurement durations of 300 s per rotation and an angular resolution of 0.06° (which represents a surface overlap of $\approx 88\%$ between the steps). The influence of the angular rate with respect to the measured topography is displayed in Figure 3.19 (bottom),

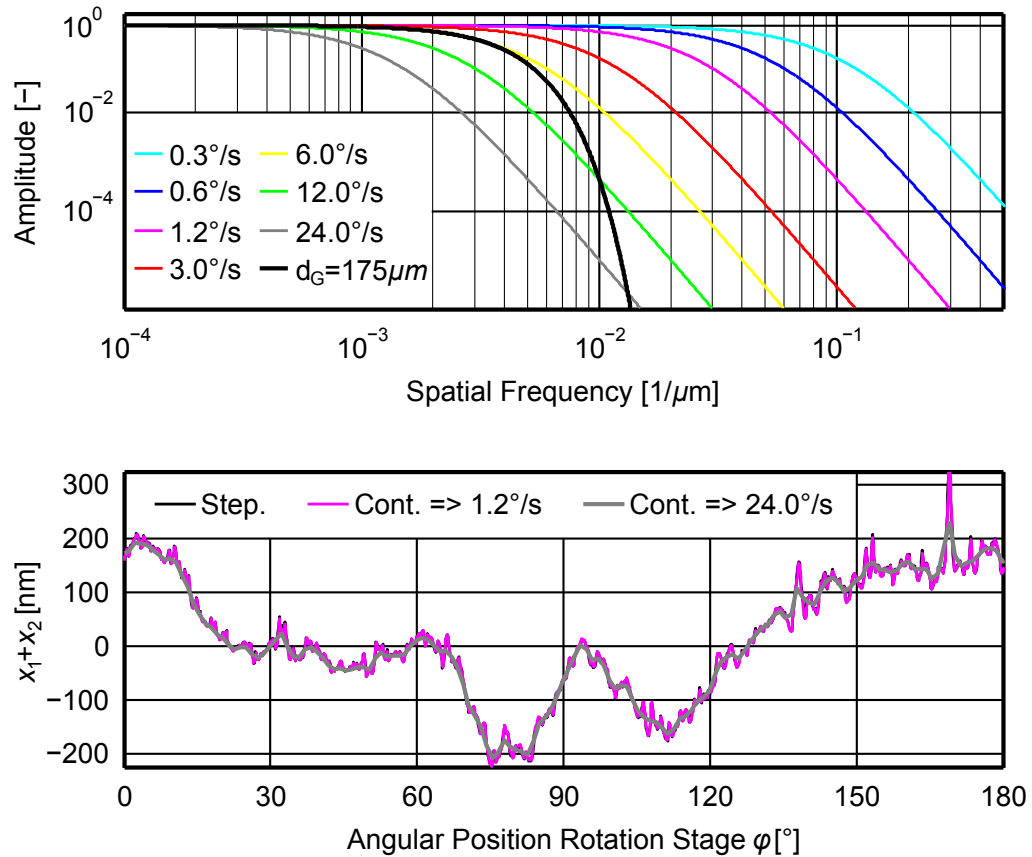


Figure 3.19: Spectra of the phasemeters' low-pass filters in the spatial frequency domain, depicted for different angular rates of the rotation stage (top). The spectrum of the low-pass filter effect introduced by a (Gaussian) laser beam of diameter $d_b = 175 \mu\text{m}$ is shown in black. The angular rate for the following measurements is chosen to be $\omega = 1.2^\circ/\text{s}$, based on these spectra, which is a good compromise between short measurement durations and low losses in resolution / errors in topography amplitudes. The sum signal of the interferometers $x_1 + x_2$, representing the change in diameter of the SPM, shows the influence of the angular rate on the measured topography (bottom).

showing the sum signal of the interferometers $x_1 + x_2$, which represents the change of the diameter of the SPM and directly compensates for error movements of the SPM's CoG in measurement direction (x -direction). One can see, that the curves for a stepwise SPM movement and a continuous SPM movement at low angular rates are nearly identical, however, the curve for a continuous SPM movement at high angular rates shows a considerably reduced resolution and strongly influenced topography amplitudes.

3.1.2.3 Surface Mapping

The surface topography measurements are performed using two heterodyne interferometers, whose measurement laser beams are aligned onto the geometrical centre of the SPM and reference laser beams are aligned onto individual reference mirrors, mounted to the setup's base structure. A precise rotation stage is rotating the SPM, hence the measure-

ment beams are scanning over the SPM surface. By means of the shaft-hub joint, integrated in the proof mass support, a set of measurements with different SPM orientation offsets $\varphi_{\text{SPM}} \in \{0, \pi/3, 2\pi/3, \pi, 4\pi/3\}$ is performed, which in combination with the opposed interferometer configuration helps to identify and determine parasitic SPM movements. These are used to derive associated correction functions via a dedicated mathematical model. Based on these corrections it is possible to extract the SPM surface topography from the recorded measurement data. The opposed interferometer configuration also enables a direct compensate of parasitic SPM movements in measurement direction, when adding the interferometer signals together.

Mathematical Model The recorded interferometer signals x_1 and x_2 are calculated from the interferometers' quadrant photo detector (QPD) signals and represent the differential displacement changes between the measurement and the reference path. Besides the SPM surface topography, they also include parasitic SPM movements, which are introduced by misalignment and error movements of the rotation stage. In order to extract the surface topography from the data, these systematic and stochastic noise sources have to be taken into consideration, namely:

- Eccentricity of the geometrical centre of the SPM with respect to the actual rotation axis.
- Radial and axial error movements of the SPM, caused by the angular contact ball bearing in the rotation stage.
- Mechanical and thermal deformations of the setup, especially non-common-mode contributions from the SPM mounting structure.

The latter should not limit the results, since the long term stability of the setup has already been proven to be suitable for sub- μm measurement accuracies, as shown in Figure 3.17

A schematic of the model employed for correction of these noise sources is depicted in Figure 3.20. The reference frame c_{IFO} is positioned in the centre between both interferometers. Due to the opposed configuration, the interferometer signal x_2 is inverted with respect to interferometer signal x_1 . In this model \vec{o} represents a static offset between the rotation axis and the reference frame due to rotation stage misalignment; \vec{s} represents the dynamic radial and axial error movements of the rotation axis, caused by the ball bearing in the rotation stage with $\vec{s}(\varphi) = \vec{s}_s(\varphi) + \vec{s}_a(\varphi)$; where \vec{s}_s represents the synchronous error movements, which occur at integer multiples of the rotation frequency $\vec{s}_s(\varphi + 2\pi) = \vec{s}_s(\varphi)$ and \vec{s}_a represents the asynchronous error movements, which occur at non-integer multiples of the rotation frequency; \vec{w} represents the eccentricity introduced by an offset between the nominal rotation axis and the geometric centre of the SPM c_{SPM} due to a misalignment of the proof mass support on the rotation stage; and \vec{u} represents the position of the SPM's geometric centre c_{SPM} with respect to the reference frame c_{IFO} .

In order to minimize the impact of the (random) asynchronous error movements \vec{s}_a , each measurement with different SPM orientation offset φ_{SPM} is performed over multiple rotations and averaged, leading to $\vec{s}_a \rightarrow 0$. Details concerning the number of rotations for averaging n_{rot} and the mean standard deviation $\bar{\sigma}_{\text{rot}}$ over all rotations with respect to the averaged signal are illustrated in Table 3.3. Considering the noise contributions introduced previously and the

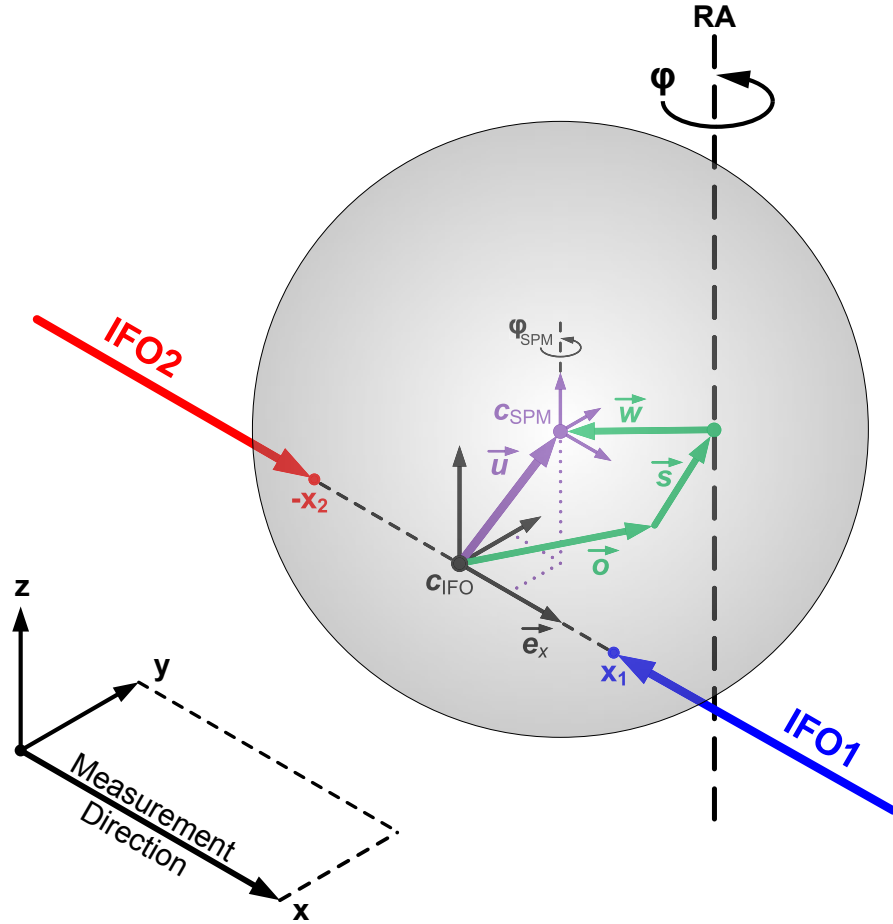


Figure 3.20: Schematic of the mathematical model for correction of noise sources in the recorded measurement data, introduced by misalignment and error movements of the rotation stage. RA: Rotation Axis; c_{IFO} : Reference Coordinate Frame; c_{SPM} : SPM Coordinate Frame (geometric centre); \vec{o} : Offset (between rotation axis and reference frame); \vec{s} : Error Movements of Rotation Stage (radial and axial); \vec{w} : Eccentricity (due to offset between RA and c_{SPM}); \vec{u} : Position of c_{SPM} ; φ : Rotation Angle of Rotation Stage; φ_{SPM} : SPM Orientation Offset; $x_{1,2}$: Interferometer Signals.

φ_{SPM}	n_{Tot}	$\bar{\sigma}_{\text{rot}}$
0	87	1.88 nm
$\pi/3$	99	2.02 nm
$2\pi/3$	96	1.95 nm
π	95	1.93 nm
$4\pi/3$	101	2.00 nm

Table 3.3: Number of rotations n_{Tot} for each measurement with different SPM orientation offset φ_{SPM} including the standard deviation $\bar{\sigma}_{\text{rot}}$ of a single rotation with respect to the average over all rotations.

averaging, the position of the SPM's geometric centre c_{SPM} with respect to the reference frame c_{IFO} can be described by

$$\begin{aligned}\vec{u}(\varphi) &= \vec{o} + \vec{s}(\varphi) + \vec{w}(\varphi) \\ &\approx \vec{o} + \vec{s}_s(\varphi) + w \vec{e}_w(\varphi - \varphi_w)\end{aligned}\quad (3.3)$$

where φ represents the angle of rotation of the rotation stage, φ_w represents the initial angle of the eccentricity \vec{w} (with $w = |\vec{w}|$) and

$$\vec{e}_w(\varphi - \varphi_w) = \begin{pmatrix} \cos(\varphi - \varphi_w) \\ \sin(\varphi - \varphi_w) \\ 0 \end{pmatrix}$$

described in Cartesian coordinates. For a perfect sphere of radius r_{SPM} the interferometer signals x_1 and x_2 are given by the Cartesian equation of a sphere

$$(\pm x_{1,2}(\varphi) \vec{e}_x - \vec{u}(\varphi))^2 = r_{\text{SPM}}^2 \quad (3.4)$$

with the solutions

$$x_{1,2}(\varphi) = r_{\text{SPM}} \sqrt{1 - \frac{u_y^2(\varphi) + u_z^2(\varphi)}{r_{\text{SPM}}^2}} \pm u_x(\varphi). \quad (3.5)$$

Introducing the SPM surface $\hat{\rho}_{\text{SPM}}$ in spherical coordinates into the model with

$$\int_0^\pi \int_0^{2\pi} \hat{\rho}_{\text{SPM}}^2(\varphi, \vartheta) \sin(\vartheta) d\varphi d\vartheta = 4\pi r_{\text{SPM}}^2 \quad (3.6)$$

and $\vartheta = \pi/2$ for all measurement results presented here, Equation 3.5 yields to

$$\begin{aligned}x_{1,2}(\varphi, \varphi_{\text{SPM}}) &\approx \hat{\rho}_{\text{SPM}}\left(\frac{\pi}{2} - \varphi \mp \left(\frac{\pi}{2} + \frac{o_y}{r_{\text{SPM}}}\right) + \varphi_{\text{SPM}}\right) \\ &\quad \cdot \sqrt{1 - \frac{u_y^2(\varphi) + u_z^2(\varphi)}{r_{\text{SPM}}^2}} \pm u_x(\varphi)\end{aligned}\quad (3.7)$$

where φ_{SPM} parametrizes a rotation of the SPM coordinate frame c_{SPM} against the reference coordinate frame c_{IFO} , representing the relative rotation of the SPM enabled by the shaft-hub joint on the proof mass support.

Data Analysis & Results As mentioned above, the interferometer signals $x_{1,2}$ include besides the SPM surface topography also parasitic SPM movements, which are introduced by misalignment and error movements of the rotation stage. Typical interferometer signals recorded over one rotation are shown in Figure 3.21, representing the raw-data before the application of any corrections. Values for the SPM surface topography amplitudes are typically in the order of $\approx 100 \text{ nm}$, whereas values for the offset $|\vec{o}|$ and the eccentricity w are in the order of $\approx 10 \mu\text{m} - 20 \mu\text{m}$ and for the rotation stage error movements $|\vec{s}|$ in the order of $\approx 1 \mu\text{m} - 2 \mu\text{m}$ (the specific error movements of the rotation stage employed, are attached in the Appendix A.3). As a consequence, the parasitic SPM movements have to be removed from the interferometer signals since they represent a dominant source of errors.

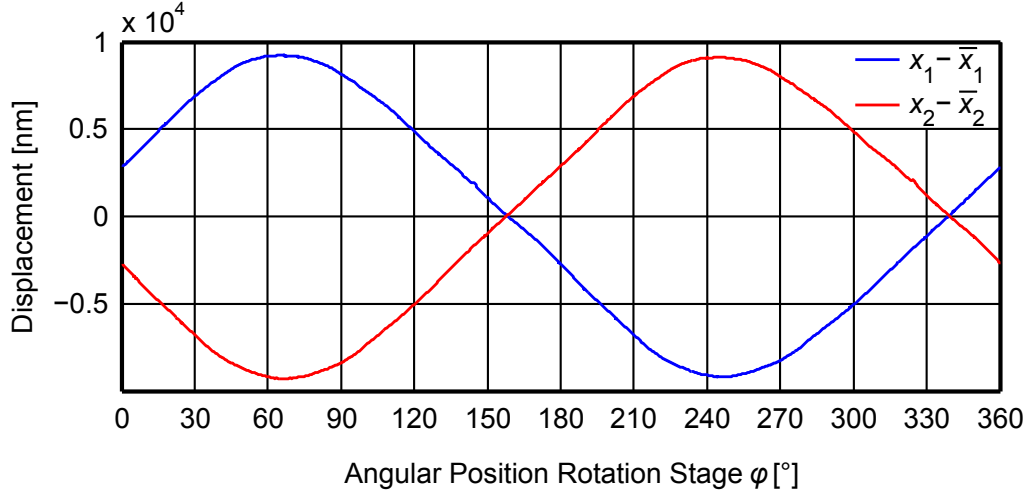


Figure 3.21: Measured interferometer raw-signals $x_{1,2}$ before the application of corrections. Displayed are the data of the measurement with SPM orientation offset $\varphi_{\text{SPM}} = \pi/3$.

By subtracting the mean values from the interferometer signals $x_{1,2}$ the x -offset is removed, leading to $o_x = 0$. Furthermore, the y -offset o_y and the eccentricity w can be estimated via the scalar product

$$\xi_{1,2}(\varphi) = \langle e^{i\varphi} | x_{1,2}(\varphi) \rangle. \quad (3.8)$$

When ignoring the rotation stage error movements with $\vec{s} = 0$ and using a Taylor expansion of Equation 3.5 this scalar product yields to

$$\xi_{1,2} = \pm \frac{w}{2} e^{i\left(-\varphi_w \pm \frac{o_y}{r_{\text{SPM}}}\right)} + w \mathcal{O}\left(\frac{o_y}{r_{\text{SPM}}}\right)^2, \quad (3.9)$$

where

$$w \approx |\xi_1| + |\xi_2| \quad (3.10)$$

$$\varphi_w \approx -\arg(\xi_1 - \xi_2) \quad (3.11)$$

$$o_y \approx \frac{r_{\text{SPM}}}{2} \left(\arg(\xi_1) - \arg(-\xi_2) \right). \quad (3.12)$$

These formulas are used to correct the interferometer signals $x_{1,2}$ for the eccentricity \vec{w} , which is introduced by an offset between the rotation axis and the geometric centre of the SPM c_{SPM} due to a misalignment of the proof mass support with respect to the rotation axis of the rotation stage. More specifically the correction is applied for x - and y -errors, where the latter cause an apparent change of SPM diameter d_{SPM} , leading to the corrected interferometer signals $x_{1,2}^c$ given by

$$\begin{aligned} x_{1,2}^c(\varphi, \varphi_{\text{SPM}}) &= x_{1,2}(\varphi, \varphi_{\text{SPM}}) \\ &\mp w \cdot \cos(\varphi - \varphi_w) \\ &+ \frac{(o_y + w \cdot \sin(\varphi - \varphi_w))^2}{2r_{\text{SPM}}}. \end{aligned} \quad (3.13)$$

φ_{SPM}	w	φ_w	o_y
0	0.39412 (3) μm	1.17203 (62)	23.32 (123) μm
$\pi/3$	8.75880 (3) μm	1.19016 (1)	- 7.88 (6) μm
$2\pi/3$	15.87013 (3) μm	1.46973 (1)	-12.50 (3) μm
π	20.49546 (3) μm	1.91497 (1)	-10.06 (2) μm
$4\pi/3$	18.48525 (3) μm	2.40042 (1)	-10.31 (3) μm

Table 3.4: Estimated parameters w , φ_w and o_y of the actual measurement configuration for each measurement with different SPM orientation offset φ_{SPM} (uncertainties in brackets).

Typical correction functions for eccentricity \vec{w} are displayed in Figure 3.22 (1st and 2nd plot) and show first order characteristics for x - and y -errors, as expected. Because the shaft-hub joint of the proof mass support is subject to lash, the parameters w and φ_w vary randomly with every change in SPM orientation φ_{SPM} , which means they have to be calculated individually for each measurement run. Their estimated values are shown in Table 3.4 in which the parameter o_y should stay constant. However, due to changes in the beam alignment after the first measurement (with $\varphi_{\text{SPM}} = 0$) o_y changed considerably. However, the realignment was mandatory in order to keep high contrast on the QPDs in the interferometers. Minor changes of o_y between the following measurements can be explained by thermal drifts of the setup, which influence the beam alignment and the SPM position over long time frames.

In the following step, the (synchronous) error movements of the rotation axis \vec{s}_s are identified and corrected for. They are introduced by the rotation stage and its angular contact ball bearing. Error movements in x -direction $s_{s,x}$ are calculated by removing the contributions of the SPM surface topography from the measurement data by relating data with different SPM orientation offset φ_{SPM} . According to Equation 3.7 this leads to

$$x_1^c(\varphi,0) - x_2^c(\varphi,0) + x_1^c(\varphi,\pi) - x_2^c(\varphi,\pi) \approx 4 s_{s,x}(\varphi). \quad (3.14)$$

Effects due to error movements of the rotation stage in y - and z -direction, $s_{s,y}$ and $s_{s,z}$, generate additional apparent changes in SPM diameter 2κ . These can be determined using a Taylor expansion of Equation 3.5 and ignoring contributions in x -direction, which results in

$$\kappa(\varphi) = \frac{s_{s,y}(\varphi) o_y}{r_{\text{SPM}}} + \frac{s_{s,z}(\varphi) o_z}{r_{\text{SPM}}}. \quad (3.15)$$

In order to extract an estimate of κ from the measurement data, a similar approach as in the previous step is applied. By relating data of different SPM orientation offsets φ_{SPM} , the SPM surface topography is isolated

$$\begin{aligned} x_1^c(\varphi,0) + x_2^c(\varphi,0) - \left(x_1^c\left(\varphi - \frac{\pi}{3}, \frac{\pi}{3}\right) + x_2^c\left(\varphi - \frac{\pi}{3}, \frac{\pi}{3}\right) \right) \\ \approx 2 \left(\kappa\left(\varphi - \frac{\pi}{3}\right) - \kappa(\varphi) \right) \\ \approx \int_0^{2\pi} \left(2\delta\left(\tilde{\varphi} - \frac{\pi}{3}\right) - 2\delta(\tilde{\varphi}) \right) \kappa(\varphi - \tilde{\varphi}) d\tilde{\varphi} \end{aligned} \quad (3.16)$$

with the delta-distribution δ .

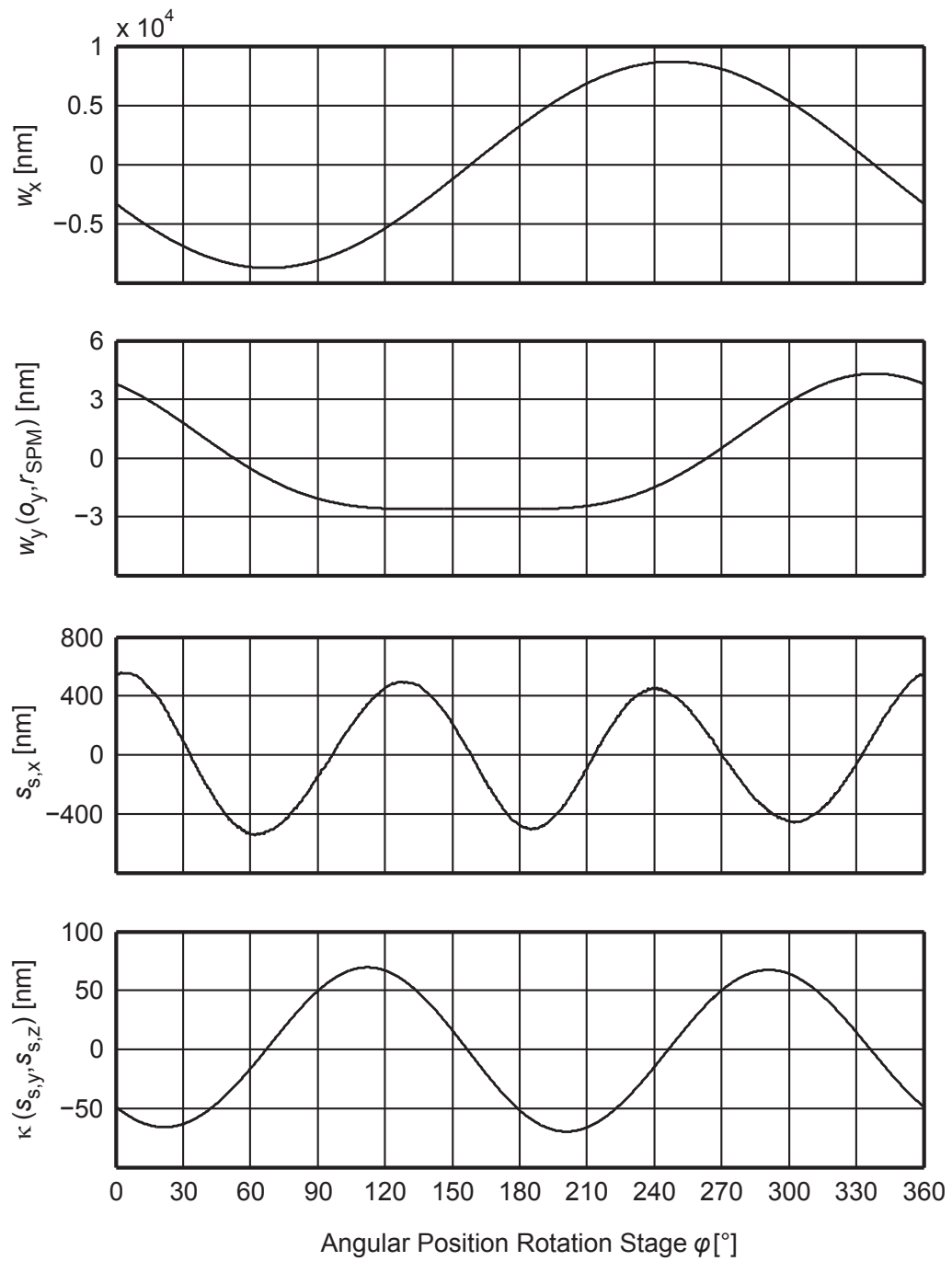


Figure 3.22: Calculated correction functions for eccentricity \vec{w} as well as for the (synchronous) error movements of the rotation axis \vec{s}_s , which are introduced by the rotation stage. Displayed are the curves, which were calculated for the measurement with SPM orientation offset $\varphi_{SPM} = \pi/3$.

Deconvolution with $2\delta(\tilde{\varphi} - \pi/3) - 2\delta(\tilde{\varphi})$ yields an ambiguous shape of κ . This ambiguity can not be resolved without additional information, therefore a solution without high frequency content is used. Typical correction functions for error movements of the rotation axis \vec{s}_s are displayed in Figure 3.22 (3rd and 4th plot) and show third order (x -errors) as well as second order (y - and z -errors) characteristics. Due to the fact that the error movements $s_{s,x}$ and $s_{s,y}$ should have an identical characteristics, it is obvious that $s_{s,z}$ is the dominant error in κ .

On the basis of these correction functions, it is possible to extract the SPM surface topography $\rho_{\text{SPM},1,2}$ from the corrected interferometer signals $x_{1,2}^c$ with

$$\begin{aligned}\rho_{\text{SPM},1,2}(\varphi, \varphi_{\text{SPM}}) &= \hat{\rho}_{\text{SPM},1,2}(\varphi, \varphi_{\text{SPM}}) - r_{\text{SPM}} \\ &\approx x_{1,2}^c(\varphi, \varphi_{\text{SPM}}) \mp s_{s,x}(\varphi) + \kappa(\varphi).\end{aligned}\quad (3.17)$$

The surface topography $\rho_{\text{SPM},1}$, which is calculated from the data of interferometer 1, is displayed in Figure 3.23. Each plot represents one set of measurements with different SPM orientation offset φ_{SPM} . The distinct peak in the results is an attribute of the SPM surface, since it moves with the applied relative rotation φ_{SPM} . However, it is most likely caused by a contamination or damage of the SPM surface. In general the results show topography amplitudes in the order of ≈ 100 nm with peaks at ≈ 150 nm.

Next, all recorded topography signals $\rho_{\text{SPM},1}$ are shifted by the amount of the SPM orientation offset employed for a direct (visual) comparison as well as an averaging of the data, which leads to the averaged SPM surface topography $\bar{\rho}_{\text{SPM},1}$. The result is displayed in Figure 3.24 (top) and shows an excellent agreement between the different measurements. In order to quantify the measurement accuracy and reproducibility, the standard deviation σ_r is calculated based on the deviation ϵ_r from the averaged topography signal. It shows values in the range of ≈ 7 nm – 18 nm (bottom). However, the shape of the deviation shows, that there are systematic errors remaining in the corrected signals. These errors are most likely introduced by the correction for error movements of the rotation stage $s_{s,x}$, as they feature an identical periodicity. One explanation of this effect could be different temperature levels of the rotation stage between the different measurements, which alter its error movements. This assumption would imply, that the applied (general) correction function for $s_{s,x}$ introduces these residual errors. A more visual display of the averaged SPM surface topography $\bar{\rho}_{\text{SPM},1}$ is presented in Figure 3.25 in polar coordinates, in which the topography features are scaled by a factor of $\approx 10^4$ (with respect to the nominal SPM radius r_{SPM}) in order to increase their amplitudes to a level to be visible.

Further on, the spectrum of the measured averaged SPM surface topography $\tilde{\rho}_{\text{SPM},1}$ is compared to the theoretical surface spectrum $\tilde{\rho}_M$, which is based on the surface model introduced in Chapter 2 of this thesis (Equation 2.27 and 2.28), see Figure 3.26. The model has been scaled to the new conditions in the setup by accounting for averaging of surface irregularities over the cross-section of a Gaussian laser beam of diameter $d_b = 175$ μm . Based on the measurement data, the values of the variables of the model are determined to be $C_a = 2.1 \cdot 10^{-4}$ μm^3 and $a = 1$. These values are different, compared to the ones determined previously in the measurements of the test mirror surface ($C_a = 4.1 \cdot 10^{-10}$ μm^3 and $a = 2$), discussed in Chapter 2. Thereby, the higher value of C_a implies an increased level of topography amplitudes, while the lower value of a - which is still within the range given by DIN ISO 10110 – 8 - implies a flatter trend of the curve, hence more evenly distributed topography amplitudes over the (spatial) spectrum. This result is not unexpected, since the SPM dummy employed was never manufactured and finished to an optical quality. Nor was

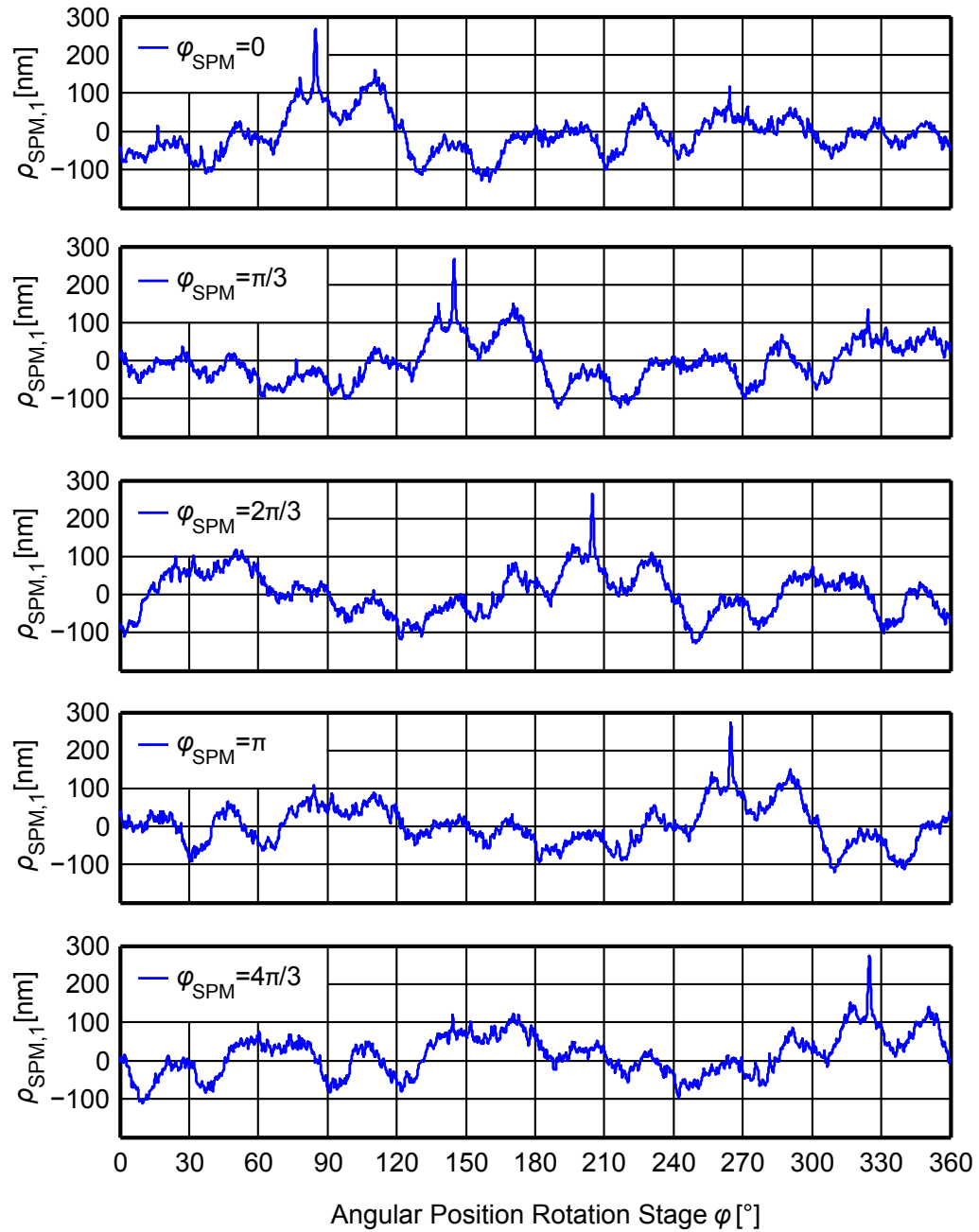


Figure 3.23: SPM surface topography $\rho_{\text{SPM},1}$ as measured for all SPM orientation offsets φ_{SPM} . The distinct peak is a feature of the SPM surface, since it moves with the applied SPM orientation offset, and is most likely caused by a contamination or damage of the SPM surface.

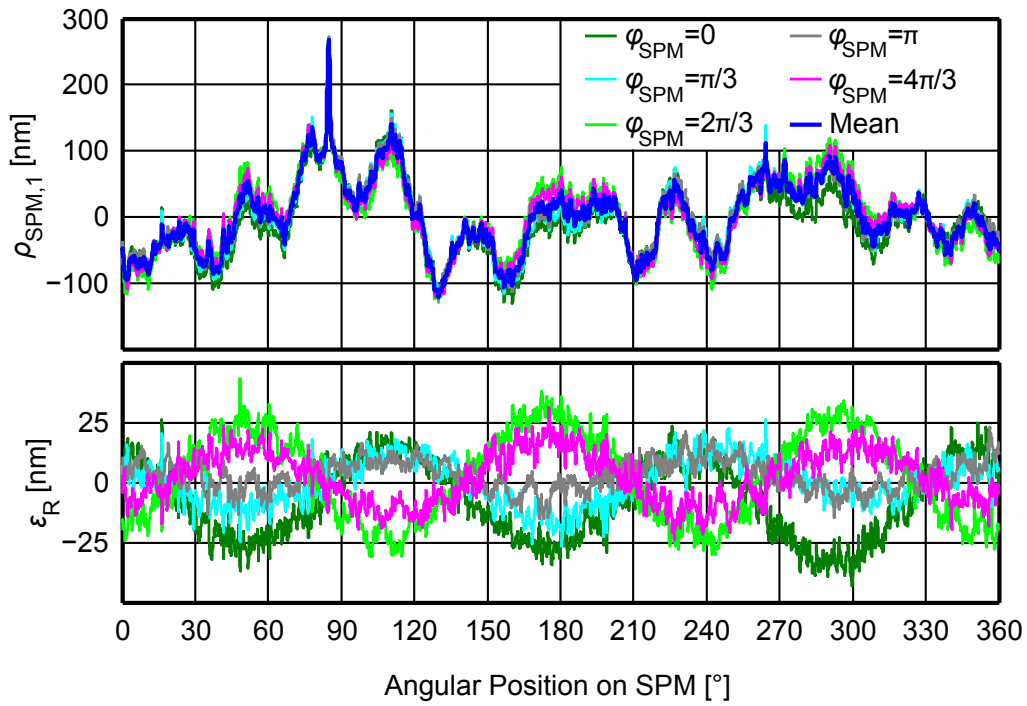


Figure 3.24: SPM surface topography $\rho_{\text{SPM},1}$ (measured by interferometer 1) as measured for all SPM orientation offsets φ_{SPM} (top). The measurement accuracy and reproducibility is quantified by the standard deviation σ_r , based on the deviation ϵ_r from the averaged topography signal $\bar{\rho}_{\text{SPM},1}$ (bottom): $\sigma_{r,0} = 17.3$ nm; $\sigma_{r,\pi/3} = 9.1$ nm; $\sigma_{r,2\pi/3} = 17.9$ nm; $\sigma_{r,\pi} = 7.0$ nm; $\sigma_{r,4\pi/3} = 10.7$ nm;

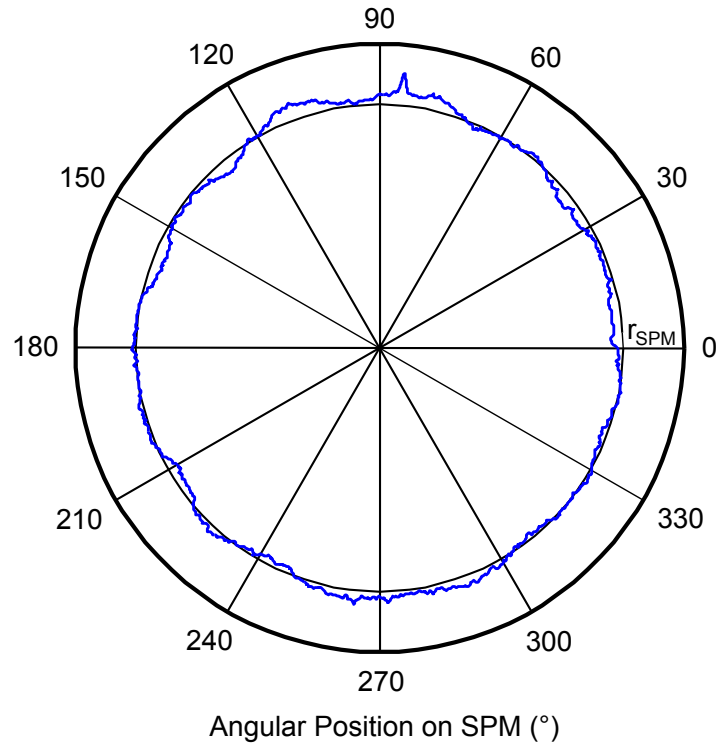


Figure 3.25: Averaged SPM surface topography $\bar{\rho}_{\text{SPM},1}$ in polar coordinates versus the angular position on the SPM. The topography amplitudes are scaled by factor $\approx 10^4$ with respect to the nominal SPM radius r_{SPM} in order to increase visibility.

its handling, storage and transport in compliance with the stringent requirements demanded for an optical component. Both of the mentioned aspects can explain the higher topography amplitude levels and different distribution.

As discussed previously, it is not possible to extract a bespoke correction function for the error movements of the rotation stage $s_{s,x}$ based on the recorded data, which fits for each measurement and SPM orientation offset applied. However, by calculating the changes in SPM diameter with $\rho_{\text{SPM},1}(\varphi, \varphi_{\text{SPM}}) + \rho_{\text{SPM},2}(\varphi, \varphi_{\text{SPM}})$ all occurring error movements in x -direction (measurement direction) are directly compensated for, due to the opposed interferometer configuration. These sum signals are depicted in Figure 3.27 and repeat themselves after $\varphi \approx 180^\circ$, as expected. The values in standard deviation σ_d are in the range of $\approx 5 \text{ nm} - 8 \text{ nm}$, thus considerably smaller than the previous standard deviation values σ_T ($\approx 7 \text{ nm} - 18 \text{ nm}$) from the surface topography signals $\rho_{\text{SPM},1}$. This fact consolidates the assumption that the residual errors in the measured surface topography are indeed introduced by one of the applied correction functions. Unfortunately, the signals of the change in SPM diameter lack the information to distinguish the individual signal contributions of each interferometer involved, which prevents a determination of the actual SPM surface topography from them. Nonetheless, these improved results lead to a new idea for an improved measurement configuration, more specifically a more advanced solution for the reference mirrors, which is expected to help generating more accurate measurement results, see Chapter 4.

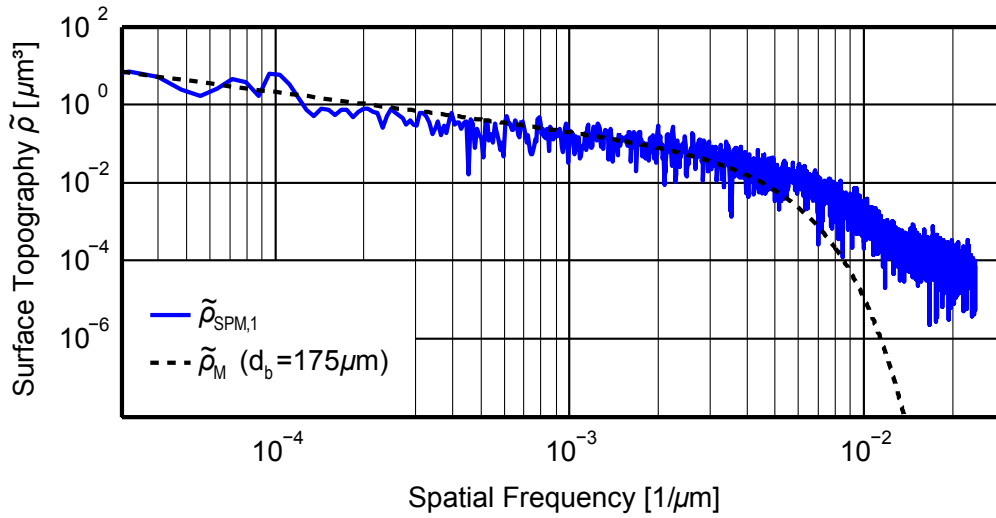


Figure 3.26: Spectrum of the (measured) averaged SPM surface topography $\tilde{\rho}_{SPM,1}$. It is compared to the theoretical surface spectrum $\tilde{\rho}_M$, which accounts for the topography averaging of a Gaussian laser beam of diameter $d_b = 175 \mu\text{m}$, as utilised in the experimental setup.

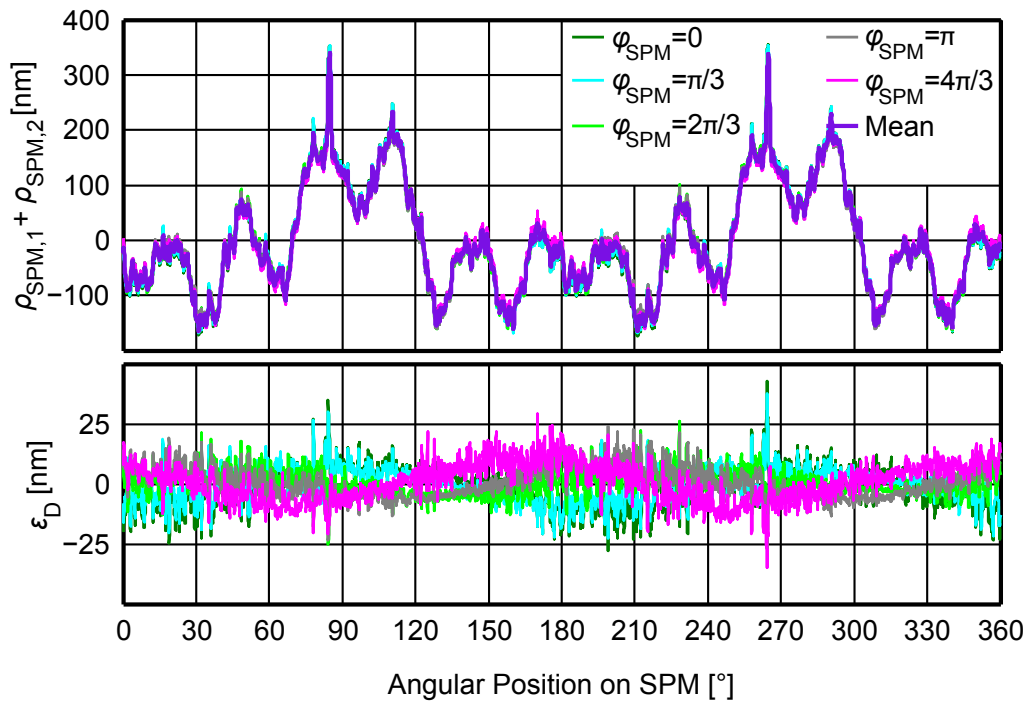


Figure 3.27: Sum of the measured SPM surface topography $\rho_{SPM,1} + \rho_{SPM,2}$ of both interferometers and all performed measurements with different SPM orientation offsets φ_{SPM} , representing the change in SPM diameter (top). The measurement accuracy and reproducibility is quantified by the standard deviation σ_d , based on the deviation ϵ_d from the averaged signal of the change in SPM diameter: $\sigma_{d,0} = 7.9 \text{ nm}$; $\sigma_{d,\pi/3} = 6.5 \text{ nm}$; $\sigma_{d,2\pi/3} = 5.3 \text{ nm}$; $\sigma_{d,\pi} = 6.2 \text{ nm}$; $\sigma_{d,4\pi/3} = 7.8 \text{ nm}$;

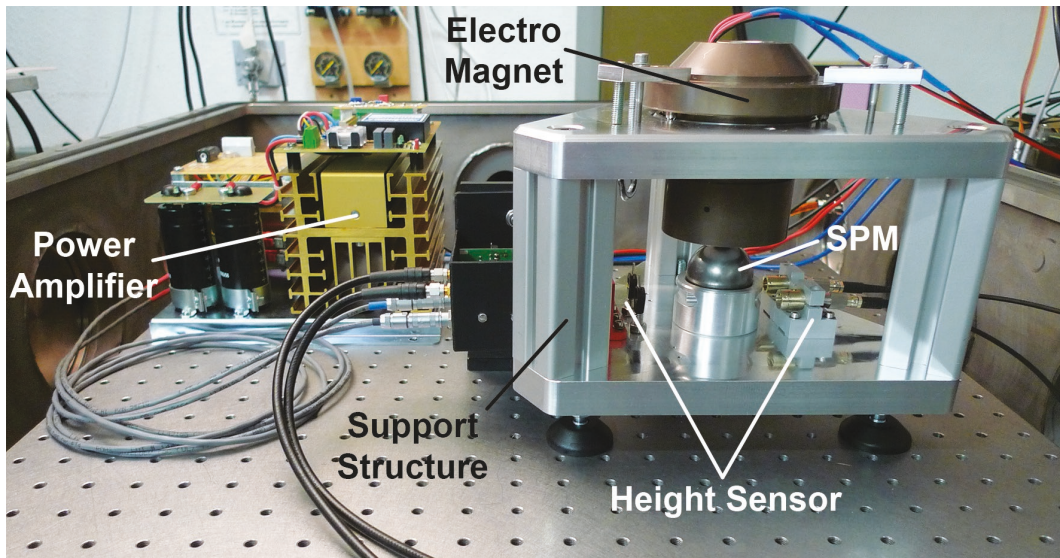


Figure 3.28: Photograph of the SPM levitation test setup for proof of principle of the levitation concept, which utilises an electro-magnet in combination with a height control loop.

3.2 The Proof Mass Levitation System

In order to further investigate the concept of an inertial sensor with SPM, a levitation system has been developed, which features an electro-magnet for levitating a magnetic SPM dummy. Herein, a height control of the SPM is realised by a photo-electric height sensor, coupled to a digital control loop. It is intended to combine this levitation system with the setup for optical SPM surface topography measurements presented previously, including its two heterodyne interferometers for the optical read-out of the levitated SPM. This will result in a comprehensive test bed, which offers the opportunity to perform fundamental and advanced tests as well as parameter studies on this novel concept like:

- Investigations in possible (optical) read-out concepts and configurations of a floating SPM via interferometry.
- Detailed tests on the two different concepts for compensating topography induced errors in the SPM CoM position determination involving a freely rotating SPM / a SPM with defined spin.
- Tests of different contact-free SPM discharge concepts involving UV-LEDs.

3.2.1 Levitation Test Setup

As a first step, a test setup was developed, which utilises an electro-magnet for levitating a magnetic SPM dummy in combination with a photo-electric height sensor for height control. This setup is used for proof of principle as well as to test and improve the components and software involved, in order to increase the performance in height stability of the floating SPM. Figure 3.28 shows the levitation test setup in its final version, which proved to be able to lift and levitate a magnetic SPM dummy.

3.2.1.1 Magnetic SPM Dummy

The SPM dummy employed has a diameter of $d_{SPM} \approx 40$ mm (similar to the sphere employed in the optical SPM surface topography measurements) and is made of μ -metal. μ -metal is a ferromagnetic nickel-iron alloy with high relative permeability, typically in the order of $\approx 50,000$ or more, which is well suited for machining. This material features a density of ≈ 8700 kg/m³, which leads to a weight of the SPM dummy of $m_{SPM} \approx 0.3$ kg. Manufacturing is performed by drop-forging with subsequent grinding and polishing processes in order to achieve a precise shape (max. diameter fluctuations < 1 μ m) as well as a reflective surface. These attributes are required on the one hand to reduce wobbling caused by an uneven mass distribution when performing measurements with a SPM under spin, and to realise an optical read-out via interferometry, respectively. Important to notice is, that the permeability of μ -metal reduces considerably after machining, due to an increased number of lattice defects in its crystal structure. In consequence, the SPM dummy received an annealing process after machining in order to rise its permeability again. For the layout and simulation of the system its relative permeability is (conservatively) estimated to be $\mu_{r,SPM} \approx 1300$.

3.2.1.2 Electro-Magnet

The electro-magnet employed features two-stages, more specifically it features two individual coils of $n_1 = 6000$ (primary coil) and $n_2 = 500$ (secondary coil) turns, which can be used in a cascade configuration if required. The idea is that the primary stage generates high magnetic forces $F_{m,1}$ for basic SPM levitation, while the secondary stage generates small magnetic forces $F_{m,2}$ for fine adjustments of the SPM height. Due to the use of identical 16 bit digital-to-analog converters (DACs) in the controller outputs, the magnetic force $F_{m,1}$ is subject to larger incremental steps compared to the magnetic force $F_{m,2}$, which suits this specific application. Driving current is generated by two linear power operational amplifiers, one for each stage, which are wired to work as a voltage-to-current converter, delivering up to 0.5 A constant current when applying an input voltage of 10 V.

The electro-magnet is displayed in Figure 3.29. All components have been designed in accordance to the available space in the setup for SPM surface topography measurements. Special attention has been given to a vacuum compatible and modular design. Both coils are placed on a common carrier with the secondary coil wound first and the primary coil wound second (above it). A first estimation of the required dimensions and attributes of the primary coil is conducted by a simplified model for calculating the magnetic forces of an electro-magnet. The total energy of the magnetic field U_m of a live inductor is given by

$$U_m = \frac{1}{2} i^2 L \quad (3.18)$$

when neglecting losses. Herein i represents the current running through the coil and L represents its inductance, which is given by

$$L = \frac{n^2}{R_m} \quad (3.19)$$

for a cylindrical coil, with n representing the number of turns and R_m representing the magnetic reluctance of the system. Since the reluctance is dominated by the gap between the magnet

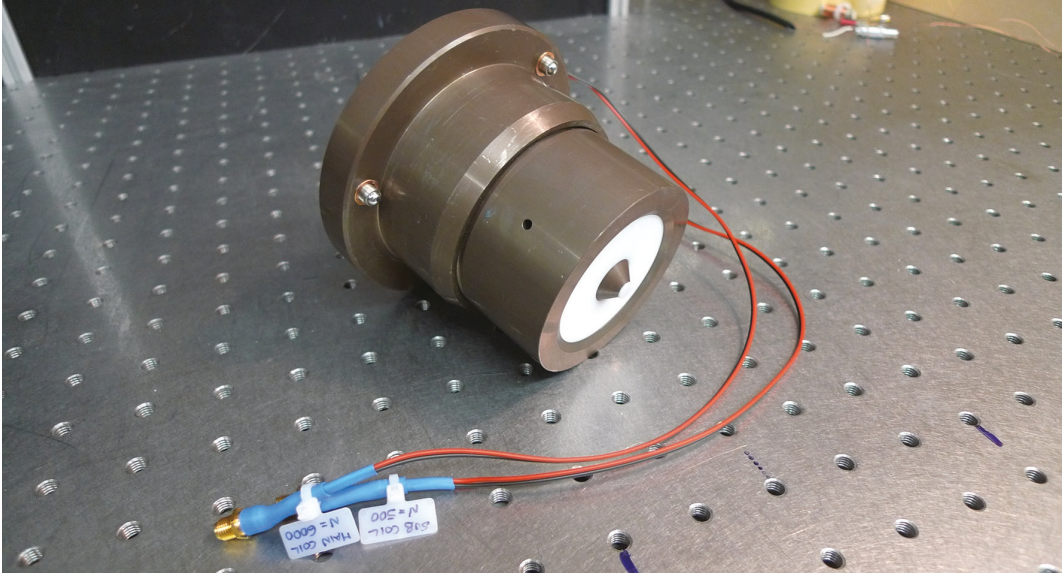


Figure 3.29: Photograph of the electro-magnet for levitation of a SPM, featuring two individual coils for the generation of different levels of levitation forces.

and the SPM surface, at least in the case of the presented system, R_m can be simplified to

$$R_m \approx \frac{l_g}{\mu_0 a_g} \quad (3.20)$$

solely representing the gap reluctance with the gap width l_g , the overlapping area between the magnetic flux and the SPM surface a_g (also called the flux cross-section), and the permeability of vacuum $\mu_0 = 4\pi \cdot 10^{-7}$ H/m, since the setup including the electro-magnet will finally be placed in a vacuum chamber).

For a first estimation of the primary coil dimensions, more specifically the required number of turns of the primary coil, only the levitating force (in z -direction) is considered, leading to the simplified formula of the magnetic force $F_{m,1}$ described by

$$\begin{aligned} F_{m,1} &\approx \left| \frac{\partial U_m}{\partial l_g} \right| \\ &\approx \frac{n_1^2 i_1^2 \mu_0 a_g}{2 l_g^2}. \end{aligned} \quad (3.21)$$

This simplification includes the assumption that axial and radial forces of the magnet are independent with respect to each other. A schematic of the model applied is depicted in Figure 3.30. Considering the gravitational force of the SPM dummy of $F_w \approx -3$ N and the fact that an additional levitation force F_a is required in order to accelerate the SPM dummy in earth's gravity field, a levitation force of $F_{m,1} = -F_w - F_a = 6$ N is selected. The initial (starting) position of the SPM dummy will result in a gap width of $l_g \approx 4$ mm from which the SPM has to be lifted off at the maximum supply current of $i_{1,\max} = 0.5$ A. According to Equation 3.21 this leads to a required number of turns of the primary coil of $n_1 \geq 5500$, when considering a circular flux cross-section of $a_g \approx 20$ mm² on which the magnetic force is

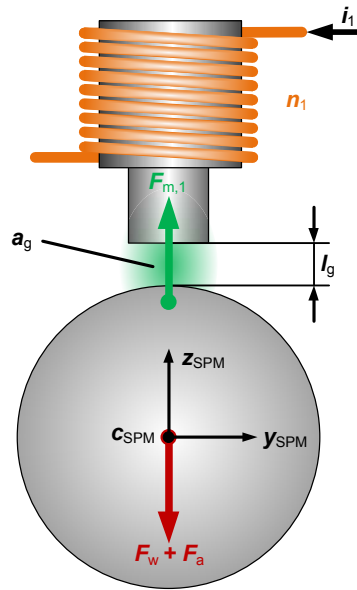


Figure 3.30: Schematic of the magnet's primary stage for estimating its dimensions and attributes. $F_{m,1}$: Levitation Force (in axis); $F_w + F_a$: Gravitational and Acceleration Force of the SPM; i_1 : Supply Current; n_1 : Number of Turns (of primary coil); l_g : Gap Width (between magnet core and SPM surface); a_g : Flux Cross-Section (between magnet and SPM surface).

acting (representing a conservative estimation). This result leads to the final decision of using $n_1 = 6000$ turns for the primary coil.

The core of the magnet is made of a high-alloy, ferritic steel with a relative permeability in the order of ≈ 800 . Its diameter and tip-shape is selected on the basis of the results of a parameter study using the electro-magnetic field simulation software Maxwell (by Ansys). The development goals include the generation of high levitation forces $F_{m,1,2}$, as well as high retaining forces F_r with respect to radial SPM displacements. Especially the latter are required, since they help to stabilise the system during measurements with a SPM under spin and the involved wobbling caused by uneven mass distribution. The parameter study covered different core diameters as well as tip-shapes, including flat-, tapered- and spherical tips. The final core design features a main core diameter of $d_c = 20$ mm with a tapered core tip at 45° and an effective flux cross-section of $a_g \approx 28$ mm², which represents a good compromise between high levitating forces as well as high retaining forces.

The magnet also features a housing made of the same high-alloy, ferritic steel as the core, in order to channel the magnetic flux, hence reducing flux leakage. This increases the levitation force of the magnet considerably, while keeping the core dimension and tip-shape the same. Figure 3.31 shows the calculated levitation force $F_{m,1}$, generated by the primary stage versus the applied current i and gap width l_g . The plotted data is based on the simulation results of the final magnet design, which have been fitted according to Equation 3.21. In principle, the generated magnetic force is sufficient to lift the SPM dummy even at large gap widths, however the results are slightly lower than expected when compared to Equation 3.21. This is attributed to the simplifications applied in the mathematical model, for example no losses in flux leakage.

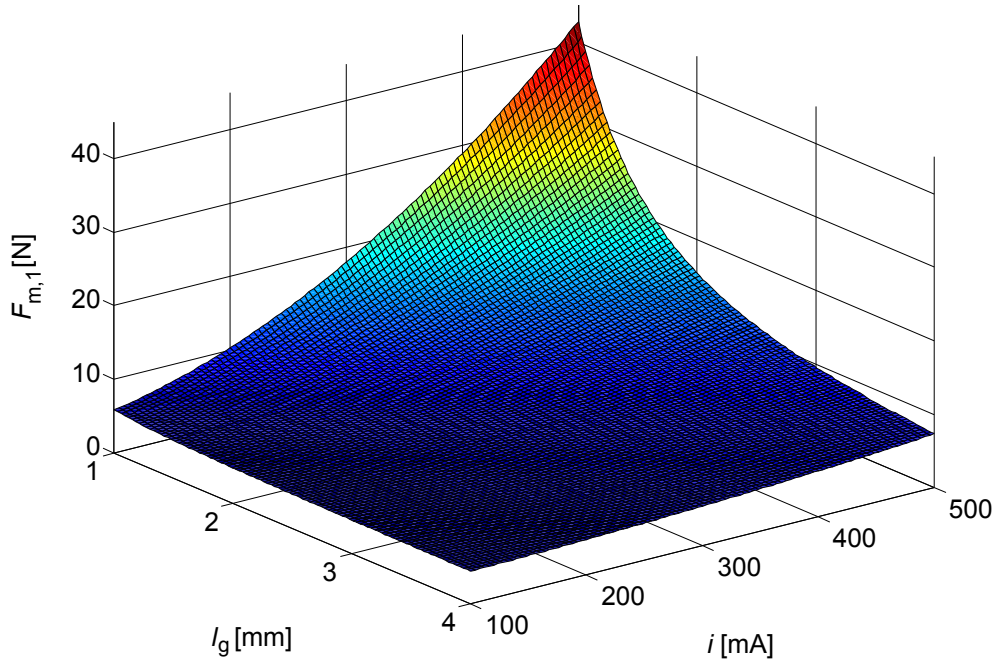


Figure 3.31: Calculated levitation force $F_{m,1}$ of the magnet's primary stage with $n_1 = 6000$ turns, plotted over the applied voltage i and gap width l_g . The data is based on the simulation results of the final magnet design, which have been fitted according to Equation 3.21.

Finally, the electro-magnet was experimentally characterised, in order to determine its properties. In a first step, the generated magnetic flux over the (DC) input voltage of the magnet's operational amplifiers is directly measured via a fluxgate probe, positioned axially centred at a distance of ≈ 2 mm from the magnet's core tip. The results show a linear gain of 372 mT/V for the primary stage and 33 mT/V for the secondary stage, which reflects the ratio of turns in the coils at $n_1 = 6000$ (primary) and $n_2 = 500$ (secondary) rather well.

Subsequently, also the dynamic behaviour of the electro-magnet was characterised, employing the same setup including the fluxgate probe. However this time, the input voltage applied to the operational amplifiers was chosen to be sinusoidal signals with an offset voltage of 6 V and an amplitude of $1 V_{pp}$, applied over a frequency bandwidth between 10^{-1} Hz – 10^2 Hz. Figure 3.32 displays the results in form of a Bode plot. Surprisingly, the edge frequencies of both stages of the electro-magnet are rather similar at ≈ 9 Hz for the primary stage and ≈ 12 Hz for the secondary stage, which also sets the dynamic limit of the SPM height control.

3.2.1.3 Optical SPM Height Sensor

Height sensing of the floating SPM is realised by a two channel photo-electric sensor, which provides the input signals for the height control loop. Figure 3.33 shows a photograph of the sensor, implemented on the support structure of the levitation test setup. Each channel consists of a collimator, which launches a laser beam, an iris diaphragm, which stops stray light and a photo detector (PD) for detecting the transmitted light and converting it into an output voltage. Two channels are arranged in parallel and positioned below the SPM with an offset

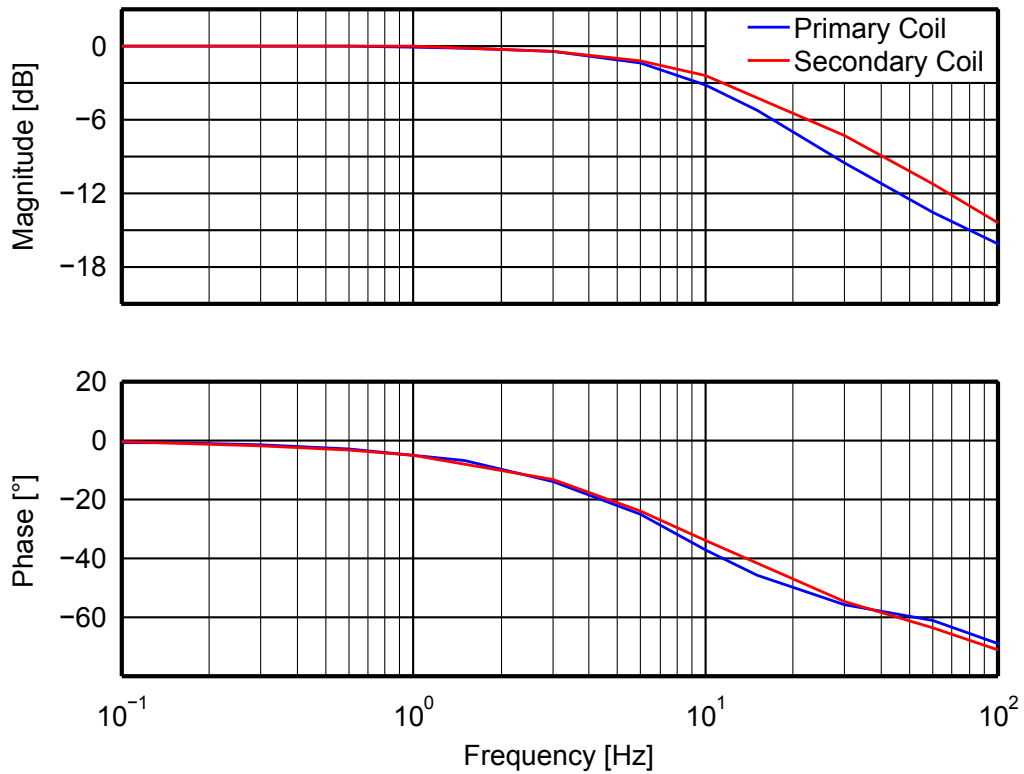


Figure 3.32: Bode plot of the magnetic force of the electro-magnet (for both stages), which represents their dynamic behaviour / response, thus the dynamic limit of the SPM height control.

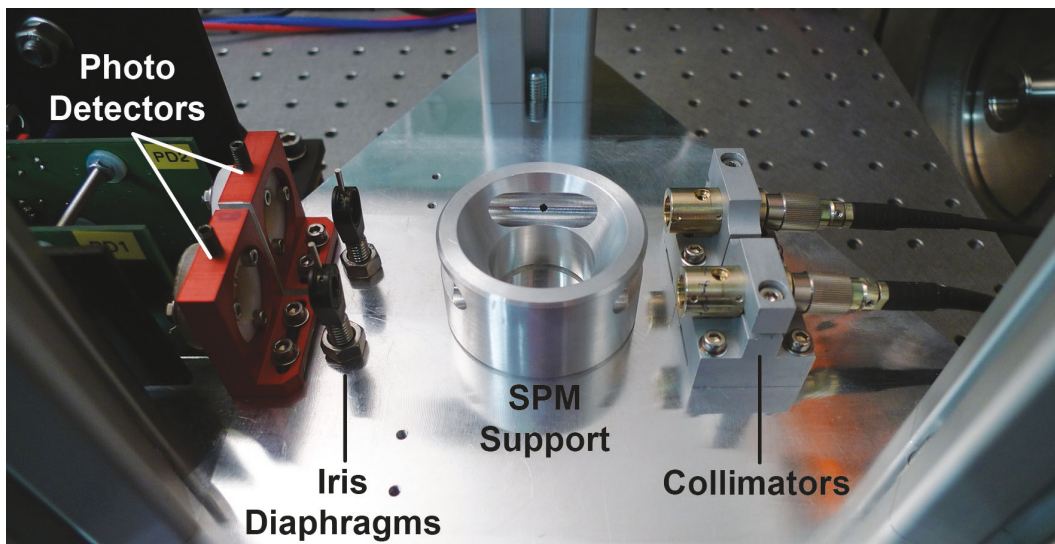


Figure 3.33: Photograph of the photo-electric sensor for SPM height control, featuring two channels in order to compensate for lateral SPM displacements in the combined output signal.

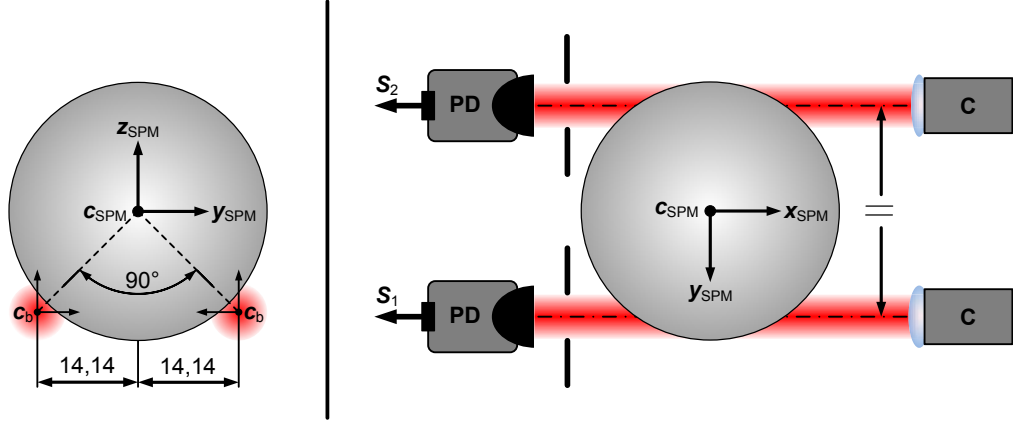


Figure 3.34: Schematic of the height sensor configuration applied, which is used for height control of the (levitated) SPM. C: Collimator; PD: Photo Detector; $S_{1,2}$: PD Output Signals; c_{SPM} : SPM Coordinate Frame (geometrical centre); c_b : Laser Beam Coordinate Frame;

of ≈ 14.14 mm to either side of its geometrical centre, see Figure 3.34. In this configuration, the SPM represents an obstructing element in the laser beams, which varies the level of obstruction, hence the received optical power $P_{b,1,2}$ on the PDs, dependent on the actual SPM position. By measuring the PD output signals $S_{1,2}$, SPM movements in z_{SPM} -direction (height) as well as y_{SPM} -direction (lateral) can be detected. In x_{SPM} -direction, the direction of beam propagation, the sensor shows a very low sensitivity.

This sensor configuration has been selected, since changes in SPM height (z_{SPM}) result in a synchronous variation of the received optical power in both channels ($\Delta P_{b,1} = \Delta P_{b,2}$), while changes in lateral SPM position (y_{SPM}) lead to an opposed variation of the received optical power ($\Delta P_{b,1} \approx -\Delta P_{b,2}$). This means, when looking at the combined PD output signal, lateral SPM movements are directly compensated, leading to a signal only dependent on the SPM height. However, this assumption is only valid for small lateral SPM displacements in the range of $\approx \pm 0.1$ mm and relies on similar parameters of the laser beams involved.

From a mathematical point of view, the PD output signals $S_{1,2}$ can be calculated by multiplying the received optical power $P_{b,1,2}$ with the individual PD conversion factor $C_{PD,1,2}$, which accounts for the conversion from optical power to voltage, therefore considering the photo diodes' responsivity as well as the gain of the subsequent transimpedance amplifier. Figure 3.35 illustrates the mathematical model behind the SPM height calculation, which has been simplified by assuming identical beam parameters for the diameter ($d_{b,1} = d_{b,2} = d_b$), (Gaussian) intensity distribution ($I_{b,1} = I_{b,2} = I_G$) and optical power ($P_{b,1} = P_{b,2} = P_b$). By assuming that the diameter of the photo diode is considerably larger than the laser beam diameter under investigation ($d_{PD} \gg d_b$) the PD output signals can be written as

$$\begin{aligned}
 S_{1,2}(o_{1,2}) &= C_{PD,1,2} \cdot \hat{P}_{b,1,2}(o_{1,2}) \\
 &= C_{PD,1,2} \cdot (P_b - P_{o,1,2}(o_{1,2})) \\
 &= C_{PD,1,2} \cdot \left(P_b - \int_{-3d_b}^{3d_b} \int_{o_{1,2}}^{\infty} I_G(y_b, z_b) dz_b dy_b \right). \quad (3.22)
 \end{aligned}$$

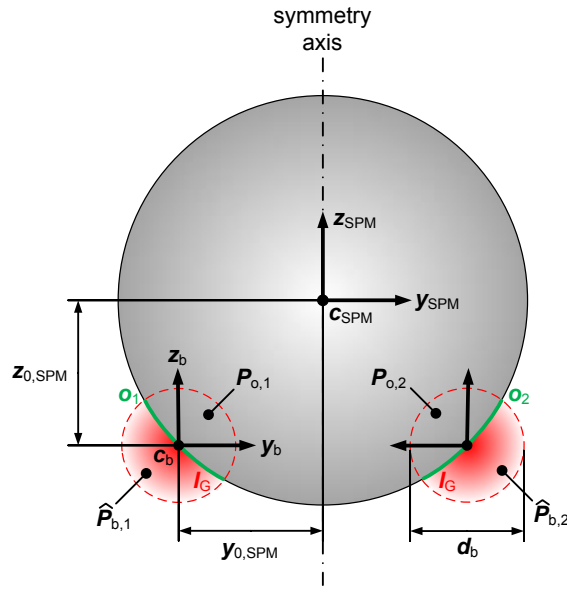


Figure 3.35: Schematic of the model applied, which is used for the SPM height calculation. c_{SPM} : SPM Coordinate Frame (geometrical centre); $y_{0,SPM}/z_{0,SPM}$: SPM Zero Position; c_b : Laser Beam Coordinate Frame; $o_{1,2}$: Integration Limit of Obstruction (depending on the SPM position); $\hat{P}_{b,1,2}$: Transmitted Light Power; $P_{o,1,2}$: Obstructed Light Power; d_b : Laser Beam Diameter (at obstructing position); I_G : (Gaussian) Light Intensity Distribution;

In this mathematical expression, the lower integration limit $o_{1,2}$ for z_b -direction, is defined as

$$o_{1,2}(y_b, y_{SPM}, z_{SPM}) = z_{0,SPM} + z_{SPM} - \sqrt{r_{SPM}^2 - (y_{0,SPM} \pm y_{SPM} - y_b)^2}, \quad (3.23)$$

which is dependent on the SPM position y_{SPM} and z_{SPM} . The integration limits for y_b -direction are chosen at three times the beam diameter ($\pm 3d_b$), since $o_{1,2}$ is only defined within the SPM diameter. Nonetheless, these limits still cover $> 99.9\%$ of the beam profile / light. $y_{0,SPM}$ and $z_{0,SPM}$ represent the zero position of the SPM, which is defined as the position of the SPM coordinate frame c_{SPM} with respect to the laser beam coordinate frame c_b at the position where the SPM main diameter touches the beam centres. Due to the symmetry of the sensor configuration, the PD output signals $S_{1,2}$ only differ by the sign of the lateral SPM position y_{SPM} .

Subsequently, the PD output signals are normalised by multiplying them with the reciprocal of the corresponding PD conversion factor $1/C_{PD,1,2}$ and the reciprocal of the total optical power of the laser beams $1/P_b$ leading to

$$\begin{aligned} S_{n,1,2}(o_{1,2}) &= \frac{1}{C_{PD,1,2} P_b} \cdot S_{1,2}(o_{1,2}) \\ &= 1 - \frac{1}{P_b} \int_{-3d_b}^{3d_b} \int_{o_{1,2}}^{\infty} I_G(y_b, z_b) dz_b dy_b. \end{aligned} \quad (3.24)$$

When including the Gaussian intensity distribution I_G , which has already been introduced

in Chapter 2, Equation 2.20, the normalised signals yield to

$$S_{n,1,2}(o_{1,2}) = 1 - \frac{1}{P_b} \int_{-3d_b}^{3d_b} \int_{o_{1,2}}^{\infty} I_{G,\max} \frac{d_{b,0}}{d_b} \cdot e^{-8\left(\frac{y_b^2 + z_b^2}{d_b^2}\right)} dz_b dy_b. \quad (3.25)$$

Since this integral can not be solved easily in an analytical way, a fit is introduced in order to approximate this function resulting in

$$S_{n,1,2}(y_{SPM}, z_{SPM}) \approx \frac{1}{2} + \frac{\text{erf}}{2} \left(C_1 + C_2(z_{SPM} \pm y_{SPM}) - 2C_3(z_{SPM} \mp y_{SPM}) + C_3(z_{SPM}^2) \right)$$

with the fit parameters $C_1 = 0.002549$, $C_2 = 1.176$ and $C_3 = 0.02088$. The residual rms error of the fitted function is $< 5 \cdot 10^{-5}$, which is smaller than the expected resolution of the 16-bit ADCs in the experimental setup and is therefore negligible.

By adding both normalised signals together, variations due to lateral SPM displacements y_{SPM} almost completely compensate themselves. This assumption can be proven by linearising the signals around $y_{SPM} = 0$, which shows that the lateral SPM position appears with opposite signs. Hence, the combined signal is purely dependent on the SPM height z_{SPM} given by

$$\begin{aligned} S_n(z_{SPM}) &= \frac{S_{n,1}(y_{SPM}, z_{SPM}) + S_{n,2}(y_{SPM}, z_{SPM})}{2} \\ &\approx \frac{1}{2} + \frac{\text{erf}}{2} \left(C_1 + C_2(z_{SPM}) - 2C_3(z_{SPM}) + C_3(z_{SPM}^2) \right). \end{aligned} \quad (3.26)$$

When solving this quadratic equation for the SPM height z_{SPM} , one gets

$$z_{SPM} \approx \frac{-C_2 + 2C_3 + \sqrt{(C_2 - 2C_3)^2 - 4C_3(C_1 - \text{erf}^{-1}(2S_n(z_{SPM}) - 1))}}{2C_3}. \quad (3.27)$$

In the experimental setup, the calculation of the SPM height (z_{SPM}) is implemented on a FPGA board. The PD output signals $S_{1,2}$ are fed into the onboard 16-bit ADCs and digitised at a sampling frequency of $f_{s,3} = 200$ kHz, leading to time-discrete signals dependent on the (index) variable k_3 with $k_3 \in \mathbb{N}$ and $k_3 = t \cdot f_{s,3}$. This sampling rate is chosen considerably higher than the dynamic ability of the magnet, in order to generate oversampling for an improved signal to noise ratio. The logic for the height calculation is implemented on the FPGA board, including the inverse error function erf^{-1} , which is realised via a look up table. Based on the calculated SPM height, the program also determines the SPM velocity \dot{z}_{SPM} by calculating its derivative given by

$$\dot{z}_{SPM}(k_3) = (z_{SPM}(k_3) - z_{SPM}(k_3 - 2)) \cdot \frac{f_{s,3}}{2}. \quad (3.28)$$

Both values are used as the input signal of the controller, which is described in more detail in the next paragraph. The optical height sensor enables SPM height measurements in the range of $z_{SPM} \approx \pm 1.5$ mm. This measurement range is mainly driven by the laser beam diameters utilised, which are given in this application at $d_b \approx 1.7$ mm at the obstructing position. The use of different beam sizes can either lower or increase the measurement range and also influences the sensitivity of the sensor. Important to notice is that the (achievable) precision in SPM height determination at maximum and minimum height is limited, since the

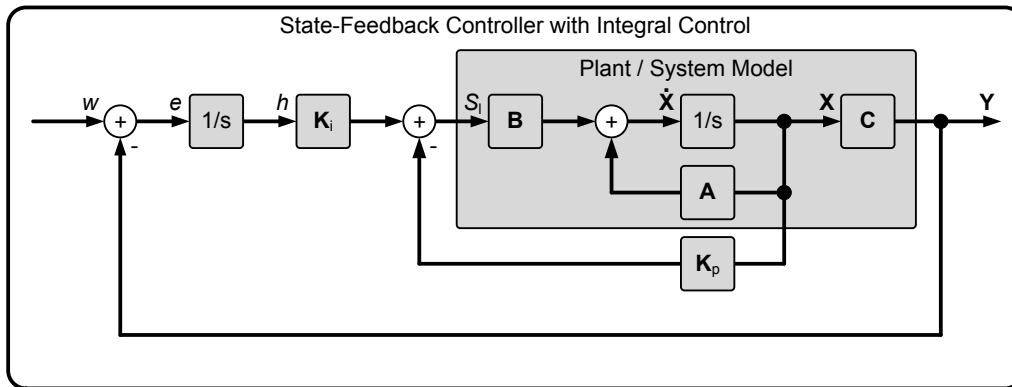


Figure 3.36: Schematic of the system model with a state feedback controller and integral control, as utilised in the levitation test setup. **A:** System Matrix; **B:** Input Matrix; **C:** Output Matrix; **K_p:** Gain Matrix (of proportional part); **K_i:** Gain Matrix (of integral part); w : Set-Point; e : Error (controller input); S_i : Controller Output; X : States (of system model); h : Additional (third) State (in closed loop, due to input integrator); Y : Output (of system model);

detected optical signals are highly non-linear around these positions. This effect is caused by the Gaussian intensity distribution of the laser beams and leads to detrimental errors in SPM height determination, which implies that the system should not be driven near these points. Additional small errors in SPM height determination occur due to the simplifications in the mathematical model as well as the assumption of constant (total) optical powers of the laser beams over time, hence neglecting thermally driven intensity fluctuations. However, these errors are estimated to be small and do not noticeably influence the precision of SPM levitation in the current setup. Especially when considering that in a future application of the system the estimated absolute SPM height value is not longer required. The controller will only need a height dependent signal for stable levitation with $\Delta z_{\text{SPM}} \rightarrow 0$. This signal will be generated based on the DWS signal of the interferometers after the levitation system is combined with the setup for optical SPM surface topography measurements presented previously.

3.2.1.4 Digital Control-Loop

The height control loop varies the current, which flows through the coils of the electro-magnet, in order to control the magnetic forces $F_{m,1}$ and $F_{m,2}$, hence creating a stable condition of SPM levitation with a constant SPM height ($\Delta z_{\text{SPM}} \rightarrow 0$). Input signals are the SPM height z_{SPM} and speed \dot{z}_{SPM} , which are calculated based on the PD output signals of the optical height sensor presented above. The controller itself is implemented on the same FPGA as the program for SPM height calculation and represents a state feedback controller with integral control. Figure 3.36 shows a schematic of the controller employed.

In its implemented form, the controller drives each state of the system into a particular condition, since they are fully controllable and observable, hence stabilising it. In this case the two (measured) signals z_{SPM} and \dot{z}_{SPM} represent the only state variables of the system model. The magnet itself is assumed to follow a static behaviour, thus representing pure gains for both stages, which means an implementation in form of additional states is not required. This simplified approach renders an additional observer obsolete. Steady state errors are reduced by introducing an integrator at the controller input, which integrates the deviation from the

set-point / the error signal e to zero, even when constant or slowly varying disturbances occur. This step introduces an additional third state h . Finally, the controller in closed loop can be described by

$$\begin{pmatrix} \dot{\mathbf{X}} \\ \dot{h} \end{pmatrix} = \left(\left(\begin{pmatrix} \mathbf{A} & 0 \\ 1 & 0 & 0 \end{pmatrix} - \begin{pmatrix} \mathbf{B} \\ 0 & 0 \end{pmatrix} [\mathbf{K}_p \mathbf{K}_i] \right) \begin{pmatrix} \mathbf{X} \\ h \end{pmatrix} + \begin{pmatrix} \mathbf{B}_w \end{pmatrix} w + \begin{pmatrix} 0 \\ -9.81 \\ 0 \end{pmatrix} \right)$$

$$\begin{pmatrix} \mathbf{Y} \end{pmatrix} = \begin{pmatrix} \mathbf{C} & 0 \end{pmatrix} \begin{pmatrix} \mathbf{X} \\ h \end{pmatrix}$$

with

$$\mathbf{A} = \begin{pmatrix} 0 & 1 \\ 0 & 0 \end{pmatrix}; \mathbf{B} = \begin{pmatrix} 0 & 0 \\ K_1 & K_2 \end{pmatrix}; \mathbf{B}_w = \begin{pmatrix} 0 \\ 0 \\ 1 \end{pmatrix}; \mathbf{C} = (1 \ 0); \mathbf{X} = \begin{pmatrix} z_{\text{SPM}} \\ \dot{z}_{\text{SPM}} \end{pmatrix};$$

where \mathbf{A} represents the system matrix describing the system dynamics, \mathbf{B} and \mathbf{B}_w represent the input matrices describing the coupling between the system inputs to states, and \mathbf{C} represents the output matrix describing the coupling between states to system output. \mathbf{K}_p and \mathbf{K}_i represent the gain matrices for the proportional and the integral part of the controller and K_1 and K_2 represent the linear gains of the two stages of the electro-magnet. \mathbf{X} and \mathbf{Y} represent the system model states and output and w represents the set-point. Due to the input integrator the formula is extended to include the additional third state h . In the implemented form the controller is similar to a PID-controller with a proportional, integral and differential (PID) control scheme. This makes it rather robust and enables a stable SPM levitation even in combination with the simplified system model applied.

3.2.2 Measurements & Results

The levitation test setup presented here enables a stable SPM levitation in the range of $z_{\text{SPM}} \approx \pm 1$ mm. As mentioned before, the height signal is highly non-linear above and below that range due to the Gaussian intensity distribution of the laser beams. By recording the (in-loop) output signal of the optical height sensor during SPM levitation, the lower limit of the sensor can be determined. Figure 3.37 displays the recorded (in-loop) height z_{SPM} (top) and its spectrum \tilde{z}_{SPM} (bottom) at a set point of $w = z_{\text{SPM}} = 0$ mm. The results show noise levels in the order of $\approx 10^{-1} \mu\text{m}$ between frequencies of $\approx 10^1 \text{ Hz} - 10^{-2} \text{ Hz}$. At higher frequencies the noise level is decreasing, which is consistent with the dynamic behaviour of the electro-magnet displayed in Figure 3.32. However, since the results represent an in-loop measurement, these values do not reflect the actual SPM height stability of the system, but they represent its lower limit. On the basis of the presented test setup and the positive results, an improved version of the levitation system has been developed. It features an advanced version of the optical height sensor, which will enable also out-of-loop measurements of the SPM height. This advanced setup is described in more detail in Chapter 4 of this thesis.

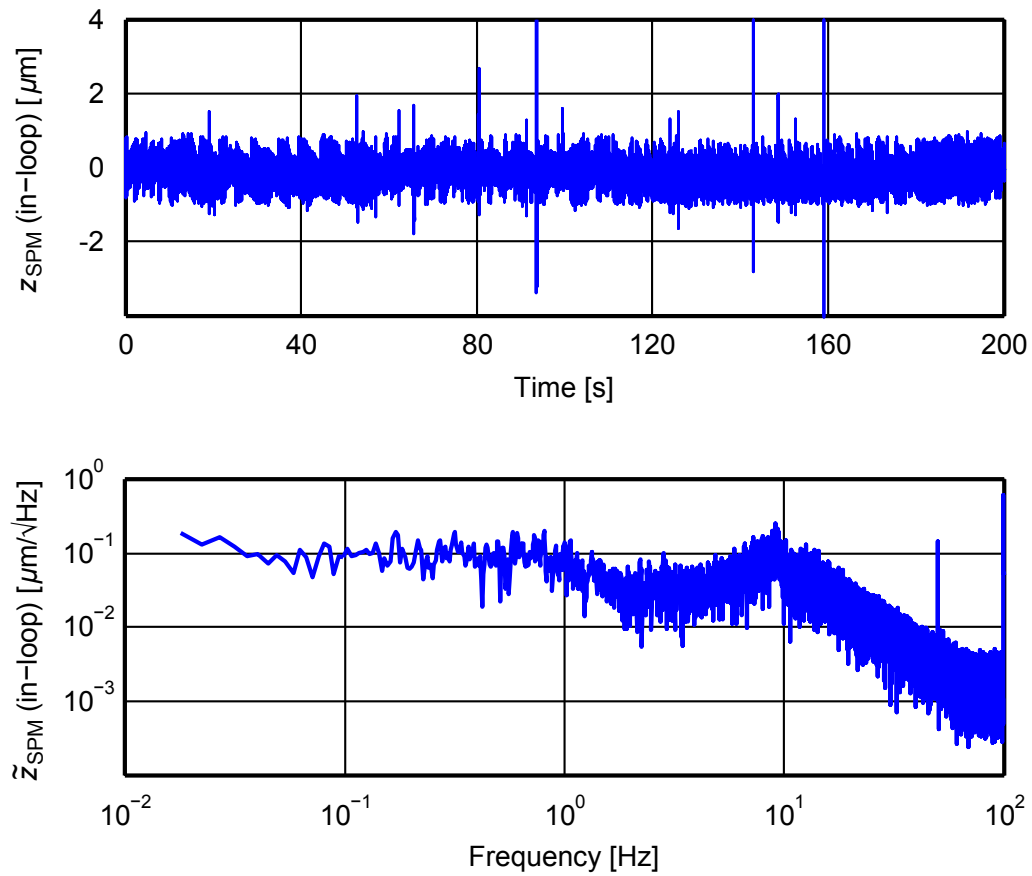


Figure 3.37: Measurement of the (in-loop) output signal of the optical height sensor for a set point of $w = 0$ mm, representing its lower limit. Displayed are the measured height z_{SPM} in the time domain (top) and its spectrum \hat{z}_{SPM} in the frequency domain (bottom).

4 Conclusions & Outlook

Piston in the IFP Telescope In the LISA IFP wide-field telescopes, optical path length changes - so called piston - will be generated by beamwalk of the received / transmitted laser beam over the surface of the telescope mirrors, due to the integrated active beam steering. This topography induced piston has been investigated in more detail in Chapter 2 of this thesis, in order to assess its impact on the LISA measurement performance via a mathematical model.

In a first step, the surface topography of a representative test mirror was experimentally characterised for determining the input parameters of the surface model. The measurement setup features a heterodyne interferometer with picometer sensitivity, which measures the distance to the test mirror surface. A pendulum mechanism provides precise guidance for a lateral movement of the test mirror with respect to the interferometer's laser beams. During actuation of the mechanism, the laser beams scan over the test mirror surface and the interferometer measures the topography induced changes in distance, hence the mirror topography. The setup proved to be fully functional by delivering highly accurate and reproducible measurement results at the sub- μm level. The observed topography amplitudes showed variations in the nanometre scale for the test mirror employed, displayed in Figure 2.20. These variations can be directly transferred into piston by multiplication with a factor of 2 for considering the change in travelled light distance.

Further on, a mathematical model was introduced, which shall predict the piston within the IFP wide-field telescope, generated by beamwalk due to beam steering. This model has been calibrated against the experimental results and checked for consistency, illustrated in Figure 2.22. Afterwards it was applied to the specific conditions in the IFP wide-field telescope, taking into account its geometry and optical design as well as the orbit mechanics of the three spacecraft. Finally the model predicts that piston generated by beamwalk due to IFPM pointing is in fact negligible for the current telescope design, or - in other words - should not significantly impact the LISA measurement sensitivity, see Figure 2.31. These results are attributed to the averaging of the mirror topography over comparatively large beam diameters, which

- considerably reduce the topography amplitudes to levels well below the allocated requirement. (And specifically for Gaussian beams, push the spectral components to very low time frequencies below the LISA measurement bandwidth. This particular effect is attributed to the relatively small lateral beamwalk velocities on the telescope mirrors.)
- reduce the piston gradients such, that coupling of the beams to small amplitude beamwalk jitter also remain well below the allocated requirement.

An additional reduction of the beamwalk induced piston is expected, since the actual LISA telescope mirrors will most probably feature a higher surface quality ($\leq \lambda/20$) compared to the test mirror investigated. However, the presented results do not consider optical path length changes in the telescope due to geometrical coupling of tilt to piston, which is mainly driven by the IFPM design, in particular the kinematics of the hinge. Additional contributions are attributed to manufacturing as well as alignment tolerances with respect to the telescope's

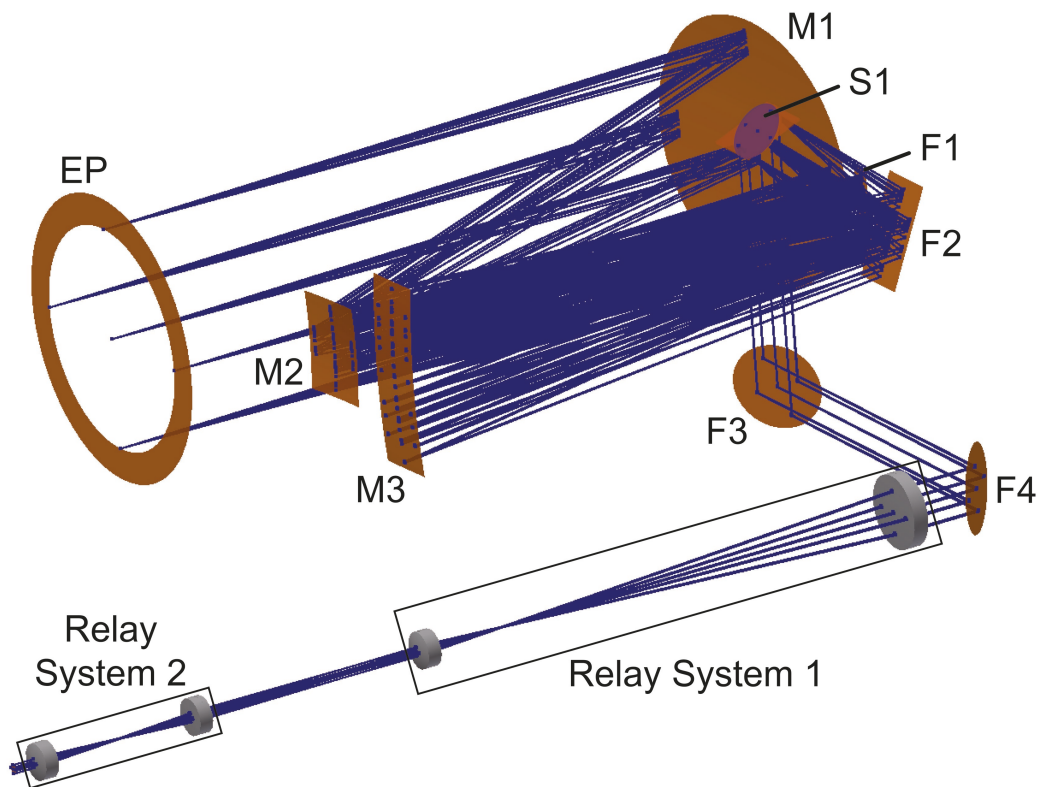


Figure 4.1: Optical design of the off-axis wide-field telescope as employed in the experimental setup for demonstrating the feasibility of the IFP concept. It offers an accessible intermediate pupil for positioning the scanning mirror S1, which is included in the IFPM. The overall field of view of the telescope is $\pm 1^\circ$. EP: External Pupil; M1 - M3: Mirrors with Power; F1 - F4: Flat Folding Mirrors; S1: Flat Scanning Mirror; Relay System 1: Optic for Beam Expansion / Compression; Relay System 2: Optic for Beam Imaging;

intermediate pupil plane and the rotation axis of the IFPM. These errors are expected to generate considerably larger piston effects compared to the beamwalk and have to be analysed in more detail in order to determine their influence in the LISA measurement performance.

In pursuit of this, a new investigation has been started, which includes an experimental setup for measuring the total piston in the IFP wide-field telescope, generated by the integrated beam steering [51]. The results will be used to demonstrate the general feasibility of the IFP concept. The setup employed features a Zerodur based, fully representative laboratory model of the IFP wide-field telescope, including an IFPM prototype for active beam steering. The piston measurements are performed by a heterodyne interferometer with picometer sensitivity, which is also Zerodur based. This setup enables an end-to-end performance validation of the IFP concept, including measurements of the telescope's passive as well as dynamic stability under active beam pointing. Further investigations will address stray light effects and their possible impact in the LISA measurement performance.

Describing the setup in more detail, the telescope employed is a down-scaled version of the IFP wide-field telescope presented in Chapter 2, with an external pupil of $\varnothing 150$ mm. Its optical design is displayed in Figure 4.1 and features two stages with an overall magnification of 25. The first stage features a magnification of 5 and includes 3 mirrors with power (M1 -

M3), which generate an accessible intermediate pupil for the scanning mirror (S1) as well as 4 additional flat folding mirrors (F1 - F4) for beam guidance. The second stage includes two pupil relay systems with a magnification of 5 and 1, the first one for beam expansion/compression and the second one for beam imaging onto the interferometer's QPDs.

The IFPM prototype within the telescope is developed and manufactured by TNO and holds the scanning mirror S1, which can be tilted by $\pm 2.5^\circ$, resulting in an overall field of view of the telescope of $\pm 1.0^\circ$ (considering the magnification of the first stage). The IFPM's structure is based on a monolithic design made of titanium and includes elastic Haberland hinges for the mirror rotation, in combination with a Gimbal mounting concept for the mirror support. This concept minimises tilt to piston coupling during actuation, since the rotation axis should ideally coincide with the mirror surface. The IFPM itself is driven by a custom made piezo stepping actuator, which offers high resolution and range. Thereby the driving force is applied parallel to the surface of the scanning mirror in order to reduce surface distortions.

A rendering of the complete setup is depicted in Figure 4.2. It combines all required components of the setup on one common Zerodur base plate, including the interferometer head, the beam expander/compressor, the telescope mirrors and the end mirror M0, hence providing a thermo-mechanically stable structure. The interferometer head itself features a quasi-monolithic design, in which the optical components are bonded onto a Zerodur base plate via hydroxide catalysis bonding, offering high thermal and mechanical stability. The bonding itself was performed by the University of Glasgow, which has been optimising this particular process for the application with Zerodur [52]. Both, the measurement and reference laser beam are launched in the interferometer head towards the telescope and the reference path, respectively. Thereby the measurement beam enters the telescope from the back and passes both pupil relay systems. Next, it is guided onto the scanning mirror S1 via the two folding mirrors F4 and F3 and deflected in a variable angle set by the IFPM for changing the line of sight of the telescope. Afterwards the measurement beam passes the subsequent telescope mirrors F2, M3, F1, M2, M1 and is finally hitting the end mirror M0, which is located in the telescope's external pupil and simulates the remote spacecraft. At M0 the measurement beam is reflected in itself back through the telescope towards the photo detectors of the interferometer, which measures path length changes due to the active beam steering by the IFPM with respect to the (ideally) constant length of the reference path.

Surface Measurements of a SPM Inertial sensors featuring a fully drag-free SPM in combination with an all optical read-out, promise very low noise levels, hence an increased measurement accuracy, since the proof mass is not controlled or suspended in any DoF. However, without a suspension, the SPM tends to slowly rotate during free fall due to residual torques, which results in surface topography induced path length changes in the optical read-out system and therefore errors in position determination of the SPM's CoG. One solution to address this specific problem is the application of a correction algorithm, which accounts for the topography induced errors via a detailed surface map. This map will be measured prior to launch of the spacecraft and is implemented into the correction algorithm, which will be applied on the recorded in-orbit measurement data [53]. The generation of such a surface map has been experimentally investigated in more detail in the first part of Chapter 3 of this thesis. The measurement setup features two heterodyne interferometers with picometer sensitivity, positioned in an opposed configuration, which measure the distance to the surface of a SPM dummy. This SPM dummy is placed on a precise rotation stage in the middle between the

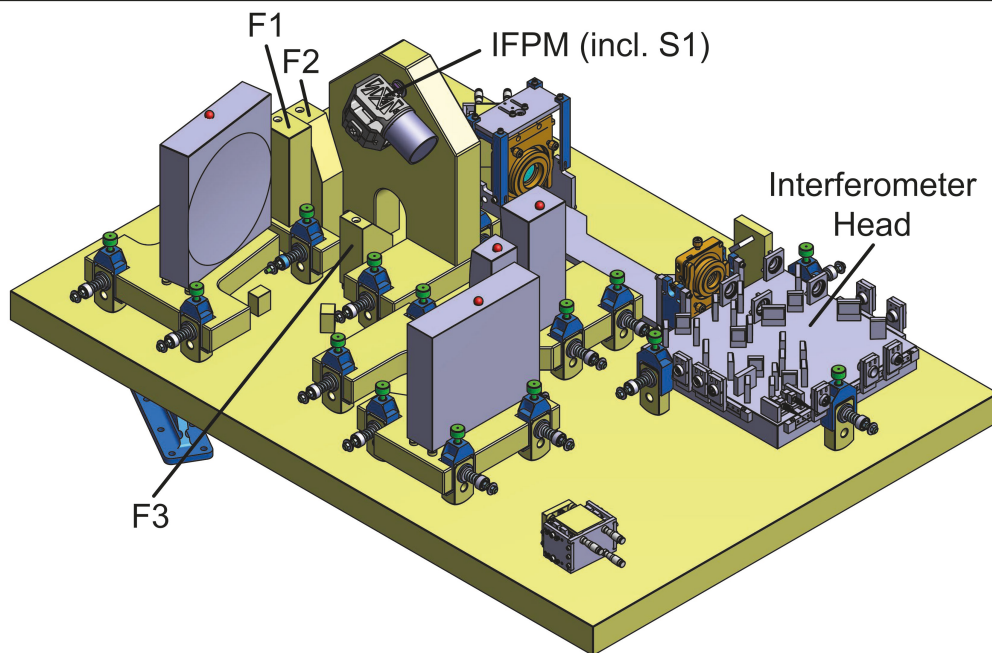
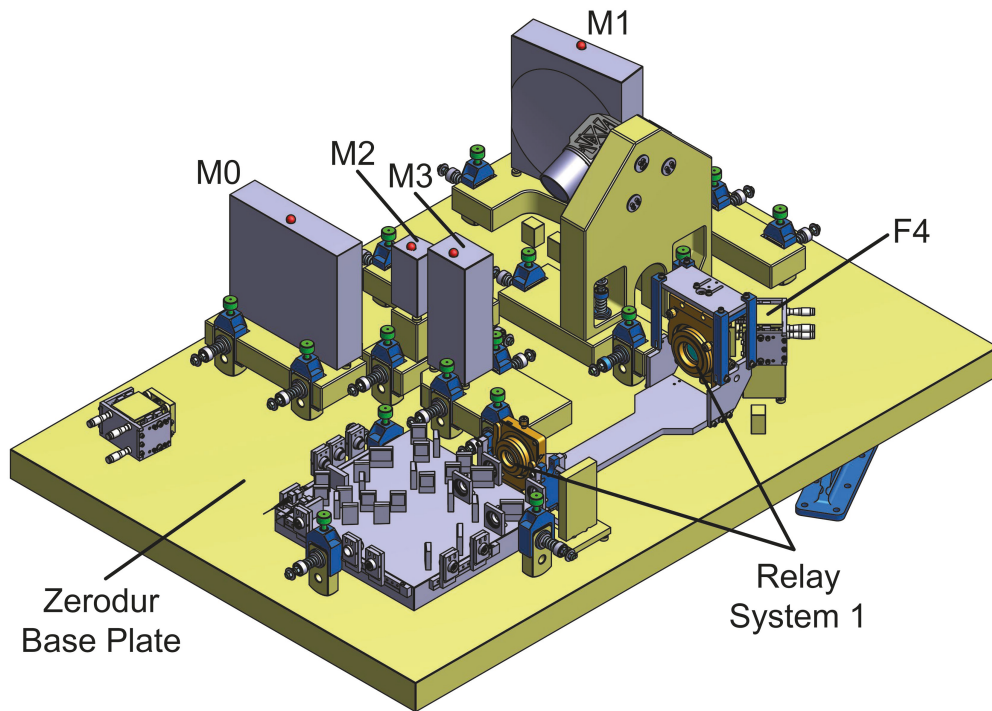


Figure 4.2: Rendering of the experimental setup for demonstrating the feasibility of the IFP concept. All components are mounted onto one common Zerodur base plate. M0: End Mirror (simulating the remote spacecraft); M1 - M3: Mirrors with Power; F1 - F4: Flat Folding Mirrors; IFPM: In-Field Pointing Mechanism (including the scanning mirror S1 for beam steering); Relay System 1: Optic for Beam Expansion / Compression;

two interferometers and is rotated during measurement. Therefore the laser beams scan over the SPM surface and the interferometer measure the topography induced distance changes along a great circle of it.

Further on, a mathematical model has been introduced in the data evaluation process, in order to correct for deterministic errors caused by alignment errors as well as error movements of the rotation stage. The corrected results represent the SPM topography and are depicted in Figure 3.24, featuring measurement accuracies in the range of $\approx 7 \text{ nm} - 18 \text{ nm}$. Thereby the achieved accuracies are limited by the correction process employed and were improved by summing up both interferometer signals, representing the change in SPM diameter rather than the SPM topography itself. By doing this, errors in measurement direction are directly suppressed without the use of the previously introduced correction process (at least in the measurement direction), which leads to the improved results depicted in Figure 3.27, featuring measurement accuracies in the range of $\approx 5 \text{ nm} - 8 \text{ nm}$. These are similar levels of accuracy as achieved in the tactile measurements of the gyroscope spheres of the GP-B space mission, which were performed with a Talyrond machine (by Taylor Hobson). This machine was equipped with a tactile displacement measuring instrument and showed values in the order of $\approx 8 \text{ nm} - 10 \text{ nm}$ [35].

In general these results prove that the measurement setup is fully functional and already generates SPM topography measurements with accuracies at the low nm level. However, in order to generate results suitable for the use in a LISA like GRS, this accuracy has to be further improved, down to the low μm level. The results of the performance measurements of the entire setup, depicted in Figure 3.17, and the interferometers, depicted in Figure 3.10, show that the current setup still has left some potential for improvements in order to increase the measurement accuracy well below the current level. Further improvements could be gained by employing larger beam diameters of the measurement beams as well as by increasing the stability of the thermal environment of the setup, which could be realised by

- implementing multi-layer insulation foil inside the vacuum chamber
- placing of the PD electronics inside the vacuum chamber

hence increasing the thermal stability of the setup over long time frames.

An additional major point to address for future enhancements of the setup is the ability to measure the complete surface of a SPM within one measurement run. Towards this goal, an automated mechanism has been developed, which provides an additional (rotational) DoF to the SPM around a second rotation axis ϑ , orthogonal to the rotation axis of the rotation stage φ . Figure 4.3 shows a photograph of the mechanism, which is made of stainless steel and will be placed on the rotation stage of the setup. It features a driven axis including a driving wheel as well as a freely rotating axis including two (permanently fixed) support wheels. The SPM will be placed onto the three wheels with the contact force only generated by gravity. When the driven axis is rotated by an electric stepping motor, the SPM rotates around its geometric centre and also drives the freely rotating axis. The latter is equipped with a precise optical encoder in order to determine the current rotation angle of the SPM. Friction in the system is minimised by employing ball bearings in both axes in order to reduce slipping and associated errors in determination of the rotation angle. Additionally, slip can be detected by comparing the nominal rotation angle of the driven axis (given by the controller of the stepping motor) with the rotation angle of the freely rotating axis (given by the optical encoder).

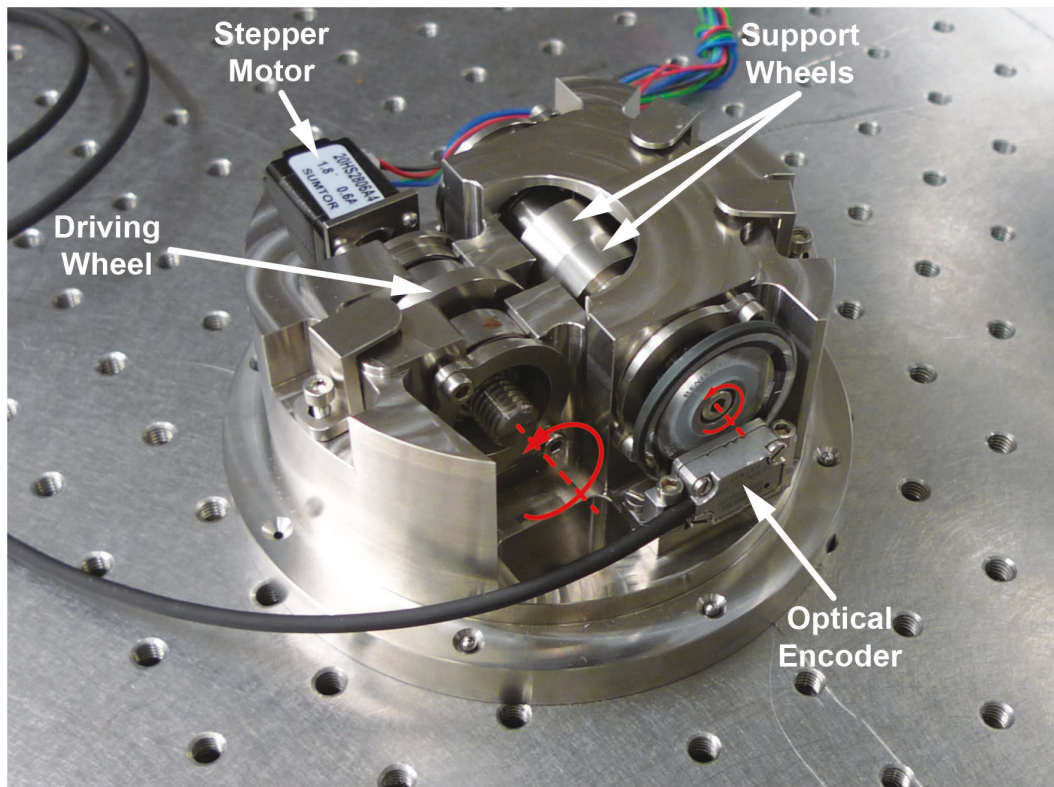


Figure 4.3: Photograph of the new rotation mechanism, which enables the measurement of a complete SPM surface within one measurement run. This mechanism provides a second (rotational) DoF to the SPM by driving the axis / the driving wheel. Not depicted is the reference ring mirror, which will be positioned centrally (surrounding the SPM) and provides a common reference for both interferometers.

An additional feature of this mechanism is its integrated reference ring mirror, which will take over the function of the two fix mounted reference mirrors employed previously in front of the SPM. This reference ring surrounds the SPM and provides a common reference for both interferometers. The advantage of this configuration is the direct coupling of the rotation stage error movements into the length of the reference path. This will lead to a similar positive effect on the measurement accuracy as gained by the calculation of the change in SPM diameter, when summing up both interferometer signals, hence directly compensating for rotation stage error movements in measurement direction. In this configuration however, it will be still possible to calculate the SPM topography from the individual interferometer signal. An additional positive effect of the reference ring mirror is the more direct connection of the reference (in a mechanical point of view) to the SPM, which is expected to further reduce measurement noise.

In order to realise a complete surface map it is also necessary to speed up the data acquisition system of the setup. Such a map requires the measurement of ≈ 800 great circles of the SPM, depending on the requested resolution and laser beam diameters utilised. With a faster acquisition scheme, thermo-elastic drifts of the setup will not be limiting the measurement accuracy. One solution to address this problem is a reduction of the loop time of the interferometer host program to ≈ 1 ms (up by a factor of 50 with respect to the current state). This solution enables the application of higher angular rates of the rotation stage,

while maintaining angular resolution, and can be implemented with only small changes. In the current setup, the host program calculates besides the phase, displacement and heterodyne amplitude signal of each QPD channel also the averaged interferometer displacement and tilt signals $x_{1,2}$ and $\alpha_{1,2}$. In addition several more signals are calculated for monitoring purposes, including the beam position and heterodyne contrast on each QPD. This large amount of signal processing increases the required loop time of the host program and could just as well be calculated during data post processing or in an separate monitoring program, which can run on a different processor core.

In this respect, the use of the reference ring mirror will add an additional advantage, since it also compensates for some of the stochastic, unsynchronous error movements of the rotation stage. As a result, the averaging currently employed over several SPM rotations for minimising noise (≈ 100 rotations per measurement run) could be avoided or at least reduced, which will save valuable measurement time. All together, the suggested changes will reduce the measurement duration for a complete SPM surface map to $\approx 2\text{ h} - 3\text{ h}$, which seems a reasonable time frame to perform accurate measurements.

Levitation of a SPM The development of a levitation system, which enables the levitation of a SPM, allows detailed experimental investigations in possible concepts and configurations of an optical read-out of a floating SPM. Therefore a test bed has been developed, featuring an electro-magnet in combination with a digital height control loop for the levitation. This test stand is presented in more detail in the second part of Chapter 3 of this thesis, and offers a testing environment for the optimisation of the components and systems, in particular the height control loop. In the latest version, this test setup proved to be fully functional by levitating a SPM dummy made of μ -metal with a mass of $\approx 0.3\text{ kg}$ and a diameter of 40 mm . However, the stability of levitation could only be verified based on the available in-loop height signal of the control loop, depicted in Figure 3.37. Measurements of an out-of-loop signal have not been performed due to the lack of an appropriate signal, yet.

Based on this test bed, a new levitation system has been developed, which is specifically designed for the use in the setup for SPM surface topography measurements. Figure 4.4 shows the new design of the system, which will be mounted on the (aluminium) base structure between the two interferometers. Its support structure is equipped with several custom-made translation stages as well as a tip/tilt platform, which together provide full adjustability of the magnet and the optics of the height sensor in all three translational DoFs as well as in tilt. This configuration enables an individual alignment of the system with respect to the interferometers. The electro-magnet employed is directly carried over from the original levitation test bed.

Extensive changes have been made to the optics of the height sensor, which is depicted in Figure 4.5 and schematically in Figure 4.6. It now features 4 optical channels, bundled to two orthogonally arranged beam pairs. This configuration allows for a more accurate position determination of the SPM, since movements in both lateral directions, x_{SPM} as well as y_{SPM} , are detected independently (in contrast to the detection in a single direction as utilised in the original height sensor design). Together with an improved height control, this will increase the positional stability of the floating SPM. The new optics will also enable out-of-loop measurements of the SPM height during levitation by using one beam pair for height control and the second beam pair for height measurement. An additional improvement is the implementation of an intensity detection in each channel. Therefore, the required light is picked up by a 50/50 beam splitter (one in each optical channel, which is placed directly after

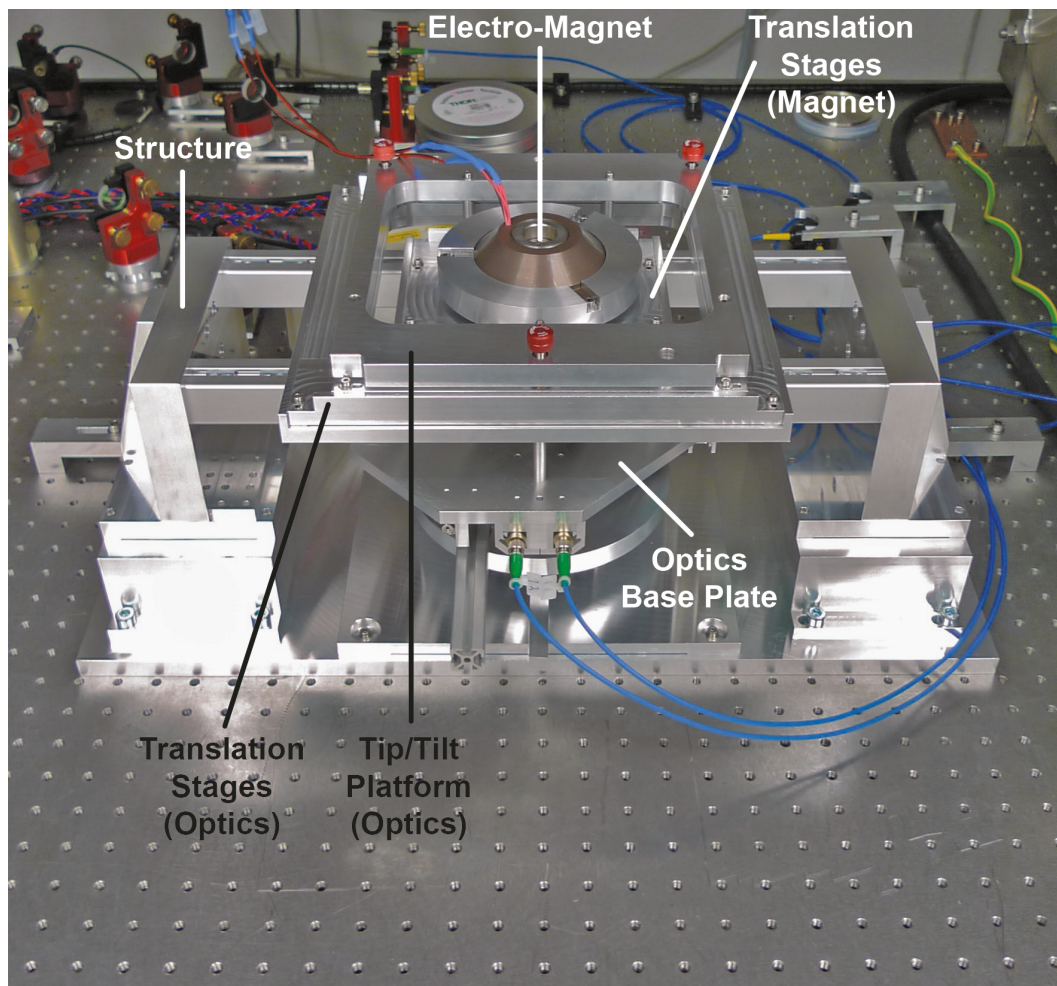


Figure 4.4: Photograph of the new levitation system, which is specifically designed to work in combination with the setup for SPM topography measurements. The translation stages as well as tip/tilt platform enable a full adjustability of the electro-magnet and the optics of the height sensor for alignment with respect to the interferometers.

the individual collimator) and is reflected onto a photo detector. The detector measures the intensity, which is then used for normalisation in order to correct for (mainly thermally driven) intensity fluctuations, hence errors in SPM height determination.

Future developments of the new levitation system should include an extension of the digital control loop in order to support the new 4 channel configuration of the height sensor optics including the data processing for intensity normalisation in each channel as mentioned above. Simultaneously, special attention should be given to the applied control scheme. The use of a cascade control for the two stages of the electro-magnet could possibly be advantageous and should be investigated in more detail. Such a configuration would level out constant force offsets of the secondary coil, hence avoiding saturation.

By combining the new levitation system with the setup for SPM topography measurements, it will be possible to use the heterodyne interferometers for the optical read-out of the levitated SPM. Thus enabling experimental tests on different read-out concepts and configurations, including experimental tests on SPM CoM position determination, based on optical distance

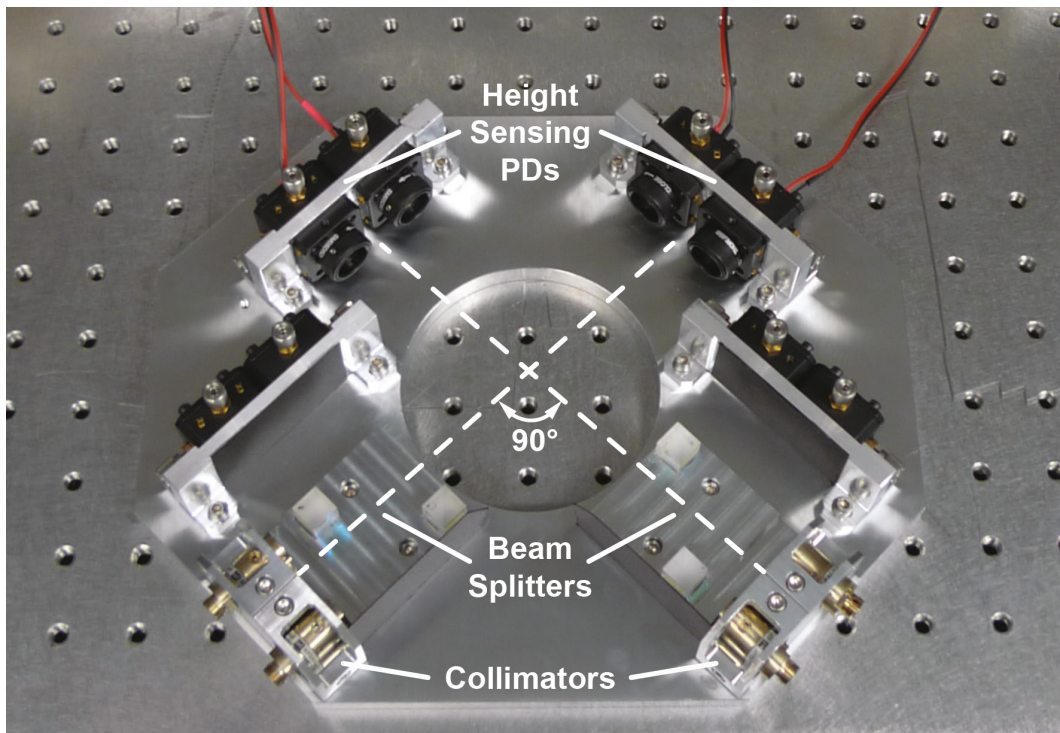


Figure 4.5: Photograph of the improved height sensor optics, featuring 4 optical channels, bundled to two orthogonally arranged beam pairs.

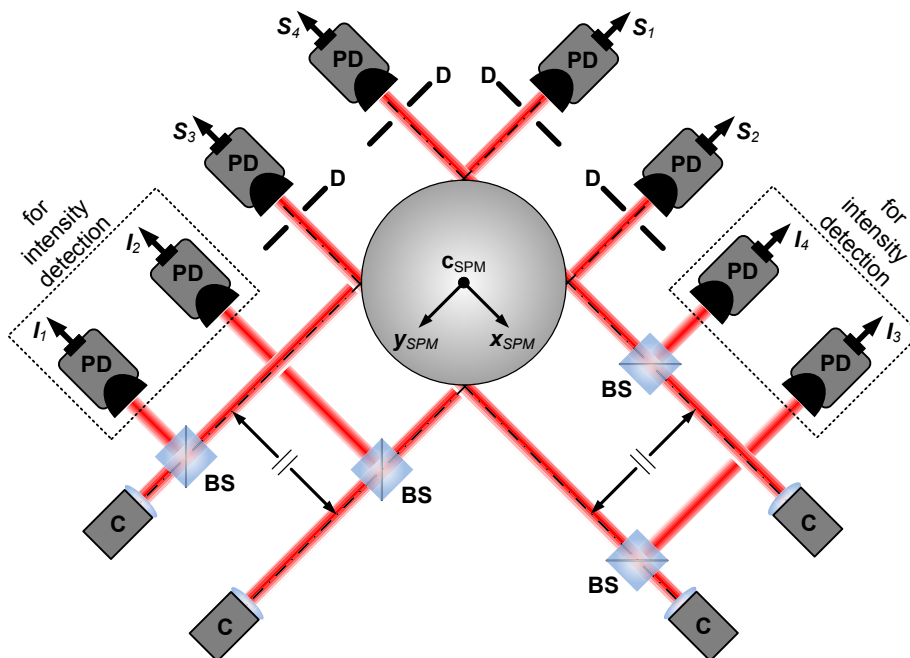


Figure 4.6: Schematic of the improved height sensor optics. This new configuration enables an independent detection of SPM movements in both lateral directions (x_{SPM} and y_{SPM}). C: Collimator; BS: 50/50 Beam Splitter; D: (Iris) Diaphragm; PD: Photo Detector; c_{SPM} : SPM Coordinate Frame (geometrical centre);

measurements. These tests could address both read-out concepts (e.g. utilising a spinning versus a non-spinning SPM), as already described in Chapter 1. One way to apply an active spin onto the SPM is to adopt the principle of an induction motor, in which the SPM acts as the driven rotor. Therefore, the setup has to be equipped with several electro-magnet pairs, positioned in the measurement plane of the interferometers at equidistant angles around the SPM. These magnets are used to generate a rotating magnetic field, which induces eddy currents in the SPM and in turn generate a counter-reacting magnetic field, leading to a momentum causing the SPM to spin.

For tests addressing the read-out concept with a non-spinning SPM in combination with a correction algorithm for compensating surface topography induced errors in SPM CoM position determination, an active spin is only required at the start of the measurements, in order to quickly determine the SPM orientation with respect to the interferometers. The identification of the orientation is enabled by applying the SPM surface map, which is implemented in the correction algorithm and comparing the topography induced distance changes under spin with the topography amplitudes saved in the surface map.

Additionally, investigations in SPM discharge concepts could be performed by introducing small enhancements to the setup. This is an interesting option, since highly precise inertial sensors utilising free-flying proof masses will require a contact-free bipolar discharge system in order to control their variable electric charge level. Otherwise these charges could interact with the surrounding housing and introduce forces, which will act on the proof mass and will lead to residual acceleration noise. Such charges can be generated by contact electrification (during proof mass release) as well as charged particles, high-energy plasma and cosmic rays, which influence the proof mass in orbit. A possible way to realise a contact-free, effective discharge is by employing photo-emission based UV discharge systems, which are already successfully applied in the GB-P gyroscopes [54] and the LTP inertial sensors [55]. Their principle involves the illumination of specific surfaces of the SPM and the dedicated charge-control electrode with UV-light, leading to a release of electrons from their surfaces due to the photoelectric effect. The flow of electrons leads to photo currents, which can either remove positive or negative charges, depending on the applied bias voltage of the injection electrode, thus enabling a bipolar charge control of the SPM. Recently, a conceptual design of an advanced UV discharge system has been elaborated, utilising a high-frequency switching of the UV-light source, which will be synchronised to the applied bias voltage of the injection electrodes at ≈ 100 kHz [56]. The injection electrodes would be already available in the inertial sensor or GRS, since they could be shared with the electrostatic position sensing of the proof mass.

This new discharge concept can be experimentally investigated by equipping the setup for SPM topography measurements, including the levitation system presented, with a fast switchable UV light source (suggested is an UV-LED) in combination with injection electrodes for generating the high-frequency bias voltage. Additionally a pair of (low-frequency) charge electrodes is required, which have to be aligned in measurement direction of the optical read-out of the setup, for generating a defined electric charge in the magnetic SPM dummy. Hence, when an electric charge is applied by the charge electrodes, the levitated SPM dummy will move in measurement direction, and when the discharge process is started, it will move back into its initial position. These movements can be detected and tracked by the optical read-out / the interferometers and used to investigate this new discharge concept in more detail.

Appendix

A.1 Kinematic Trace of the Pendulum Mechanism

This appendix describes the kinematic trace of the test mirror within the pendulum mechanism, which is used in the surface topography measurements of a laser mirror (presented in Chapter 2). During actuation the test mirror follows a circular trace around the pivot point of the flexure hinge, illustrated in Figure A.1. Thereby, the travelled distance l_{TM} of the test mirror centre c_{TM} can be described by

$$l_{\text{TM}}(y_a, y_f) = r_{\text{TM}} \cdot \sin^{-1} \left(\frac{\gamma \left(y_a - 33 + \sqrt{33^2 - (1,5 + (\sqrt{r_f^2 - 44^2} - \sqrt{r_f^2 - (44 - y_f)^2})^2)} \right)}{r_{\text{TM}}} \right).$$

Herein $\gamma = r_{\text{TM}}/r_f$ represents the ratio between the radius of the kinematic trace of the test mirror centre r_{TM} and the radius of the kinematic trace of the point of force application r_f , both with respect to the pivot point of the flexure hinge. y_a represents the position of the piezo actuator and y_f the position of the point of force application. This formula also considers non-linearities in movement, introduced by a tilt of the actuation bar. In order to simplify this expression, a polynomial approximation is introduced, leading to

$$l_{\text{TM}}(y_a) \approx 8.0 \cdot 10^{-5} y_a^3 - 2.8 \cdot 10^{-3} y_a^2 + 1.2 y_a - 4.1 \cdot 10^{-2},$$

which only depends on the actuator position y_a . This simplified equation is the basis for the position conversion in the presented (interferometric) topography measurements. However, this accurate approach is only required for measurements featuring small laser beam diameters ($d_b < 100 \mu\text{m}$). In this specific case, the positional errors introduced by a tilt of the actuation bar - in the order of a few μm - are not negligible due to the comparatively small averaging of the surface topography over the beam cross-section. On the other hand, for measurements featuring large laser beam diameters ($d_b \geq 100 \mu\text{m}$), the conversion can be reduced to $l_{\text{TM}}(y_a) \approx \gamma \cdot y_a$.

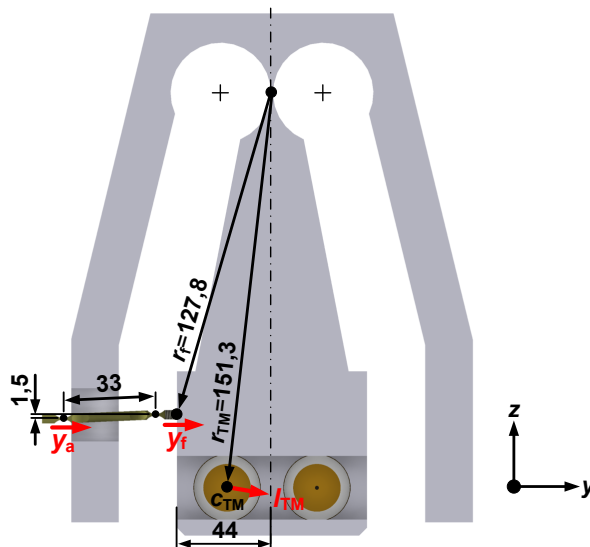
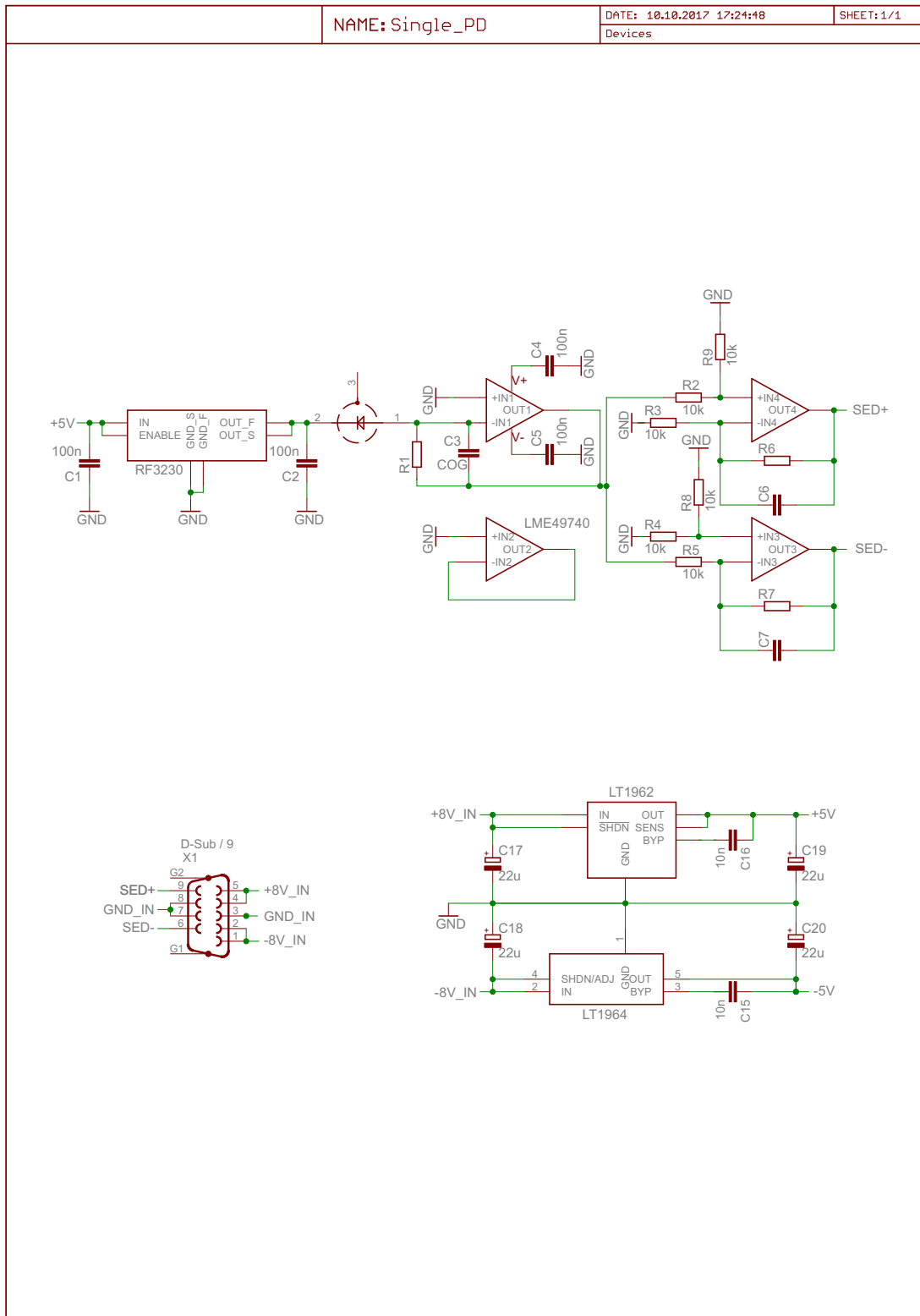


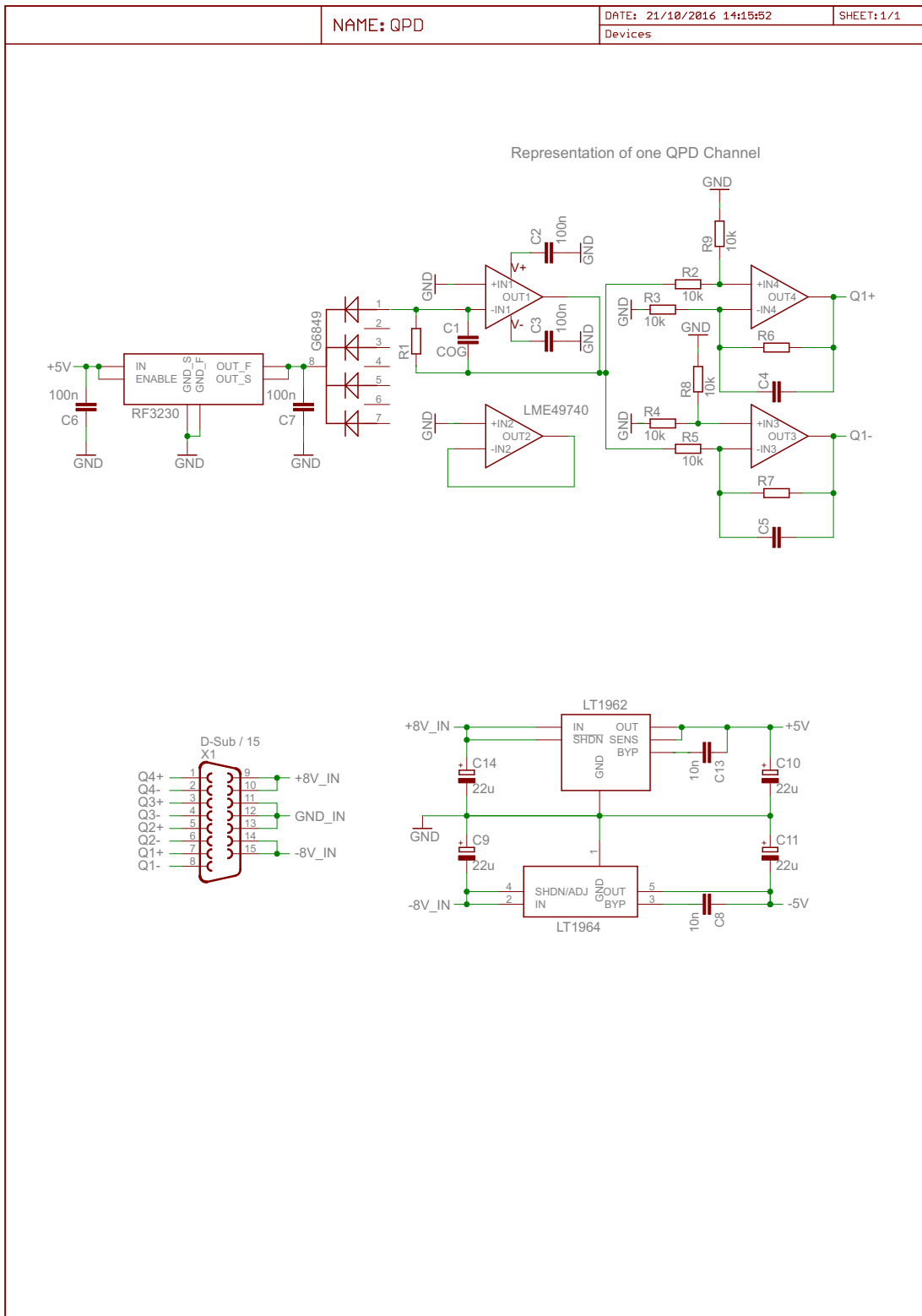
Figure A.1: Parameters for calculating the kinematic trace of the test mirror centre c_{TM} .

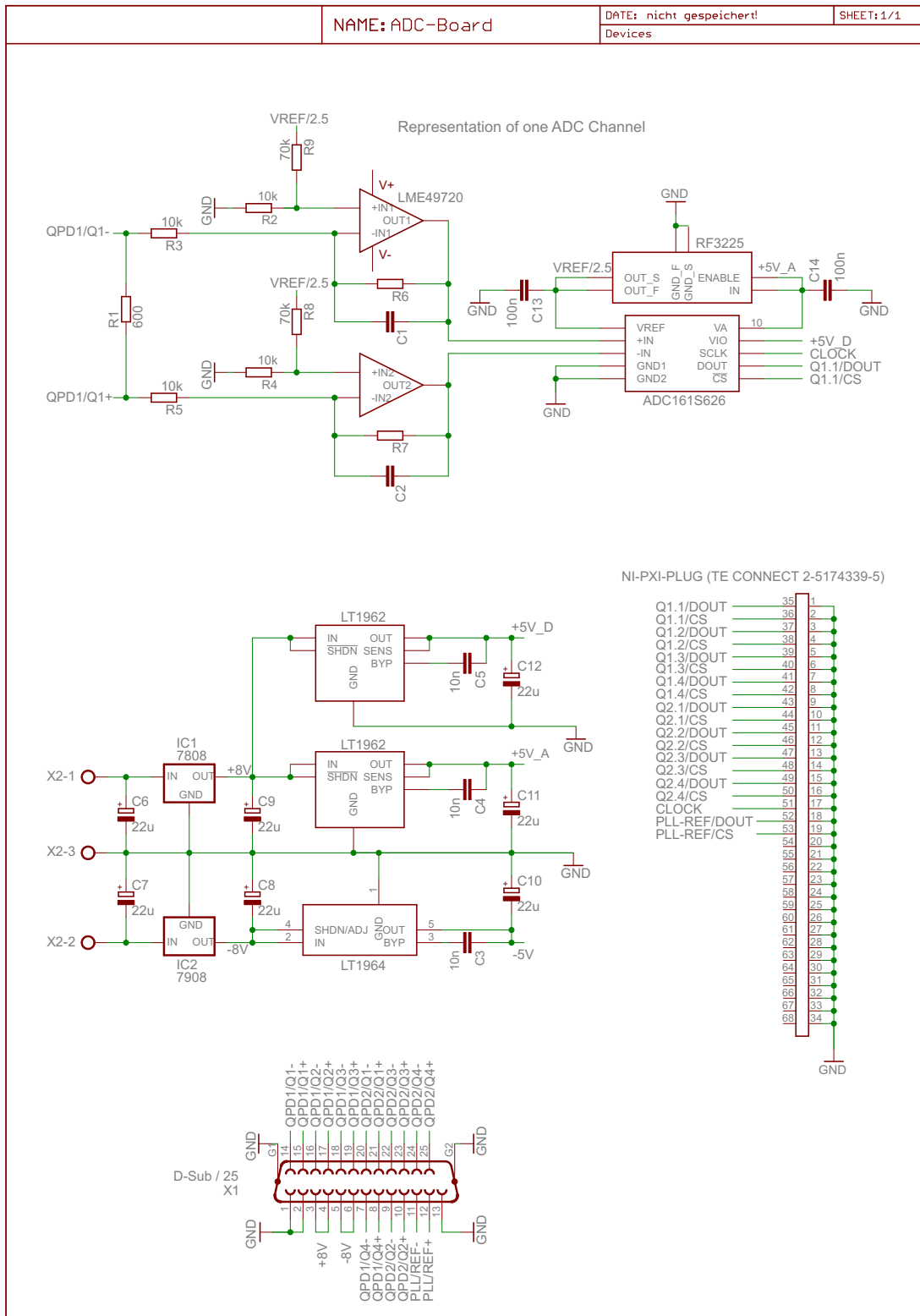
A.2 Circuit Diagrams of the Interferometer Electronics

This appendix contains the circuit diagrams of the single element (PD) and quadrant photo detectors (QPD), as well as the analog digital converters (ADC), as utilised in the heterodyne interferometers for the topography measurements of a SPM dummy (presented in Chapter 3). The resistors and capacitors, which influence the amplification and low-pass filtering of the processed signals (usually located in the feedback lines of specific operational amplifiers) are not defined in these diagrams, since they are supposed to be adapted to the chosen application. In order to keep this flexibility they are also not equipped on the original circuit boards.



A.2 Circuit Diagrams of the Interferometer Electronics



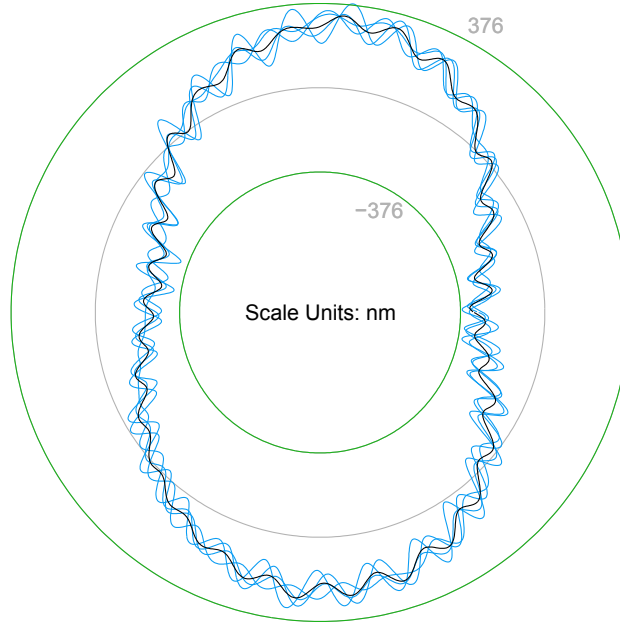


A.3 Error Movements of the ALAR 100-LP Rotation Stage

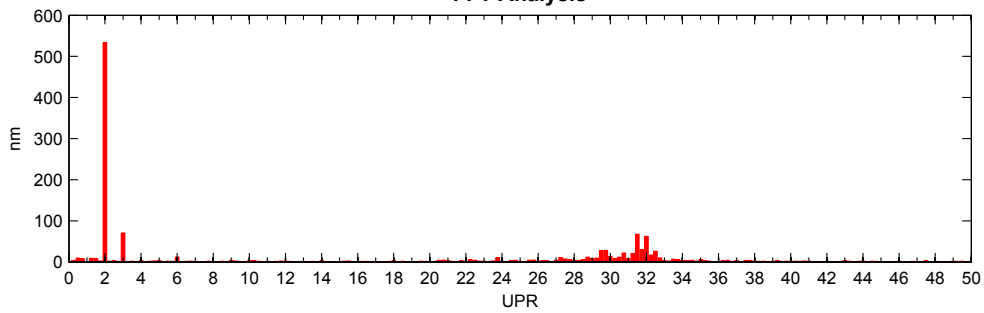
This appendix contains the data sheets of the error movements of the specific rotation stage ALAR 100-LP (by Aerotech), used in the setup for topography measurements of a SPM (presented in Chapter 3). The measurements were performed and provided by Aerotech.



Axial Error Motion



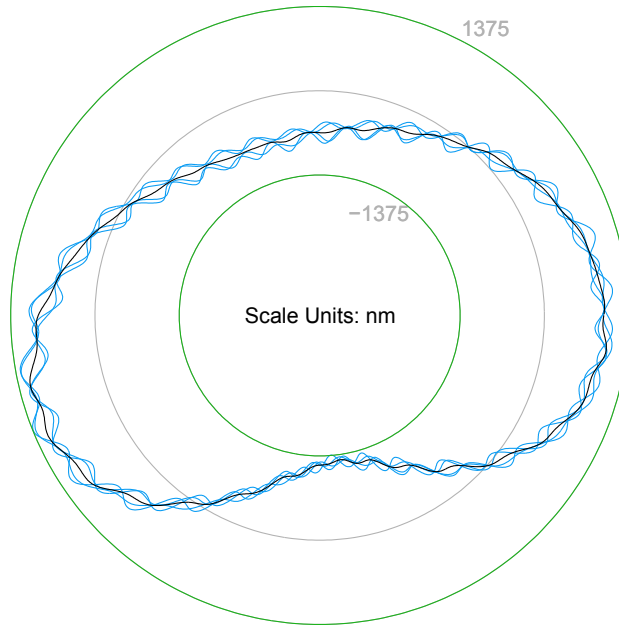
FFT Analysis



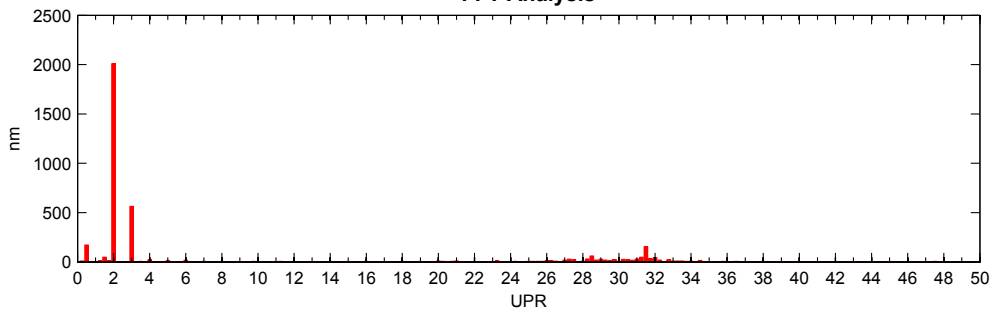
Results	Comments	Test Conditions
<p>Synch. – Residual = 658.09 nm Synch. – Total = 919.23 nm Asynch. = 166.71 nm Total = 1036.31 nm Fund. Mag. = 447.50 nm TIR = 1154.99 nm</p>	<p>Serial No.: 171357-A-1-1 Stage: ALAR100-LP Date: 03 Apr 2014 11:41:12 Operator: MT File Name: 171357-A-1-1.Ida</p>	<p>Test Speed: 60.0 RPM Data Points/Rev: 1440 Revolutions: 4 Target Artifact: 1" Dia. Test Ball Sensor: Lion Cap. Probe (2500 nm/V) Data Synch: Target Eccentricity Low Pass Filter: 50 UPR</p>



Fixed Sensitive Radial Error Motion



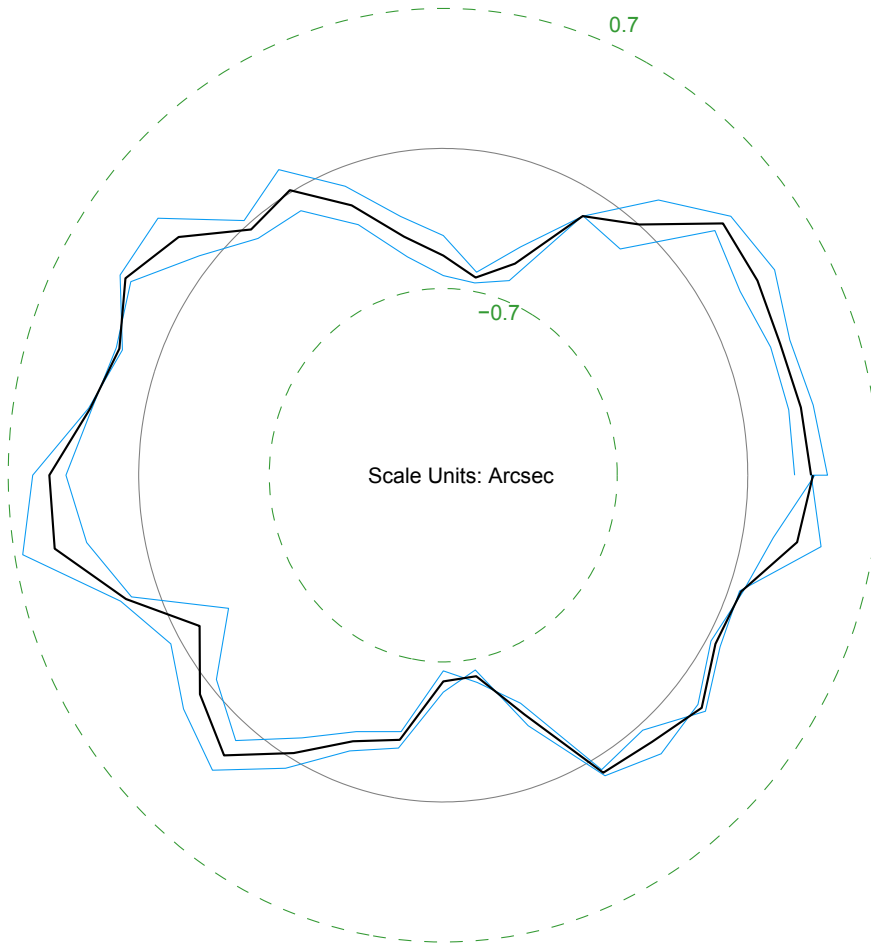
FFT Analysis



<p>Results</p> <p>Synch. = 2480.23 nm Asynch. = 453.34 nm Total = 2749.86 nm TIR = 14146.54 nm</p>	<p>Comments</p> <p>Serial No.: 171357-A-1-1 Stage: ALAR100-LP Date: 03 Apr 2014 11:34:22 Operator: MT File Name: 171357-A-1-1.lda</p>	<p>Test Conditions</p> <p>Test Speed: 60.0 RPM Data Points/Rev: 1440 Revolutions: 4 Target Artifact: 1" Dia. Test Ball Sensor: Lion Cap. Probe (2500 nm/V) Data Synch: Target Eccentricity Low Pass Filter: 50 UPR</p>
--	---	--



Tilt Error Motion



<p>Results</p> <p>Synch. = 1.11 Arcsec Asynch. = 0.36 Arcsec Total = 1.31 Arcsec</p>	<p>Comments</p> <p>Serial No.: 171357-A-1-1-A Stage Type: ALAR-100-LP Date Tested: April 2, 2014 08:31:20 Operator: M. Trozzi Equipment ID: HighAccuracy Amplifier: ML @ 10 Amps Controller: Ensemble 4.7.2.2 Optic Location: 60mm ABOVE TT Payload: 5KG</p>	<p>Test Conditions</p> <p>Air Temperature: 20.9 °C Test Length: 360.0 deg Step Size: 10.0 deg Number of Runs: 1, Bidirectional Test Instrument: Autocollimator Test Orientation: Horizontal Rotating Sensitive Test</p>
--	--	--

Bibliography

- [1] A. Einstein, "Die Feldgleichungen der Gravitation," (1915).
- [2] A. Einstein, "Naherungsweise Integration der Feldgleichungen der Gravitation," (1916).
- [3] A. Einstein, "Uber Gravitationswellen," (1918).
- [4] S. Hawking and W. Israel, eds., *General Relativity: An Einstein Centenary Survey* (Cambridge University Press, 1979).
- [5] J. Weber, "Detection and generation of gravitational waves," *Physical Review* **117** (1960).
- [6] A. Waard *et al.*, "MiniGRAIL, the first spherical detector," *Classical Quantum and Gravity* **20** (2003).
- [7] J. Taylor, L. Fowler, and P. McCulloch, "Measurements of general relativistic effects in the binary pulsar PSR 1913+16," *Nature* **277** (1979).
- [8] J. Taylor and J. Weisberg, "A new test of general relativity - gravitational radiation and the binary pulsar PSR 1913+16," *Astrophysical Journal* **253** (1982).
- [9] M. Gertsenshtein and V. Pustovoit, "On the detection of low-frequency gravitational waves," *Soviet Physics JETP* **16** (1962).
- [10] S. Rowan and J. Hough, "Gravitational wave detection by interferometry," *Living Reviews in Relativity* (2000).
- [11] E. Fitzsimons, "Techniques for precision interferometry in space," Ph.D. thesis, University of Glasgow (2010).
- [12] B. P. Abbott *et al.*, "Observation of gravitational waves from a binary black hole merger," *Physical Review Letters* **116** (2016).
- [13] ESA, "LISA, unveiling a hidden universe," Assessment study report, European Space Agency (2011).
- [14] ESA, "NGO, revealing a hidden universe: Opening a new chapter of discovery," Assessment study report, European Space Agency (2011).
- [15] Astrium, "LISA measurement performance," Tech. rep., Astrium GmbH (2007).
- [16] P. McNamara, S. Vitale, and K. Danzmann, "LISA Pathfinder," *Classical and Quantum Gravity* **25** (2008).
- [17] M. Armano *et al.*, "LISA Pathfinder: The experiment and the route to LISA," *Classical and Quantum Gravity* **26** (2009).

- [18] R. Gerndt *et al.*, "LTP - LISA Technology Package: Development challenges of a space-born fundamental physics experiment," *Journal of Physics: Conference Series* **154** (2009).
- [19] D. Bortoluzzi *et al.*, "Testing LISA drag-free control with the LISA technology package flight experiment," *Classical and Quantum Gravity* **20** (2003).
- [20] M. Armano *et al.*, "Sub-femto-*g* free fall for space-based gravitational wave observatories: LISA Pathfinder results," *Physical Review Letters* **116** (2016).
- [21] D. Weise *et al.*, "Alternative opto-mechanical architectures for the LISA instrument," *Journal of Physics: Conference Series* **154** (2009).
- [22] D. Weise *et al.*, "Opto-mechanical architecture of the LISA instrument," *Proceedings of the 7th ICSO* (2008).
- [23] B. Lange, "The drag-free satellite," *AIAA Journal* **2** (1964).
- [24] D. B. DeBra, "Disturbance compensation system design," *APL Technical Digest* **12** (1973).
- [25] Staff of the Space Department (The Johns Hopkins University) and Staff of the Guidance and Control Laboratory (Stanford University), "A satellite freed of all but gravitational forces: TRIAD I," *Journal of Spacecraft and Rockets* **11** (1974).
- [26] C. W. F. Everitt *et al.*, "The Gravity Probe B test of general relativity," *Classical and Quantum Gravity* **32** (2015).
- [27] Astrium, "LISA feasibility study," *Tech. rep.*, Astrium GmbH (2000).
- [28] B. Lange, "Managing spherical proof masses in drag-free satellites with application to the LISA experiment," *Classical and Quantum Gravity* **18** (2001).
- [29] B. Lange, "Preliminary studies of spherical proof masses in LISA drag-free satellites," *SPIE Proceedings* **4856** (2002).
- [30] U. Johann *et al.*, "Novel payload architectures for LISA," *AIP Conference Proceedings* **873** (2006).
- [31] K.-X. Sun *et al.*, "LISA gravitational reference sensors," *Journal of Physics: Conference Series* **60** (2007).
- [32] K.-X. Sun *et al.*, "Advanced gravitational reference sensor for high precision space interferometry," *Classical and Quantum Gravity* **22** (2005).
- [33] J. W. Conklin *et al.*, "Determination of spherical test mass kinematic with a modular gravitational reference sensor," *Journal of Guidance, Control and Dynamics* **31** (2008).
- [34] K.-X. Sun *et al.*, "Modular gravitational reference sensor development," *Journal of Physics: Conference Series* **154** (2009).
- [35] F. Marcelja *et al.*, "Precision spheres for the Gravity Probe B experiment," *Classical and Quantum Gravity* **32** (2015).

- [36] G. Bartl *et al.*, "Volume determination of the Avogadro spheres of high enriched ^{28}Si with a spherical Fizeau interferometer," *Metrologia* **48** (2011).
- [37] D. Gerardi *et al.*, "Advanced drag-free concepts for future space-based interferometers: Acceleration noise performance," *Review of Scientific Instruments* **85** (2014).
- [38] J. Crowder and N. J. Cornish, "Beyond LISA: Exploring future gravitational wave missions," *Physical Review D* **72** (2005).
- [39] H. Kögel *et al.*, "Interferometric characterization and modeling of pathlength errors resulting from beamwalk across mirror surfaces in LISA," *Applied Optics* **52** (2013).
- [40] G. E. Sommaergren, "Optical heterodyne profilometry," *Applied Optics* **20** (1986).
- [41] D. Pantzer, J. Politch, and L. Ek, "Heterodyne profiling instrument for the Angstrom region," *Applied Optics* **25** (1986).
- [42] C. M. Wu, S. T. Lin, and J. Fu, "Heterodyne interferometer with two spatial-separated polarization beams for nanometrology," *Optical and Quantum Electronics* **34** (2002).
- [43] T. Schuldt *et al.*, "Picometer and nanoradian optical heterodyne interferometry for translation and tilt metrology of the LISA GRS," *Classical and Quantum Gravity* **26** (2009).
- [44] T. Schuldt, "An optical readout for the LISA gravitational reference sensor," Ph.D. thesis, Humboldt Universität zu Berlin (2010).
- [45] E. Morrison *et al.*, "Automatic alignment of optical interferometers," *Applied Optics* **33** (1994).
- [46] E. Morrison *et al.*, "Experimental demonstration of an automatic alignment system for optical interferometers," *Applied Optics* **33** (1994).
- [47] R. Spero, "Optical path error from beamwalk across irregular mirror surfaces," Draft (1998).
- [48] Astrium, "Telescope design for IFP," Technical note, Astrium GmbH (2007).
- [49] Astrium, "System parameters and error budgets for IFP/Single GRS," Budget report, Astrium GmbH (2007).
- [50] H. Kögel *et al.*, "Interferometric surface mapping of a spherical proof mass for ultra precise inertial reference sensors," *Applied Optics* **55** (2016).
- [51] C. Brugger *et al.*, "An experiment to test In-Field Pointing for LISA," Proceedings of the 10th ICSO (2014).
- [52] E. J. Elliffe *et al.*, "Hydroxide-catalysis bonding for stable optical systems for space," *Classical and Quantum Gravity* **22** (2005).
- [53] D. Gerardi, "Advanced drag-free concepts for future space based interferometers," Ph.D. thesis, University of Stuttgart (2016).
- [54] S. Buchman *et al.*, "Charge measurement and control for the Gravity Probe B gyroscopes," *Review of Scientific Instruments* **66** (1995).

- [55] T. Sumner *et al.*, "Description of charging/discharging processes of the LISA sensors," *Classical and Quantum Gravity* **21** (2004).
- [56] T. Ziegler *et al.*, "Modeling and performance of contact-free discharge systems for space inertial sensors," *IEEE Transactions on Aerospace and Electronic Systems* **50** (2012).

Acknowledgements

At this point, I want to thank all the people who supported me during this doctorate. Their help and advice were a crucial contribution for carrying out this ambitious task.

First of all I want to express my very great appreciation towards my supervisor on the part of the University of Bremen Prof. Dr. Claus Braxmaier, as well as the head of the department Future Programs & Missions at Airbus DS Dr. Ulrich Johann, who gave me the special opportunity to work on such an interesting project. More than that, with their distinguished skills in physics and space engineering they were the initiators of several key aspects of the alternative LISA payload architecture presented in this thesis, hence establishing this doctorate. It was a pleasure learning from their wealth of expertise and foremost a key contribution for its success.

I would also like to offer my special thanks to the supervisors on the part of Airbus DS Dr. Dennis Weise, Dr. Ewan Fitzsimons and Dr. Alexander Sell. With their substantial knowledge in physics and mechanical engineering, each one of them provided invaluable support and thereby contributed crucially to this doctorate. In this respect, I am also very grateful for the considerable amount of time and effort they invested for answering questions and teachings - I am still impressed how you managed that along with your daily work.

My special thanks are extended to my colleagues from the LET and SET laboratories, Martin Gohlke, Dr. Thilo Schuldt, Dr. Andreas Keller, Dr. Ruven Spannagel, Dr. Franz-Georg Hey and Oliver Mandel. They always had an open ear and invested the time to discuss technical and mathematical problems, which rose during the experimental work in the laboratory. Most of the times, these discussions led to helpful inputs and suggestions, which helped solving them. Together, they created a pleasant and sometimes also humorous working atmosphere in the laboratory, which was more than once welcome to keep one's mind.

I also want to thank Prof. Dr. Gerhard Heinzl from the University of Hannover, who has kindly offered to be the external examiner of this doctorate.

Looking back, my time as a PhD student was very interesting and informative. I am deeply grateful for giving me this special opportunity. It was a pleasure to work in such a friendly and supportive environment with so many cooperative, encouraging and highly skilled colleagues. The knowledge and skills they taught me during this period will be - I am sure about that - very useful for my future.

Studentische Arbeiten

In der vorliegenden Arbeit sind Ergebnisse enthalten, die im Rahmen der Betreuung folgender studentischer Arbeiten entstanden sind:

- [1] Clemens Birkenmaier, "Dimensioning, setup and test of a heterodyne frequency generation for high precision laser interferometry", Student Project, University of Applied Sciences Konstanz (2013).
- [2] Clemens Birkenmaier, "Development and validation of an electro magnetic levitation system for a spherical inertial reference sensor with optical readout", Bachelor Thesis, University of Applied Sciences Konstanz (2013).
- [3] Dominik Möhrle, "Development and testing of quadrant photo diodes for heterodyne interferometry", Master Thesis, University of Applied Sciences Konstanz (2014).
- [4] Cessica Cenni, "Development of FPGA-based controllers for a laboratory model of a spherical inertial reference sensor with optical readout", Master Thesis, University of Pisa (2015).
- [5] Stefan Rasch, "Modelling and validation of a control system for a magnetic levitation system", Master Thesis, University of Bremen (2015).
- [6] Francesco Mostallino, "Design of a rotation mechanism for interferometric surface topography of a sphere", Master Thesis, University of Pisa (2017).

Student Theses & Projects

This thesis contains results, which were generated in the course of the supervision of the following student theses and projects:

- [1] Clemens Birkenmaier, "Dimensioning, setup and test of a heterodyne frequency generation for high precision laser interferometry", Student Project, University of Applied Sciences Konstanz (2013).
- [2] Clemens Birkenmaier, "Development and validation of an electro magnetic levitation system for a spherical inertial reference sensor with optical readout", Bachelor Thesis, University of Applied Sciences Konstanz (2013).
- [3] Dominik Möhrle, "Development and testing of quadrant photo diodes for heterodyne interferometry", Master Thesis, University of Applied Sciences Konstanz (2014).
- [4] Cessica Cenni, "Development of FPGA-based controllers for a laboratory model of a spherical inertial reference sensor with optical readout", Master Thesis, University of Pisa (2015).
- [5] Stefan Rasch, "Modelling and validation of a control system for a magnetic levitation system", Master Thesis, University of Bremen (2015).
- [6] Francesco Mostallino, "Design of a rotation mechanism for interferometric surface topography of a sphere", Master Thesis, University of Pisa (2017).